

論文 / 著書情報  
Article / Book Information

題目(和文)	電磁駆動衝撃波における緩和領域の研究
Title(English)	A study on relaxation layer of electro-magnetically driven strong shock waves
著者(和文)	近藤康太郎
Author(English)	Kotaro Kondo
出典(和文)	学位:博士(理学), 学位授与機関:東京工業大学, 報告番号:甲第7524号, 授与年月日:2009年3月26日, 学位の種別:課程博士, 審査員:堀岡 一彦,河村 徹
Citation(English)	Degree:Doctor (Science), Conferring organization: Tokyo Institute of Technology, Report number:甲第7524号, Conferred date:2009/3/26, Degree Type:Course doctor, Examiner:.
学位種別(和文)	博士論文
Type(English)	Doctoral Thesis

# A Study on Relaxation Layer of Electro-magnetically Driven Strong Shock Waves

A thesis presented  
by

KONDO Kotaro

*Fourth Edition*

Department of Energy Sciences  
Interdisciplinary Graduate School of Science and Engineering  
March 2009



TOKYO INSTITUTE OF TECHNOLOGY

# Contents

Title Page . . . . .	i
Table of Contents . . . . .	iii
List of Figures . . . . .	vii
List of Tables . . . . .	x
Acknowledgments . . . . .	xi
<b>1 Introduction</b>	<b>1</b>
1.1 Background and Motivation . . . . .	2
1.2 Similarity and Scaling of Laboratory Plasma to Astrophysical Phenomena . . . . .	6
1.3 Scope and Outline of Thesis . . . . .	7
<b>2 Formation of Electro-magnetically Driven Strong Shock Waves</b>	<b>9</b>
2.1 A Short Review of Strong Shock Wave Physics . . . . .	9
2.1.1 Shock Wave and Rankine-Hugoniot Relations . . . . .	9
2.1.2 Plasma Shock Waves and Relaxation Times of Coulomb Interaction . . . . .	13
2.1.3 Radiative Shock Waves and Characteristic Time for Radiation Flux . . . . .	16
2.1.4 Initial Ionization in Strong Shock Waves . . . . .	18
2.1.5 Structure of Strong Shock Waves . . . . .	19
2.2 Methods of Generating Strong Shock Waves . . . . .	20
2.2.1 Magnetic Pressure . . . . .	20
2.2.2 Plasma Focus . . . . .	22
2.2.3 Electro-magnetically Driven Method . . . . .	23
2.3 Experimental Setup . . . . .	24
2.3.1 Electro-magnetic Device . . . . .	24
2.3.2 Tapered Electrodes and Guiding Tube . . . . .	26
2.4 Measuring instruments . . . . .	27
2.4.1 Current Probe and Discharge Current . . . . .	28
2.4.2 Fast Framing and Streak Image Camera . . . . .	30
2.5 Steady and One-dimensional Shock Waves and Self-emission Profiles . . . . .	31

2.5.1	Formation of Steady and One-dimensional Shock Waves . . . .	31
2.5.2	Self-emission Profiles of Steady and One-dimensional Shock Waves	32
2.6	Concluding Remarks . . . . .	35
<b>3</b>	<b>Calculation of Strong Shock Wave Structure Based on Steady and One-dimensional Condition</b>	<b>37</b>
3.1	Atomic Processes . . . . .	37
3.1.1	Collisional Ionization . . . . .	39
3.1.2	Three Body Recombination . . . . .	40
3.1.3	Radiative Recombination . . . . .	41
3.1.4	Photoionization . . . . .	42
3.1.5	Electron Collisional Excitation and Deexcitation . . . . .	43
3.1.6	Radiative Decay . . . . .	45
3.1.7	Atom-atom Collisional Ionization . . . . .	46
3.1.8	Charge Transfer Collision . . . . .	46
3.2	Rate Equation . . . . .	47
3.3	Steady and 1-D hydrodynamic Conservation Laws and Ion-electron Relaxation Equation . . . . .	48
3.4	Calculation Results . . . . .	50
3.4.1	Calculation Flow and Calculation Region in Shock Waves . . .	50
3.4.2	Two Initial Free Parameters . . . . .	52
3.4.3	Initial Gas Pressure and Relaxation Structure . . . . .	53
3.4.4	Initial Electron Temperature and Relaxation Length . . . . .	56
3.4.5	Effects of Charge Transfer and Electron-neutral Collision . . .	59
3.4.6	Radiation Effect on Shock Wave Structure with Relaxation Layer	62
3.5	Concluding Remarks . . . . .	64
<b>4</b>	<b>Measurement of Electron Temperature in Shock-heated Region by Spectroscopic Method</b>	<b>65</b>
4.1	Fundamental Principle of the Measurement . . . . .	65
4.1.1	Line Emission from Optically Thin Medium . . . . .	65
4.1.2	Emission from Optically Thick Medium . . . . .	66
4.2	Selections of Wavelength . . . . .	67
4.3	Setup for Electron Temperature Measurement . . . . .	68
4.3.1	Delay Pulse Setup and Streak Image Camera . . . . .	68
4.3.2	Spectroscope and Characteristics . . . . .	70
4.4	Electron Temperature Distribution . . . . .	71
4.4.1	Electron Temperature Distribution for Case of $p_1 = 0.12$ Torr	72
4.4.2	Electron Temperature Distribution for Case of $p_1 = 0.75$ Torr	75
4.5	Concluding Remarks . . . . .	79

---

<b>5</b>	<b>Estimation of Electro-magnetically Driven Strong Shock Waves with Relaxation Layer</b>	<b>81</b>
5.1	Emission from Shocked Region . . . . .	81
5.2	Initial Ionization by Atom-atom Collisional Ionization in Shock Structure . . . . .	85
5.3	Radiative Cooling in Shock Waves . . . . .	87
5.4	Relation between Electro-magnetically Driven Strong Shock Waves to Radiative SNRs . . . . .	91
5.5	Concluding Remarks . . . . .	93
<b>6</b>	<b>Conclusions</b>	<b>95</b>
<b>A</b>	<b>Rogowski Coil and Calibration</b>	<b>99</b>
<b>B</b>	<b>Sweep and Delay Time of Streak Unit</b>	<b>103</b>
<b>C</b>	<b>Xe II Atomic Data</b>	<b>106</b>
	<b>Bibliography</b>	<b>108</b>

# List of Figures

1.1	The supernova remnant SNR 1987A. Credit: NASA, P. Challis, R. Kirshner (Harvard-Smithsonian Center for Astrophysics) and B. Sugerman (Space Telescope Science Institute) . . . . .	4
1.2	Shock parameters in Xe gas by different generating methods . . . . .	5
1.3	A similarity of identical hydrodynamical behavior between SN 1987A and our experiment based on Euler number [7] . . . . .	7
2.1	A steady shock at rest and that in moving frame with the front speed	11
2.2	An electron orbit by Coulomb interaction . . . . .	14
2.3	Temperature distributions of steady and planar shock wave . . . . .	21
2.4	A sketch of a plasma focus device . . . . .	23
2.5	A sketch of conventional electro-magnetic shock tube . . . . .	24
2.6	A sketch of the experimental setup . . . . .	25
2.7	Schematic of the tapered electrodes and the guiding tube . . . . .	27
2.8	Typical discharge current waveform . . . . .	29
2.9	The equivalent circuit and block diagram of the device . . . . .	29
2.10	Framing and streak images of electro-magnetically driven shock waves	32
2.11	Framing and streak images of electro-magnetically driven shock wave in the guiding tube . . . . .	33
2.12	Initial pressure vs shock Mach number and shock speed . . . . .	35
3.1	A sketch of atomic processes in plasma . . . . .	38
3.2	Schematic of Electron impact ionization process . . . . .	39
3.3	Schematic of three body recombination process . . . . .	41
3.4	Schematic of radiative recombination process . . . . .	42
3.5	Schematic of photoionization process . . . . .	42
3.6	Schematic of electron impact excitation process . . . . .	44
3.7	Schematic of electron impact deexcitation process . . . . .	45
3.8	Schematic of radiative decay process . . . . .	45
3.9	Flowchart for numerical simulation of shock heated relaxation layer .	51
3.10	Temperature distribution sketch, initial condition and calculation region	52

3.11	Relaxation layer of shock heated Xe for $T_e^0 = 2.5$ eV at $p_1 = 0.12$ Torr	54
3.12	Relaxation layer of shock heated Xe for $T_e^0 = 2.5$ eV at $p_1 = 0.75$ Torr	55
3.13	Relaxation layer of shock heated Xe for $T_e^0 = 2.5$ eV at $p_1 = 3.0$ Torr	55
3.14	Relaxation layer of shock heated Xe for $T_e^0 = 2.2$ eV at $p_1 = 0.12$ Torr	57
3.15	Relaxation layer of shock heated Xe for $T_e^0 = 2.8$ eV at $p_1 = 0.12$ Torr	57
3.16	Relaxation layer of shock heated Xe for $T_e^0 = 2.2$ eV at $p_1 = 0.75$ Torr	58
3.17	Relaxation layer of shock heated Xe for $T_e^0 = 2.8$ eV at $p_1 = 0.75$ Torr	58
3.18	Relaxation layer of shock heated Xe for $T_e^0 = 2.2$ eV at $p_1 = 3.0$ Torr	59
3.19	Relaxation layer of shock heated Xe for $T_e^0 = 2.8$ eV at $p_1 = 3.0$ Torr	60
3.20	Schematic of radiation cooling effects on ion and electron temperature distributions . . . . .	63
4.1	Relations between the intensity ratio and electron temperature . . . . .	68
4.2	Top view of the experimental setup with basic diagnostics . . . . .	69
4.3	Focused image of the scattered light by LD Green Laser . . . . .	71
4.4	Streak spectral image of 433 nm for $p_1 = 0.12$ Torr . . . . .	73
4.5	Streak spectral image of 484 nm for $p_1 = 0.12$ Torr . . . . .	73
4.6	Streak spectral image of 529 nm for $p_1 = 0.12$ Torr . . . . .	74
4.7	Electron temperature distribution for $p_1 = 0.12$ Torr . . . . .	76
4.8	Streak spectral image of 433 nm for $p_1 = 0.75$ Torr . . . . .	76
4.9	Streak spectral image of 484 nm for $p_1 = 0.75$ Torr . . . . .	77
4.10	Streak spectral image of 529 nm for $p_1 = 0.75$ Torr . . . . .	78
4.11	Electron temperature distribution for $p_1 = 0.75$ Torr . . . . .	78
5.1	Streak profiles of $\lambda = 434$ nm for different observation points in case of $p_1 = 0.12$ Torr . . . . .	83
5.2	Streak profiles of $\lambda = 434$ nm for different observation points in case of $p_1 = 0.75$ Torr . . . . .	84
5.3	Framing image of shock wave through the guiding tube in case of $p_1 = 0.12$ Torr . . . . .	85
5.4	Framing image of shock wave through the guiding tube in case of $p_1 = 0.75$ Torr . . . . .	86
5.5	Relaxation layer of shock heated Xe for $T_e^0 = 3.5$ eV at $p_1 = 0.12$ Torr	88
5.6	Ion and electron temperature distributions with radiative flux factor $\beta$	90
5.7	Relaxation layer of shock heated Xe with radiative flux ( $\beta = 4.9$ ) for $T_e^0 = 3.5$ eV at $p_1 = 0.12$ Torr . . . . .	91
5.8	Relation between temperature and density for radiative effect and optical depth on the spatial scales $h = 10^{16}$ cm of young SNRs [7] . . . . .	92
6.1	Various shock waves and their dominant dissipative processes . . . . .	97
A.1	A sketch of Rogowski Coil . . . . .	100
A.2	Equivalent circuit of Rogowski coil . . . . .	100

---

A.3	Discharge current for calibration . . . . .	101
B.1	Setup for runtime measurement of LED . . . . .	104
B.2	Setup for calibrating of streak unit . . . . .	104
B.3	Timing chart for the calibration . . . . .	105

# List of Tables

3.1	Empirical formulae of collisional ionization rate coefficients . . . . .	40
3.2	Shock parameters estimated from experimental results and Rankine-Hugoniot Relations . . . . .	53
3.3	Plasma parameters for the estimation of charge-transfer collision . . .	60
4.1	Xe II data of three lines: 433, 484, and 529 nm . . . . .	67
4.2	Evaluated sweep time and delay time of streak mode . . . . .	70
C.1	Xe II atomic data . . . . .	106

# Acknowledgments

This thesis has been supported tremendously from numerous people. I would like to express my deepest gratitude to many people.

First, I would like to acknowledge my supervisor Professor Kazuhiko Horioka at Tokyo Institute of Technology. He, who is a big-hearted person, has encouraged me since I was undergraduate student. The thesis could never be written without his continuous help, accurate advice and useful comment.

My special thanks are for Assistant Professor Mitsuo Nakajima at Tokyo Institute of Technology. He taught me how significant profound thoughts is through physics, economics, biology and more general problems. His impressive abilities have been respected all the way in my life.

I am very grateful to Associate Professor Tohru Kawamura, who is my sub-research adviser, at Tokyo Institute of Technology. He is a great atomic physicist, and a “food entertainer” of our group. I can never forget pleasant memories eating ramen and okonomiyaki.

Thanks to Dr. Makoto Shiho at Institute for Applied Optics for his kind support. He showed me that “stick to the basics” is important for research.

My special thanks to Professor Hiroyuki Yamasaki and Professor Yoshihiro Okuno, and Associate Professor Hiroshi Akatsuka at Tokyo Institute of Technology for their kind reviews of the thesis.

I would like to express my sincere appreciation to Dr. Mark Sherlock at Rutherford Appleton Laboratory and Dr. Simon Bland at Imperial College London. They welcomed me to their laboratories. The discussions were greatly useful for my research.

Dr. Igor Kaganovich at Princeton Plasma Physics Laboratory made beneficial comments in International conferences. The conference banquet of HIF 2008 is great memory for me.

Mr. Guenther Leopold Winkler at International Atomic Energy Agency was an excellent supervisor during my internship in IAEA. The time spent in Vienna with him and the colleagues was brilliant. Vienna is my second hometown.

I had the pleasure of meeting Professor Masaki Saito at Tokyo Institute of Technology. He gave me a grand chance to intern in IAEA.

Mr. Suguru Nishinomiya, Mr. Akito Nagata, and Mr. Yusuke Sakai are good compeers in Tokyo Institute of Technology. I shared joys and sorrows with them during my doctoral course. They supported me to write this thesis.

Special thanks are due to Horioka, Shiho, and Kawamura laboratory members (Dr. Majid Masnavi, Mr. Takashi Saito, Mr. Noriyuki Hikida, Mr. Yutaka Aoyama, Mr. Yuji Otsuka, Mr. Sota Kinoshita, Mr. Kazuki Takahashi, Mr. Yuuki Uchida, Mr. Kazumasa Takahashi, Mr. Masakazu Tomii, Mr. Daisuke Nunotani, Mr. Takeshi Hosoi, as the present members, Dr. Nobuhiro Sakamoto, Dr. Jun Hasegawa, Dr. Takashi Kikuchi, Dr. Naoki Tajima, Mr. Tomoyuki Aizawa, Mr. Takashi Mizoguchi, Mr. Chihiro Iida, Ms. Miho Io, Mr. Yuji Kiriya, Dr. Toru Sasaki, Mr. Naoki Kobayashi, Mr. Hiroyuki Nagata, Mr. Masayoshi Watanabe, Mr. Atsushi Kikuchi, Mr. Takahiro Ikeda, Mr. Takato Ishii, Mr. Kensaku Takahashi, Mr. Yuuri Yano, Mr. Wataru Sekine, Mr. Naohiro Okoshi, Mr. Masashi Kobayashi, Mr. Takeshi Terada, Mr. Michiyoshi Yuyama, as the graduates), and many colleagues (Dr. Taku Inaniwa, Mr. Kengo Akiu, Mr. Kunihiko Tomiyasu, Mr. Hiroaki Taniguchi, Mr. Kaoru Hashimoto, Mr. Keita Kitade, Mr. Mitsuo Okamoto, Dr. Ken Katagiri), could help my campus life to be fruitful.

In addition, I gratefully acknowledge financial support by Japan Student Services Organization, the 21st Century Center Of Excellence (COE) Program at Tokyo Institute of Technology “Innovative Nuclear Energy Systems for Sustainable Development of the World (COE-INES)” by the Japanese Ministry of Education, Culture, Sports, Science and Technology, and the Japan Society for the Promotion of Science.

Last in this list but first in my heart, I would like to thank my best friends and my family. Without them, this work would never have come into existence.

Yokohama, Japan

March 2009

*KONDO Kotaro*

# Chapter 1

## Introduction

*“That all started with the Big Bang.”*

According to the Big Bang model [1,2], the universe expanded from an extremely dense and hot state and is continuously evolving. A few minutes into the expansion, when the temperature was  $\sim 10^9$  K and the density was about that of our atmosphere, neutrons combined with protons to form the universe’s deuterium and helium nuclei in a process called “Big Bang nucleosynthesis” [3]. Most protons remained uncombined as hydrogen nuclei. As the universe cooled, the invariant mass energy density of matter came to gravitationally dominate that of the photon radiation. After about 380,000 years from the Big Bang, the electrons and nuclei are considered to be combined into atoms: hence, the radiation decoupled from the matter and continued the expansion with space. This relic radiation is known as the cosmic microwave background radiation [4], whose temperature is estimated to be less than 3 K, whereas radiation temperatures of brilliant stars are several thousand K. Thus, our universe is dynamically evolving in an extreme non-equilibrium state and our world is in an intermediate stage of the continuously relaxing universe.

As similar to the Big Bang universe, scale-down astrophysical phenomena in it are also in non-equilibrium. Supernova explosion which provides opportunities for the birth and death of a star, and extreme-high velocity phenomena such as accretion flows into black holes [5] have given physical interests to human-beings. Study of these

phenomena contributes not only to comprehension of origin of the universe but also to developments of nuclear fusion power generation, short-wavelength light source and their derivative technologies. However, since the phenomena are in extremely high temperature, density and pressure condition, so far, the numerical calculations and observations of incident events in space have been the only methods of understanding the astrophysical phenomena.

On the other hand, the recent progress of pulse power and high intensity laser technologies have realized density conditions as high as several hundred times of a solid density. As above, these tools enable us to simulate the astrophysical phenomena in laboratory [6–8]. The simulation experiments have supplied a new measure of astrophysics to the computational and the observational astronomy, and the incorporated three approaches are expected to make a breakthrough for understanding of the astrophysical phenomena.

## 1.1 Background and Motivation

One of remarked phenomena accompanied by high energy density physics is strong shock wave. A conventional hydrodynamical shock wave [9] forms a step-like structure by energy and momentum transport, which are dominated by the collisions of fluid particles and the dissipation. When a shock velocity becomes higher, the fluid elements behind shock are dissociated, excited and ionized, and become a plasma. Once a plasma is formed, the plasma in the shock structure tends to have two, ion and electron, temperatures due to the mass difference between two particles [10]. Since there is a substantial difference between the ion and electron temperatures just behind shock front, the shock structure has ion-electron energy relaxation and ionization relaxation layers. Moreover, when the density is high and shock wave is too strong to neglect radiation effect, a zone dominated by radiative cooling appears behind the shock. Also a preheat structure is formed proceeding the shock front by radiation transport and electron heat conductivity. Then, the strong shock wave has a characteristic structure not only behind but also in the front of the shock: “precursor” region. As just described, we focus on a shock structure formed accompanied by

collisions of plasma fluid particles, heat conduction, ion-electron energy relaxation, ionization, radiation transport and interplay among them.

With different physical parameters, dominant physical processes in shock and the structure are quite different. Since astrophysical phenomena extend over an extremely wide range of parameters, each process in the structure is completely different. Here, we review simply two causes, radiation transport and ionization relaxation, of non-equilibrium shock structure and consider their relation to the astrophysical phenomena.

First we discuss the radiation effect. Assuming that plasma is optically thick, radiation energy flux  $W_{\text{rad}}$  is proportional to  $T_r^4$  according to the Stefan-Boltzmann law [11]. Here,  $T_r$  is radiation temperature. As radiation energy flux exponentially increases with a function of temperature, we can not ignore the contribution of radiation on shock structure at high  $T_r$ . One of remarkable phenomena, in which radiation effects play a significant role, is Supernova Remnant (SNR). The evolution of SNRs can be classified into four distinct phases [12, 13]: free expansion phase, adiabatic phase, radiative phase, and disappearance phase. In the radiative phase, radiation energy loss is significant compared to an initial explosion energy.

A photograph of the supernova remnant developing from SN 1987A is shown in Fig. 1.1. The bright spots in Fig. 1.1 are considered to be produced by the collision between the ejecta from the star and medium at the edges of the inner ring that encircled the star [14]. Analysis of spectra has shown that the shock wave driven into the ring are radiative, at least in the places. Thus, radiation process takes an important role for dynamics of SNRs [15–19]. Accretion flow where material falls into a compact object also forms a strong shock wave with significant radiation effects [20].

Second, ionization relaxation process in shock wave is addressed briefly. SNRs are characterized by their high electron temperature ( $\sim 10^7$  K) and low density ( $\leq 1 \text{ cm}^{-3}$ ). The duration, in which ionization process plays an important role, occupies a significant fraction of the life of a SNR ( $10^4 - 10^5$  year). In the ionization region, ions in the optically thin plasma relax to a collisional ionization equilibrium with electron heated by ion-electron momentum transfers. The underionized state is referred to as nonequilibrium ionization and has been observed in many SNRs. And

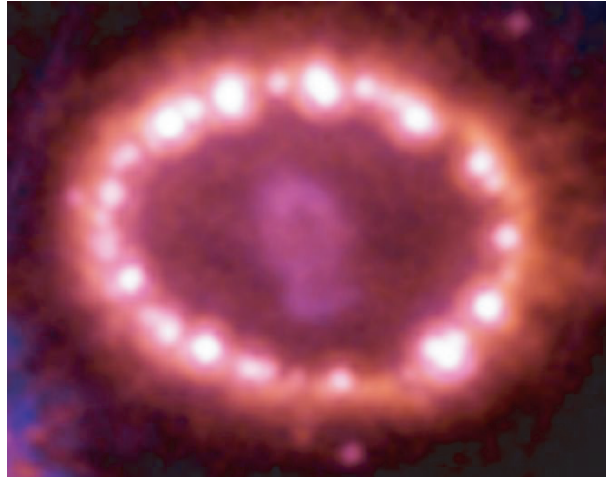


Figure 1.1: The supernova remnant SNR 1987A. Credit: NASA, P. Challis, R. Kirshner (Harvard-Smithsonian Center for Astrophysics) and B. Sugerman (Space Telescope Science Institute)

then, some SNRs are discovered to be “overionized” states [21]. Thermal conduction can cause the hot interior plasma to become overionized by reducing the temperature and density gradients, leading to an interior density increase and temperature decrease. Ionization relaxation and thermal conductivity also perform essential roles for SNRs dynamics.

As just described, the strong shock wave with relaxation layer is affected by many processes and is also strongly related to many astrophysical phenomena. It is ubiquitous in the universe and their estimation is important for exploration of these phenomena. Some theoretical approaches [10, 14, 22–24] are made based on a limited situation. However, the shock wave with relaxation layer matched to these theoretical models has not yet been generated experimentally and quantitative estimation of the strong shock wave with ionization relaxation, ion-electron energy relaxation, radiation effect and their interactions has never been established.

Strong shock wave has been investigated experimentally for several decades [25, 26]. The high velocity shock waves are generated in hydrogen or deuterium plasma. However, the shock waves in hydrogen or deuterium are not suitable for observation of excitation and ionization relaxation. On the other hand, experiments using high in-

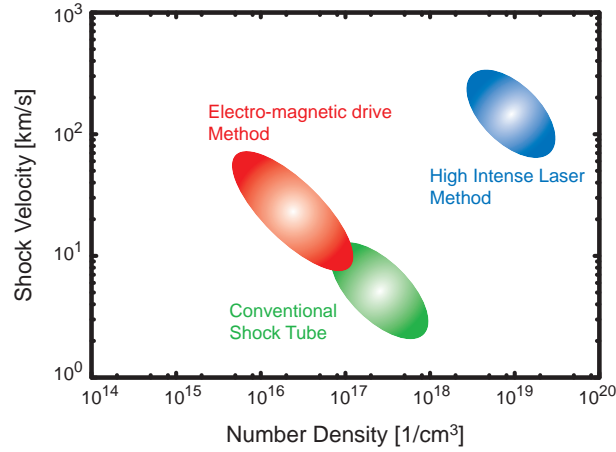


Figure 1.2: Shock parameters in Xe gas by different generating methods

tensity laser and their related simulations have been recently started [27–36]. They assume optically thick conditions, and the targets of these experiments are composed of high-Z element which is appropriate for radiation effect. However, the temporal and spatial scales of high intensity laser experiments are too small to observe the ionization relaxation. And then, our aim is understanding a strong shock structure with relaxation layer which consists of ion-electron energy relaxation, ionization relaxation, radiation effect in an optically intermediate region and their interplay among them.

For quantitative estimations of the structure formed by multi-scale relaxation processes, temporal and spatial scale of the generated shock structure need to be enough to measure it. Therefore, an electro-magnetic drive method which has larger scale length than those by the intense laser method is selected in this study. Essentially, the methods which deposit energy in different spatial and/or temporal scale length, generate the shock parameter in different parameter region. The shock wave parameters in Xe gas which can be approached by the electro-magnetic method, conventional shock tubes and intense laser methods are shown in Fig. 1.2. As shown in Fig. 1.2, the electro-magnetic drive method has a character of generating strong shock wave in comparatively low density gas. Strong shock wave with relaxation layer related to some dissipative processes in the low density has not been researched enough.

The steadiness and the geometrical simplicity are essentially important to quantitatively evaluate the complex shock structure. Then we have developed a device to make steady and 1 dimensional (1-D) shock waves (in more detail, see Sec.2.5.1). Through a comparative study of the steady and 1-D shock experiment and calculations based on the steady and 1-D shock wave, we estimate the strong shock structure with the relaxation region, which is the critical point of this thesis.

## 1.2 Similarity and Scaling of Laboratory Plasma to Astrophysical Phenomena

Astrophysical phenomena involve a great variety of physical processes occurring on very disparate temporal and spatial scales. In this section, as a first step to discuss similarity and scaling of laboratory plasma to astrophysical phenomena, we review briefly a similarity of hydrodynamic behavior under a condition, where two systems behave as ideal (i.e., without viscosity and thermal conductivity) compressible hydrodynamic fluids described by the Euler equations.

Ryutov *et.al.*, [7, 8, 10, 37] suggested “Euler number”:  $Eu = v(\rho/p)^{1/2}$  to scale up from laboratory experiment to astrophysical phenomena for velocity:  $v$ , mass density:  $\rho$ , and pressure:  $p$ . When initial state variables of the two systems have both similar dimensionless shapes and the similar parameters “Euler numbers” are equal each other, the hydrodynamical behavior described by the Euler equations can be similar. The identical hydrodynamic similarity between laboratory plasma and astrophysical phenomena holds even when they enter a nonlinear regime in their evolutions. Using “Euler numbers” for scaling, they discussed three cases related to SN 1987A: the exploding star [38–42], the young SNR [44], and the ring collision [45]. The exploding star corresponds to models of SN 1987A at a time of about 2000 s after the core collapse. In the young phase of the SNR, the parameters are appropriate to the shocked ejecta in SN 1987A at about 13 yrs. After that, in the ring collision phase, the expanding blast wave collides with a dense circumstellar ring. We show lines of Euler number:  $Eu = v(\rho/p)^{1/2}$  and plots for three phases of SN 1987 A and

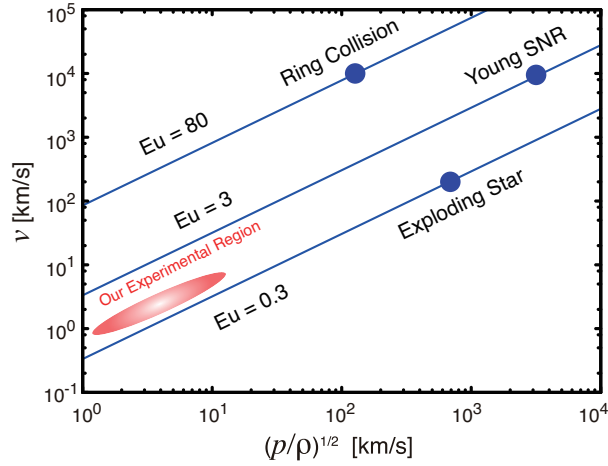


Figure 1.3: A similarity of identical hydrodynamical behavior between SN 1987A and our experiment based on Euler number [7]

our electro-magnetically driven shock waves in Fig. 1.3. As our experiment region is between exploding star phase and young SNR as identical hydrodynamic behavior in Fig. 1.3, it indicates a potential to scale up to the astrophysical phenomena. Simulating astrophysical phenomena with radiation effect is discussed in Sec. 5.4

### 1.3 Scope and Outline of Thesis

The aim of this thesis is to investigate the structure of electro-magnetically driven strong shock wave with relaxation layer. To estimate the structure, a steady and planar shock wave was driven by a compact pulse device, and the electron temperature and the scale length of the line emission from ions were measured. The ion population and ion and electron temperature distributions were calculated based on a steady and one-dimensional shock model. Since the non-linear nature of the relaxation process makes quantitative estimation of the shock wave extremely difficult, a comparative study between the experiment and the calculation was proposed. Based on the estimation by the comparative study, we showed basis for scaling to astrophysical phenomena.

The thesis started with an introduction to strong shock waves and their related

astrophysical phenomena. First we showed the motivation and background of this thesis, and similarity and scaling to astrophysical phenomena followed the introduction.

Chapter 2 presents physics and engineering concerning the formation of electromagnetically driven strong shock wave. First, we briefly review strong shock wave physics and advantages of electro-magnetic method as the shock driver. We demonstrate that well defined shock waves can be generated. The results show a potential of this method to estimate the shock structure with complex relaxation region.

Chapter 3 shows the method of calculations for evolution of the structure of strong shock wave with relaxation layer. Before the explanation of modelling, a short review of atomic processes is addressed. The model based on a steady and planar condition shows the estimation of ionization evolution and ion and electron temperature distributions in the shock heated region. For the comparative study, two fitting parameters are proposed that enables us to estimate the shock wave structure.

Chapter 4 explains the arrangement and results of electron temperature measurement by the line pair method. Before discussion of the results, the measurement principle and the experimental setup are explained. Results indicate that the electron temperature keeps almost constant value in the shocked region.

Chapter 5 describes the comparative study between the experiment and the calculations. The physical processes in the shock wave are estimated based on the comparison. The results indicate that atom-atom collision plays a critical role both for the formation and evolution of strong shock wave and radiative cooling restricts the increase of electron temperature. Moreover, a relation between our experiment and radiative SNRs is discussed for scaling of laboratory experiments to astrophysical phenomena.

Finally, in Chapter 6, we summarize these results with a roundup of newly established findings and understandings on the shock wave physics and conclude this study.

# Chapter 2

## Formation of Electro-magnetically Driven Strong Shock Waves

Since relaxation layer of strong shock wave is related to many processes, the estimation of the structure is complicated. Then, we need to generate steady and geometrically simple shock wave. In this chapter, the formation of the shock wave in this study is addressed. After a short review of shock wave physics, we show the experimental setup together with basic results on the front speed measurements.

### 2.1 A Short Review of Strong Shock Wave Physics

In this section, a short review of shock wave physics is addressed. Especially, when it is formed in a low density, high-Z medium, the structure is affected by multi-scale relaxation processes. We focus the related relaxation processes and characteristic times of them.

#### 2.1.1 Shock Wave and Rankine-Hugoniot Relations

When small disturbances of density and pressure are induced in a compressive medium, they propagate into the ambient medium. In case of the changes of the density and pressure with the fluid motion are small enough in comparison to the

average values of the density and pressure, and the flow velocity is small enough in comparison to the speed of sound, this wave is called “acoustic wave” and the disturbance propagates with the speed of sound. In the limited case, the changes are adiabatic and not dissipative.

On the contrary, when the propagation velocity is higher than the speed of sound and the disturbances of the thermodynamic parameters are large enough, the process through the wave is not adiabatic and this wave is called “finite wave”. In term of compression, the temperature and velocity gradients become so large that dissipative processes such as conductive heat transfer and friction become important. These diffusive processes counteract the steeping tendency of the finite wave. The opposing effects achieve a balance and the compression regions of the wave become stationary, in the sense that the wave propagates without a further distortion. This is “shock wave” [9]. For “finite wave”, the behavior of compression and expansion wave have significant differences. The expansion wave tends to flatten the disturbance, so it further reduces the velocity and temperature gradients, and can not achieve the stationary structure. In other words, it remains isentropic, and, generally, there are no expansion shocks.

In compression area, the isentropic relations are valid only up to a time that conductive heat transfer and friction become significant. Once diffusive and steepening effects reach a stationary balance, the condition across the “shock wave front” can be given by “The Rankine-Hugoniot Relations”. In case of calorimetrically perfect gas, the Rankine-Hugoniot Relations means that the increase in entropy is determined only by the conditions of conservation of mass, momentum, and energy and by the thermodynamic properties across the structure, and is entirely independent of the dissipative mechanisms causing this increase.

Here, we show the Rankine-Hugoniot Relations. The Euler equations in mass,

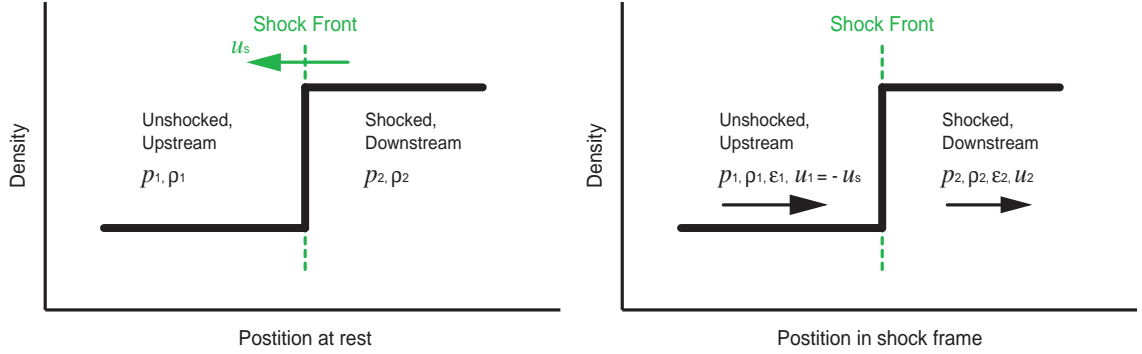


Figure 2.1: A steady shock at rest and that in moving frame with the front speed

momentum and energy conservation forms are shown as follows [10, 46]:

$$\frac{\partial \rho}{\partial t} = -\nabla \cdot (\rho \mathbf{u}), \quad (2.1)$$

$$\frac{\partial \mathbf{u}}{\partial t} + (\mathbf{u} \cdot \nabla) \mathbf{u} = -\frac{1}{\rho} \nabla p, \quad (2.2)$$

$$\frac{\partial}{\partial t} \left( \rho \epsilon + \frac{\rho u^2}{2} \right) = -\nabla \cdot \left[ \rho \mathbf{u} \left( \epsilon + \frac{u^2}{2} \right) + p \mathbf{u} \right], \quad (2.3)$$

where  $\rho$  is the density,  $\mathbf{u}$  is the velocity,  $p$  is the pressure,  $\epsilon$  is the specific internal energy, respectively.

To derive the Rankine-Hugoniot Relations, we assume a planar and steady condition as illustrated in Fig. 2.1. Then, the conservation Eqs. (2.1), (2.2), and (2.2) are changed from the frame at rest to the position at shock frame and they are simplified to the following as

$$\rho_1 u_1 = \rho_2 u_2, \quad (2.4)$$

$$\rho_1 u_1^2 + p_1 = \rho_2 u_2^2 + p_2, \quad (2.5)$$

$$\rho_1 u_1 \left( \epsilon_1 + \frac{u_1^2}{2} \right) + p_1 u_1 = \rho_2 u_2 \left( \epsilon_2 + \frac{u_2^2}{2} \right) + p_2 u_2, \quad (2.6)$$

where subscripts 1, and 2, denote the upstream and the downstream of the shock wave, respectively. The equation of state for a perfect gas and the gas constant  $R$

per unit mass are

$$p = \rho RT, \quad (2.7)$$

$$R = \mathcal{R}/\mu, \quad (2.8)$$

where  $\mathcal{R}$  is the universal gas constant and  $\mu$  is the atomic weight. From Eqs. (2.4), (2.5), (2.6), and (2.7), the Rankine-Hugoniot Relations are derived as

$$\frac{\rho_2}{\rho_1} = \frac{(\gamma - 1)p_1 + (\gamma + 1)p_2}{(\gamma + 1)p_1 + (\gamma - 1)p_2}, \quad (2.9)$$

$$\frac{T_2}{T_1} = \frac{p_1 (\gamma - 1)p_1 + (\gamma + 1)p_2}{p_2 (\gamma + 1)p_1 + (\gamma - 1)p_2}, \quad (2.10)$$

where  $\gamma$  is the specific heat ratio and we assume a calorimetrically perfect gas: i.e.,  $\gamma$  is constant through the shock. We define the shock Mach Number  $M$  shown as

$$M = \frac{u_s}{a_1}, \quad (2.11)$$

where  $u_s$  is shock speed and  $a_1$  is the speed of sound at the upstream region. The Rankine-Hugoniot Relations are modified using the shock Mach Number  $M$  and they are the following as

$$\frac{p_2}{p_1} = \frac{2\gamma}{\gamma + 1}M^2 - \frac{\gamma - 1}{\gamma + 1}, \quad (2.12)$$

$$\frac{\rho_2}{\rho_1} = \frac{(\gamma + 1)M^2}{2 + (\gamma - 1)M^2}, \quad (2.13)$$

$$\frac{T_2}{T_1} = \frac{[2 + (\gamma - 1)M^2][2\gamma M^2 - (\gamma - 1)]}{(\gamma + 1)^2 M^2}. \quad (2.14)$$

In the case of  $M \rightarrow \infty$ , these equations are reduced to the following forms:

$$\frac{p_2}{p_1} \rightarrow \frac{2\gamma}{\gamma + 1}M^2, \quad (2.15)$$

$$\frac{\rho_2}{\rho_1} \rightarrow \frac{\gamma + 1}{\gamma - 1}, \quad (2.16)$$

$$\frac{T_2}{T_1} \rightarrow \frac{2\gamma(\gamma - 1)}{(\gamma + 1)^2}M^2. \quad (2.17)$$

These Eqs. (2.15), (2.16), and (2.17) show that when we drive a strong shock wave, the pressure ratio and the temperature ratio across the shock discontinuity increase with  $\sim M^2$ . However, the density ratio approaches a finite value.

### 2.1.2 Plasma Shock Waves and Relaxation Times of Coulomb Interaction

In a neutral gas, relaxation time for establishing a Maxwell velocity distribution is characterized by the collision time between the fluid particles. Their cross sections  $\sigma_{cs}$  are approximately  $\sigma_{cs} \sim \pi r^2$ , where the radius  $r$  is of the order of the electron orbit.

On the contrary, when fluid becomes a plasma, the particles are composed of ions and electrons. The character of relaxation time in plasma is different from that of neutral gas, because the Coulomb forces decrease very slowly with distance, and don't have a characteristic length scale. Therefore, the collision times between the charged particles and the corresponding relaxation times must be considered separately. Another important is the mass difference between ion and electron. This also plays a significant role for relaxation process in the charged gas. Since the ions masses  $m_i$  are larger completely than the electron masses  $m_e$ , the energy transfer during a collision between an ion and an electron is the fraction of the order of  $m_e/m_i \ll 1$ . The ions and electrons temperatures which are connected to the average kinetic energies of ions and electrons, are different in most cases from one another's temperatures over a long time period. Thus the two factors, the long range in which Coulomb forces act and the mass differences between ions and electrons, determine the plasma properties.

The structure of plasma shock waves reflects the basic relaxation processes in plasma as above. That is associated with the inefficient momentum exchange between ions and electrons and with the high electron mobility. Maxwellian distributions in the ions and electrons themselves are formed quite rapidly, in a time of the order of particle collision time, which mean that the ion temperature  $T_i$  and the electron temperature  $T_e$  can be defined in most plasma. On the other hand, it takes much longer time to the equilibration of the temperatures between ions and electrons which means  $T_i = T_e$  due to the ions and electrons mass differences.

Here, a simple estimation of the cross-section in electron - ion collision is shown [47]. When an electron with velocity  $v_e$  approaches a fixed ion of charge  $Z_i$  as in

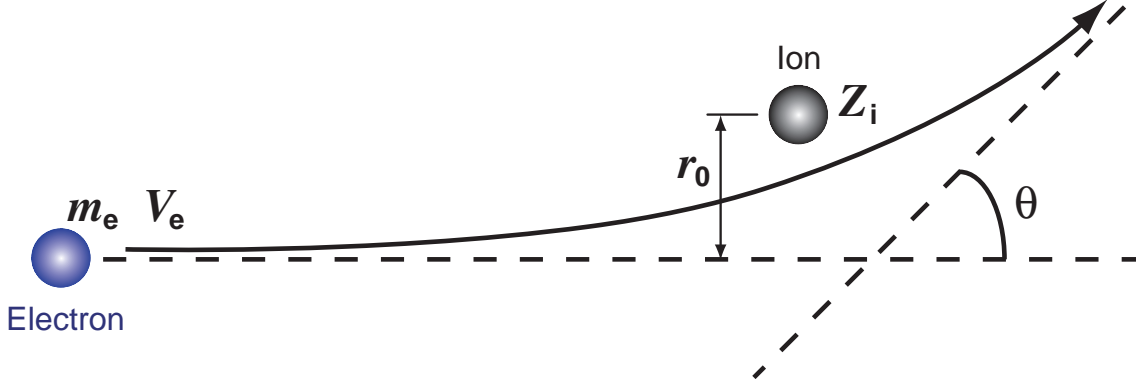


Figure 2.2: An electron orbit by Coulomb interaction

Fig. 2.2, the Coulomb force deflects the electron by an angle  $\theta$ , which is related to  $r_0$  called “impact parameter”. The momentum change  $\Delta(m_e v_e)$  of the electron is approximately described as shown in

$$\Delta(m_e v_e) = |F \Delta t| \approx \frac{Z_i e^2}{4\pi\epsilon_0 r_0^2} \frac{r_0}{v_e}, \quad (2.18)$$

where  $F$  is Coulomb force,  $\Delta t$  is interaction time and  $\epsilon_0$  is the vacuum permittivity. The change of momentum  $\Delta(m_e v_e)$  for  $\theta \sim \pi/2$  scattering, is of the order of  $m_e v_e$ . Then, we can get the relation between  $v_e$  and  $r_0$  as,

$$\Delta(m_e v_e) \approx m_e v_e \approx \frac{Z_i e^2}{4\pi\epsilon_0 r_0^2} \frac{r_0}{v_e}, \quad (2.19)$$

$$r_0 = \frac{Z_i e^2}{4\pi\epsilon_0 m_e v_e^2}. \quad (2.20)$$

The cross section  $\sigma_{cs}$  for  $\theta \sim \pi/2$  scattering of electron in Coulomb field is

$$\sigma_{cs} = \pi r_0^2 = \frac{Z_i^2 e^4}{16\pi\epsilon_0^2 m_e^2 v_e^4}. \quad (2.21)$$

Then, the collision time  $t_c(e, i)$  based on the  $\theta \sim \pi/2$  scattering is shown as

$$t_c(e, i) = \frac{1}{N \sigma_{cs} v_e} = \frac{16\pi\epsilon_0^2 m_e^2 v_e^3}{N Z_i^2 e^4}, \quad (2.22)$$

$$\approx \frac{m_e^{1/2} (4\pi\epsilon_0)^2 (k_B T_e)^{3/2}}{\pi N Z_i^2 e^4}, \quad (2.23)$$

where  $N$  is number density.

In case of Coulomb interaction in plasma, small-angle scatterings are much more frequent because the characteristic length of Coulomb force is long. The cumulative effect of many small-angle deflections turns out to be larger than the effect of large-angle single collisions. In order to consider the multi-scattering effect, a fundamental parameter was introduced within the framework of the binary collision approximation. A rigorous analysis of the interaction with Coulomb logarithm  $\ln\Lambda$  was developed by Spitzer [48] as,

$$\Lambda = \overline{\lambda_D/r_0}, \quad (2.24)$$

with  $\lambda_D$  as the Debye length and  $r_0$  means the impact parameter defined by Eq. (2.20). The Coulomb logarithm represents the Coulomb interaction region from lower limit  $r_0$ , which is the minimum distance to which the particles can approach each other, to upper limit  $\lambda_D$ , in which electric field is screened off by the simultaneous action of the positive and negative charges [10]. Electron-electron  $t_{\text{eq}}(e, e)$ , ion-ion  $t_{\text{eq}}(i, i)$ , electron-ion  $t_{\text{eq}}(e, i)$ , and ion-electron  $t_{\text{eq}}(i, e)$  relaxation times are derived using similar consideration in SI unit as

$$t_{\text{eq}}(e, e) = \frac{3m_e^{1/2}(4\pi\epsilon_0)^2(k_B T_e)^{3/2}}{4(\pi)^{1/2}N_e e^4 \ln\Lambda} \quad (\text{s}), \quad (2.25)$$

$$t_{\text{eq}}(i, i) = \frac{3m_i^{1/2}(4\pi\epsilon_0)^2(k_B T_i)^{3/2}}{4(\pi)^{1/2}N_i Z_i^2 e^4 \ln\Lambda} \quad (\text{s}), \quad (2.26)$$

$$t_{\text{eq}}(e, i) = \frac{3m_i(4\pi\epsilon_0)^2(k_B T_e)^{3/2}}{8(2\pi)^{1/2}m_e^{1/2}N_i Z_i^2 e^4 \ln\Lambda} \quad (\text{s}), \quad (2.27)$$

$$t_{\text{eq}}(i, e) = \frac{3m_i(4\pi\epsilon_0)^2(k_B T_e)^{3/2}}{8(2\pi)^{1/2}m_e^{1/2}N_e Z_i^2 e^4 \ln\Lambda} \quad (\text{s}). \quad (2.28)$$

where  $m_i$  and  $m_e$  are ion and electron mass in kg,  $T_i$  and  $T_e$  are ion and electron temperatures in K,  $N_i$  and  $N_e$  are ion and electron number densities in  $\text{m}^{-3}$ ,  $Z_i$  is the ion charge,  $k_B$  is the Boltzmann constant in J/K, and  $e$  is elementary electric charge in C, and we assume  $T_e/m_e \gg T_i/m_i$ .

The ratios of ion-ion and electron-ion relaxation times to electron-electron relax-

ation time [49] are

$$t_{\text{eq}}(e, e) : t_{\text{eq}}(i, i) : t_{\text{eq}}(e, i) \sim 1 : \frac{1}{Z_i^3} \left( \frac{m_i}{m_e} \right)^{1/2} \left( \frac{T_i}{T_e} \right)^{3/2} : \frac{1}{2Z_i} \frac{m_i}{m_e}. \quad (2.29)$$

In case of  $T_e \sim T_i$  and low  $Z$ , Eq. (2.29) is simplified as

$$t_{\text{eq}}(e, e) : t_{\text{eq}}(i, i) : t_{\text{eq}}(e, i) (\sim t_{\text{eq}}(i, e)) \sim 1 : \left( \frac{m_i}{m_e} \right)^{1/2} : \frac{m_i}{m_e}. \quad (2.30)$$

Thus, in non-equilibrium plasma, electrons establish a Maxwellian within a few electron-electron collision times followed by ions within a few ion-ion collision times and finally, after the time of order of  $(m_i/m_e)t_{\text{eq}}(e, e)$ , equilibrium between electron and ion temperatures takes place. However, since the region of  $T_i > T_e$  remains in ion-electron relaxation layer of plasma shock wave, Eq. (2.30) does not provide always correct estimation [50].

### 2.1.3 Radiative Shock Waves and Characteristic Time for Radiation Flux

Shock wave in which the structure of temperature and density is affected by radiation from the shock-heated medium is called a “radiative shock” [14]. Although the high enthalpy flow include radiation effect, generally the contribution of radiation energy density  $\epsilon_{\text{rad}}$ , and radiation pressure  $p_{\text{rad}}$  are negligibly less than that of radiation flux  $F_{\text{rad}}$ . It is shown by the following rough approximation [10, 23],

$$\frac{F_{\text{rad}}}{F_{\text{cond}}} = \frac{\sigma T_r^4}{u_s \rho \epsilon_{\text{th}}} \sim \frac{c}{u_s} \frac{\epsilon_{\text{rad}}}{\epsilon_{\text{th}}}, \quad (2.31)$$

where  $F_{\text{cond}}$ ,  $\epsilon_{\text{th}}$ ,  $c$ , and  $u_s$  are, respectively, the heat conduction flux, the thermal energy density, the speed of light, and the shock velocity. Eq. (2.31) shows that the the radiation flux is significant even if the radiation energy density is negligible with respect to the thermal one, according to the large value of the ratio  $c/u_s$ . However, when the temperature of the downstream matter, which means behind the shock front, is very high and satisfies  $\epsilon_{\text{rad}} \sim \epsilon_{\text{th}}$ , we have to take into account of not only  $F_{\text{rad}}$  but also  $\epsilon_{\text{rad}}$  and  $p_{\text{rad}}$  in the equations [23, 51]. The radiation pressure  $p_{\text{rad}}$  and the

radiation energy density  $\epsilon_{\text{rad}}$  derived by the Stefan-Boltzmann law of radiation [11] are shown as

$$p_{\text{rad}} = \frac{1}{3}aT_{\text{r}}^4, \quad (2.32)$$

$$\epsilon_{\text{rad}} = aT_{\text{r}}^4, \quad (2.33)$$

where  $T_{\text{r}}$  is the radiative temperature of planckian distribution and  $a$  is radiation density constant in SI unit.

When we consider the radiation flux, the radiation pressure, and the radiation energy density in Eqs. (2.4), (2.5), (2.6), the radiation-modified Rankine-Hugoniot jump conditions are shown as [22, 23]

$$\rho_1 u_1 = \rho_2 u_2, \quad (2.34)$$

$$\rho_1 u_1^2 + p_{\text{th1}} + p_{\text{rad1}} = \rho_2 u_2^2 + p_{\text{th2}} + p_{\text{rad2}}, \quad (2.35)$$

$$\begin{aligned} \rho_1 u_1 \left( \frac{\gamma}{\gamma-1} \frac{p_{\text{th1}}}{\rho_1} + \frac{1}{2} u_1^2 \right) + u_1 (\epsilon_{\text{rad1}} + p_{\text{rad1}}) \\ = \rho_2 u_2 \left( \frac{\gamma}{\gamma-1} \frac{p_{\text{th2}}}{\rho_2} + \frac{1}{2} u_2^2 \right) + u_2 (\epsilon_{\text{rad2}} + p_{\text{rad2}}), \end{aligned} \quad (2.36)$$

where we assume that flow is steady and planar, the fluid is a completely ionized plasma which means  $\gamma$  is constant, and both the upstream and the downstream material is extremely optically thick. As usual the subscripts “1” and “2” denote upstream and downstream conditions, respectively. The last assumption represents that any radiation crossing the front from the hot downstream medium into the cooler upstream medium will be completely reabsorbed within a thin layer into which it can penetrate by diffusion. Moreover, the conditions outside the diffusion layer become homogeneous and the radiation fluxes,  $F_{\text{rad1}}$  and  $F_{\text{rad2}}$ , are zero.

When  $p_{\text{rad2}}$  becomes comparable to  $p_{\text{th2}}$  ( $p_{\text{rad2}} \sim p_{\text{th2}}$ ), we consider that the shock wave is radiatively affected. The criterion  $p_{\text{rad2}} \geq p_{\text{th2}}$ , which characterizes a full radiative regime with Eqs. (2.34), (2.35), and (2.36), derives a Mach number threshold and a shock velocity threshold [23, 35] for radiative dominant region as shown in SI

unit as,

$$u_s \geq D_{\text{rad}} = \left( \frac{7^7 k_B^4 N_1}{72a \mu_1^3} \right)^{\frac{1}{6}} \quad (\text{m/s}), \quad (2.37)$$

$$M_{\text{rad}} = \frac{7^2}{6} (6\gamma)^{-\frac{1}{2}} \alpha_r^{-\frac{1}{6}}, \quad (2.38)$$

where  $k_B$  is the Boltzmann constant in J/K,  $a$  is radiation density constant in  $\text{J/m}^3/\text{K}^4$ ,  $N_1$  is number density in the upstream region in  $\text{m}^{-3}$ ,  $\mu_1$  is the particle mass in kg,  $\gamma$  is the ratio of specific heat, and  $\alpha_r$  represents  $p_{\text{rad1}}/p_{\text{th1}}$ .

At last in this subsection, we consider the characteristic time  $t_{\text{rad}}$  which means the radiation energy flux is more significant than the hydrodynamical one. In the consideration, a slab plasma is assumed. As the radiative flux from the two surfaces of the planar slab is  $2F_{\text{rad}}$ , the plasma energy content per unit area of the slab surface is  $3/2(N_i k_B T_i + N_e k_B T_e)l$ , where  $l$  is the characteristic length of the slab plasma in m. The characteristic time  $t_{\text{rad}}$  is the ratio of radiation heat fluxes to the plasma energy density as shown in [27]

$$t_{\text{rad}} = \frac{3/2(N_i k_B T_i + N_e k_B T_e)l}{2F_{\text{rad}}} = \frac{3/2(N_i k_B T_i + N_e k_B T_e)l}{2\kappa l \rho \sigma T^4} \quad (\text{s}), \quad (2.39)$$

where,  $\kappa$  is specific opacity in  $\text{m}^2/\text{kg}$ ,  $\sigma$  is the Stefan-Boltzmann constant in  $\text{J/s/m}^2/\text{K}^4$ ,  $\rho$  is plasma mass density in  $\text{kg/m}^3$ . This ratio is for an optically thick material. Ryutov, Sutherland and Dopita [7, 52] also reported the cooling time in an optically thin region where the cooling is due to bremsstrahlung and the line radiation.

Here, when plasma is optically thick, in which the radiation flux behaves like a black body, and the ion temperature  $T_i$  is equal to the electron one. In case of black body, Eq. (2.39) is converted to a more simplified form as shown in [7]

$$t_{\text{rad}} = \frac{3/2(Z_i + 1)(N_i k_B T)l}{2\sigma T^4} \quad (\text{s}), \quad (2.40)$$

where  $Z_i$  is the ion charge and  $T$  is plasma temperature in K, respectively.

### 2.1.4 Initial Ionization in Strong Shock Waves

The thickness of the compression shock wave is approximately two to three of gasketic atomic mean free paths. Ionization occurs after the shock compression

and rapid heating of the particles. The basic ionization mechanism is ionization by electron collision (in more detail, see Sec. 3.1.1). However, ionization by electron collision with the formation of an electron avalanche requires the presence of some initial “priming” electrons [10]. One of the mechanisms which can lead to this initial ionization is by atom-atom collisions. Ionization processes in low energy atomic collision cross section were reported from both theoretical studies [53, 54] and beam experiment [55].

Some experimental data using conventional shock tube [56–62] about initial ionization were published. However, the experimental data did not enough agree with the avalanche ionization calculations [10]. It is shown that ionization as a result of atom-atom ionization collision or photoionization by photons from shock heated region cannot ensure the rapid formation of the large number of priming electrons which are required to explain the experimental data. Thus, the mechanism of the initial ionization in strong shock wave has not been understood. In strong shock formation at the low density region, atom-atom process is considered to be significant for the initial ionization. As has been described in Sec. 1.1, electro-magnetically driven method can be considered to be a good tool to investigate it.

### 2.1.5 Structure of Strong Shock Waves

Here, we show a sketch of temperature distributions of steady and planar shock wave in Fig. 2.3. Fig. 2.3(a) represents a temperature distribution of a simple hydrodynamical shock wave. The fluid is compressed and heated by the shock and the structure is uniform and has no relaxation layer. In higher shock velocity, the fluid behind shock becomes plasma as shown in Fig. 2.3(b). As above, the plasma shock wave has ion-electron relaxation layer because of inefficient momentum exchange between ion and electron. When the shock wave is further strengthened and radiation effect cannot be ignored, the temperature distribution is modified by radiative energy like in Fig. 2.3(c). Shocks in this region are expected to have precursor region and radiative cooling region with ion-electron relaxation and ionization relaxation. The precursor is expected to be formed by electron heat conductivity and/or photoioniza-

tion process. The characteristic length of precursor by electron heat conductivity is order of the thickness of the relaxation region in which the electron and ion temperatures equilibrate [10] and the length by photoionization characterized by the order of photon mean free path.

## 2.2 Methods of Generating Strong Shock Waves

As shown in Sec. 1.1, we chose an electro-magnetic method for generating the strong shock wave, because the temporal and spatial scale of the shock structure in the electro-magnetic device is appropriate to observe the high temperature non-equilibrium plasma. The driving source of this method is discharge produced magnetic pressure. In this section, a relevant magneto-hydrodynamics is briefly reviewed and the shock formation methods including electro-magnetic one is addressed.

### 2.2.1 Magnetic Pressure

A simplified form of plasma equation of motion is considered. Here, we neglect gravitational force with the help of mass, momentum and current equations, and then the equation of motion can be written simply [47]

$$\rho \left( \frac{\partial \mathbf{v}}{\partial t} + (\mathbf{v} \cdot \nabla) \mathbf{v} \right) = \mathbf{j} \times \mathbf{B} - \nabla p, \quad (2.41)$$

where  $\rho$  is the plasma density,  $\mathbf{v}$  is the velocity,  $\mathbf{j}$  is the current density,  $B$  is the magnetic field,  $p$  is the gas kinetic pressure. The Ampere's law gives the equation as shown in

$$\text{rot} \mathbf{B} = \mu_0 \mathbf{j}, \quad (2.42)$$

where  $\mu_0$  is magnetic permeability. We substitute Eq. (2.42) into Eq. (2.41) to obtain

$$\rho \left( \frac{\partial \mathbf{v}}{\partial t} + (\mathbf{v} \cdot \nabla) \mathbf{v} \right) = \left[ \frac{1}{\mu_0} (\mathbf{B} \cdot \nabla) \mathbf{B} - \nabla \left( \frac{\mathbf{B}^2}{2\mu_0} \right) \right] - \nabla p. \quad (2.43)$$

The first term on right-hand side represents magnetic tension forces, however, it is negligible in many cases because  $\mathbf{B}$  does not vary along  $\mathbf{B}$ . The second term is the

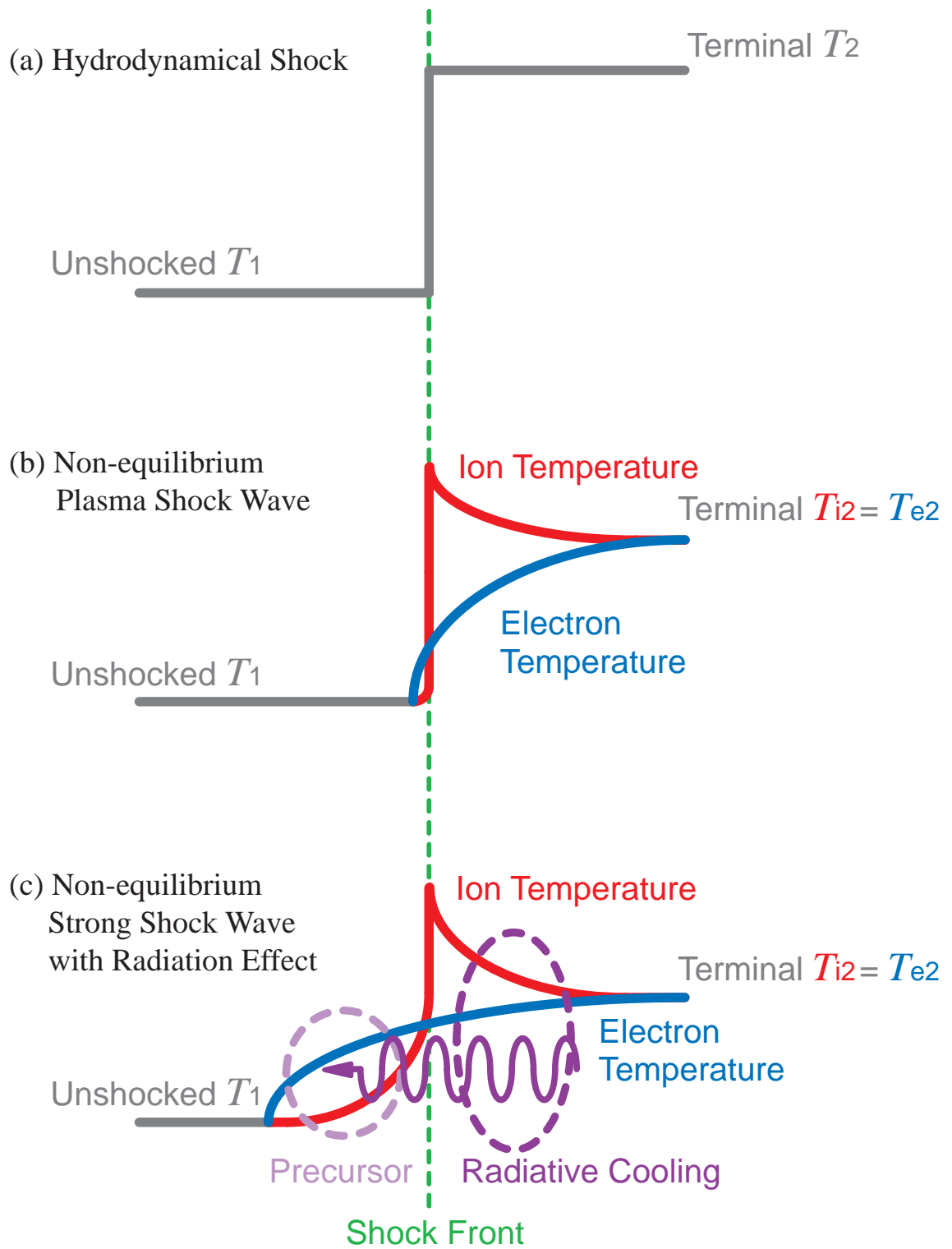


Figure 2.3: Temperature distributions of steady and planar shock wave

magnetic pressure. Therefore, Eq. (2.43) says that

$$\rho \left( \frac{\partial \mathbf{v}}{\partial t} + (\mathbf{v} \cdot \nabla) \mathbf{v} \right) = -\nabla \left( \frac{B^2}{2\mu_0} + p \right). \quad (2.44)$$

This Eq. (2.44) means that the dynamical source of magneto-hydrodynamical plasma is gradient of magnetic pressure and gas kinetic pressure. The maximum shock velocity which is accessible by the conventional shock tube is limited because the dynamical source is only the gas pressure of driver gas. Whereas, since the electro-magnetic method can drive a large current in a local region, the gradient of magnetic pressure can be extremely large. In case of the localized plasma current, the magnetic field  $B$  is

$$B \sim \frac{I}{r}, \quad (2.45)$$

where  $I$  is the discharge current and  $r$  is a characteristic length. Thus, it is important for forming a strong shock wave that the discharge current is large and the characteristic length is small. (in more detail, see Appendix. 2.4.1). This magnetic pressure is the primary dynamical source for the shock formation in this study.

## 2.2.2 Plasma Focus

The basic concept of our experimental device is based on plasma focus systems. The plasma focus [63] consists of a cylindrical column anode at the center, a tubular cathode surrounding the anode and an insulator between the coaxial electrodes. Fig. 2.4 shows a sketch of typical plasma focus device. Initially, the region between the electrodes is filled with a gas. When a high voltage is applied, a flashover discharge is induced on the insulator and the current passes radially from the anode to the cathode, and then the discharged plasma, which is called a “current sheet”, is formed. This current sheet accelerated by the magnetic pressure compresses the initial gas in front of the sheet and a shock wave is formed. In Fig. 2.4, since the current density in the inner electrode: the anode, is higher than that in the outer electrode: the cathode, the current sheet is expanding spherically with time. When the current sheet achieve the top of the central electrode, the pinch process is induced. The process forms high

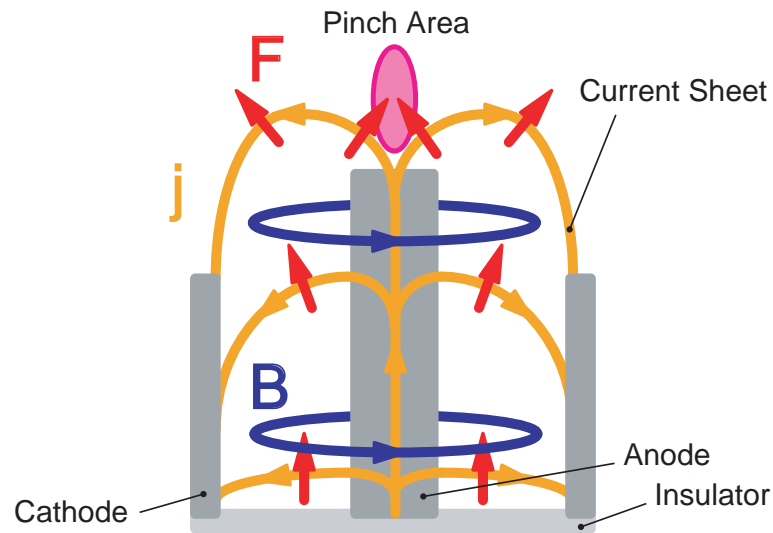


Figure 2.4: A sketch of a plasma focus device

energy density plasma. The plasma focus system has been developed originally for studies on neutron sources [64] and recently for intense light sources [65].

### 2.2.3 Electro-magnetically Driven Method

A T-tube built by Kolb [25] utilizes the electromagnetic interaction between currents for accelerating a gas plasma. As shown in Fig. 2.5, the lead carrying the return current in the discharge circuit is placed close to the discharge part of the T-tube [10]. A strong repulsive force exists between parallel conductors carrying oppositely directed currents. This force can be regarded as the result of the magnetic pressure derived in Sec. 2.2.1. The magnetic pressure gradient is perpendicular to the direction of the current and the magnetic field. The drive source repels the plasma carrying the discharge current in the direction of the vertical part of the tube, and imparts an additional acceleration to the plasma. The principle of the magnetic pressure drive for shock wave formation is also used in another shock tube developed [66,67].

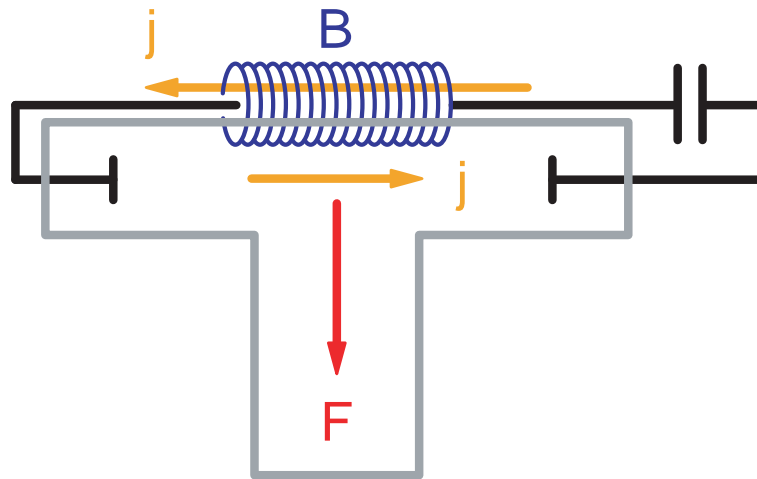


Figure 2.5: A sketch of conventional electro-magnetic shock tube

## 2.3 Experimental Setup

We drive the shock wave by the electro-magnetic method shown in Sec. 2.2.3. Fig. 2.6 gives a sketch of the experimental device. Here, we show the flow of the shock wave formation and experimental steps below briefly.

The electro-magnetic energy of capacitors charged by a power supply inputs the power pulse into the gas (Here, Xe gas) between electrodes through a spark gap switch and the magnetic pressure drives the shock wave. A pair of tapered electrodes are used in our device to guide and strengthen the electro-magnetically driven shock wave. The shock wave is formed in the tapered electrode and propagates upward through the guiding tube. In this time, a fast framing and streak camera (Imacon 468) takes the self emission from the propagating shock wave and we estimate the shock front velocity.

In the following subsection, characteristics of the experimental device are shown.

### 2.3.1 Electro-magnetic Device

A compact pulse power device was constructed for generating electro-magnetic pulse. The energy suppliers are the twelve plastic capacitors [Maxwell Laboratories,

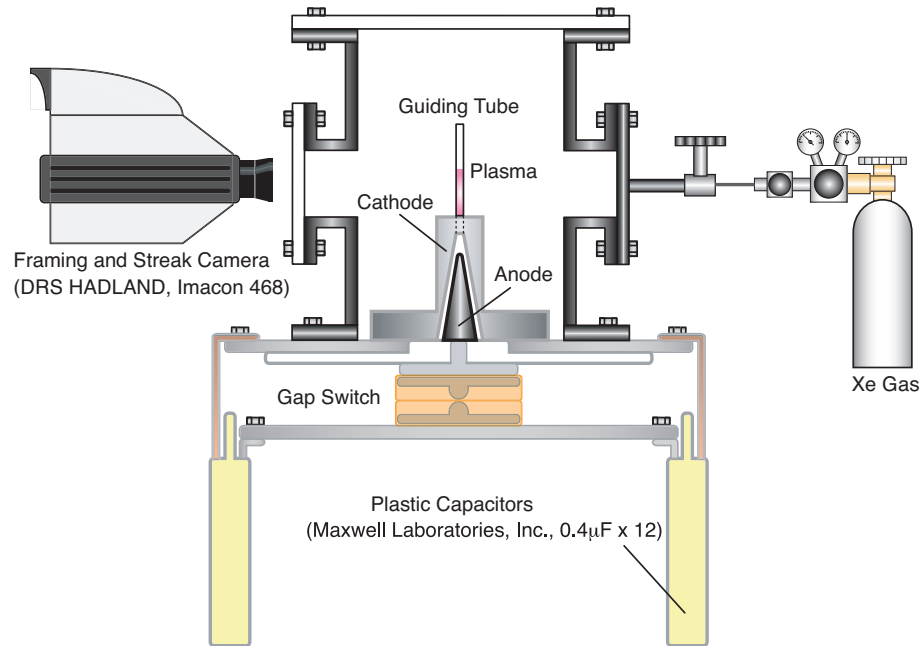


Figure 2.6: A sketch of the experimental setup

Inc.,  $0.4 \mu\text{F}$ ,  $50 \text{ kV}$  (max)], which are cylindrically arranged to reduce the inductance. Each wiring fixed tightly by conductor plates to reduce the residual resistance. Since the drive force, which is magnetic pressure, is in proportion to square of the discharge current, low inductance and resistance is essential for driving a large discharge current.

The gap switch was placed between the anode and the high voltage side of capacitors as shown in Fig. 2.6. The switch was operated with self-breakdown mode, to ensure low resistivity and fast switching. It was composed of two plane conductors with hemispherical electrode and plastic insulator. The spark discharge starts out from cathode to anode when the voltage between the electrodes is over a breakdown threshold. The accelerated electrons ionize the insulator gas and supply additional electrons. The chain reaction induces electron avalanche and finally forms a low resistance current path [68,69]. The relation of discharge voltage  $V_{\text{dis}}$  to the gap distance:  $d$ , and the pressure of the insulator gas:  $p$  is approximately given by the Paschen's

law as,

$$V_{\text{dis}} \propto pd. \quad (2.46)$$

When the gap distance is  $d = 6$  mm and the pressure is  $p = 0.2$  MPa of  $\text{N}_2$  gas, the discharge voltage was measured to be 20 kV.

In our surroundings, the operating of the device over 20 kV was unstable. For keeping the shock velocity condition constant, we added an oil capacitor (SHIZUKI ELECTRICAL MFG. Co., Ltd., CAFFA,  $4.45\mu\text{F}$ ) and operated the device with lower discharge voltage:  $\sim 17$  kV. After this modification, the gap was normally operated with atmospheric air.

### 2.3.2 Tapered Electrodes and Guiding Tube

In Sec. 2.2.2, we showed that in a conventional discharge device, the produced shock wave as well as the current sheet spreads spherically and decays without a controlling method. The sketch of the tapered electrodes and the guiding tube is shown in Fig. 2.7. The cross section of the discharge area of our device is gradually decreased with a pair of tapered electrodes and, an acrylic guiding tube with a constant cross section is located on the top of the tapered electrodes to generate a 1-dimensional and strong shock wave [70]. The base diameter and the height of the conical anode are 20 and 45 mm and those of the cathode are 25 and 60 mm, respectively. The distance between electrodes is selected to be 5 mm considering the discharge condition: voltage is  $\sim 20$  kV and the pressure  $\sim$  Torr. The height of electrode (60 mm) is determined by typical shock wave velocity of  $\sim 10$  km/s and discharge current period of  $\sim \mu\text{s}$ . The top of anode is rounded with 1.5 mm radius. Both electrodes are made of stainless steel. A polyacetal disk insulates the electrodes. The acrylic tube is connected with the cathode by a screw thread. The outside and inside diameters of the tube are 8 and 4 mm, respectively. The detail of the driven shock wave is addressed in Sec. 2.5.1.

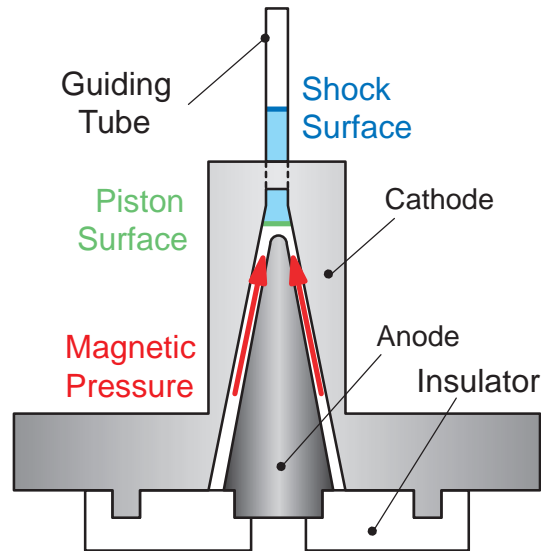


Figure 2.7: Schematic of the tapered electrodes and the guiding tube

## 2.4 Measuring instruments

The discharge current is measured by a Rogowski coil. The initially filled gas is Xe in this experiment. Since Xe is a monatomic gas, there is no degrees of freedom of vibration and rotation. In addition, as it has low ionization energy among noble gases and is heavy element, whose speed of sound is very low:  $\sim 180$  m/s at room temperature, it is appropriate to estimate the shock structure: i.e., ionization relaxation and radiation effect. To change the shock Mach number, the initial pressure of the gas is controlled for a range of 0.1 - 8 Torr by a rotary pump [ULVAC, Inc., D-330] and measured by a capacitance gage [PFEIFFER VACUUM, Inc., CMR 263 or CMR 264]. The leak rate of the vacuum chamber is less than  $3 \times 10^{-3}$  Torr/min and impurity ratio is estimated to be less than 10% even at the lowest initial pressure condition. The gas in the vacuum chamber is purged once with each test, pumped to  $10^{-3}$  Torr. In the following subsections, we explain the current probe, equivalent circuit of the experimental arrangement and the Fast Framing and Streak Image Camera.

### 2.4.1 Current Probe and Discharge Current

Rogowski Coil, which is appropriate to measure large discharge current, is selected as the current probe in this experiment. As the discharge period of the experimental device is expected to  $\sim \mu\text{s}$ , we designed an external integration type Rogowski coil. The designed Rogowski coil was calibrated using a small pulser (See Appendix. A).

The discharge current is shown in Fig. 2.8 based on the calibrated Rogowski coil. As shown, the discharge current peaked about 160 kA at 0.9  $\mu\text{s}$ . We can roughly estimate accessible shock Mach number. When characteristic length  $r$  is  $\sim 0.01$  m and discharge current  $i$  is  $\sim 100$  kA, the magnetic pressure  $p_B$  is estimated as follows,

$$p_B = \frac{B^2}{2\mu_0} \sim \left(\frac{i}{r}\right)^2, \quad (2.47)$$

$$\sim 10^6 \quad (\text{Pa}), \quad (2.48)$$

where  $\mu_0$  is magnetic permeability. When initial pressure  $p_1$  in a vacuum chamber is 1 Torr  $\sim 10^2$  Pa, using the Rankine-Hugoniot relation:  $p_B/p_1 \sim M^2$ , the accessible shock Mach number  $M$  is estimated to be,

$$M \sim \sqrt{\frac{p_B}{p_1}} \sim 100. \quad (2.49)$$

This value is as large as ten times of shock Mach number generated by conventional shock tube and this device has potential to discuss the shock structure in much more extreme condition.

At last in this subsection, an equivalent circuit of the electromagnetic device is addressed. The equivalent circuit and block diagram of the device are shown in Fig. 2.9. Taking into account of the stray inductance  $L$  and residual resistance  $R$ , the equivalent circuit is considered to be a LCR circuit. The discharge current and effective values of  $L$  and  $R$  can be estimated from the calibrated Rogowski Coil. When we neglect the evolution of plasma resistance and inductance, the ideal discharge

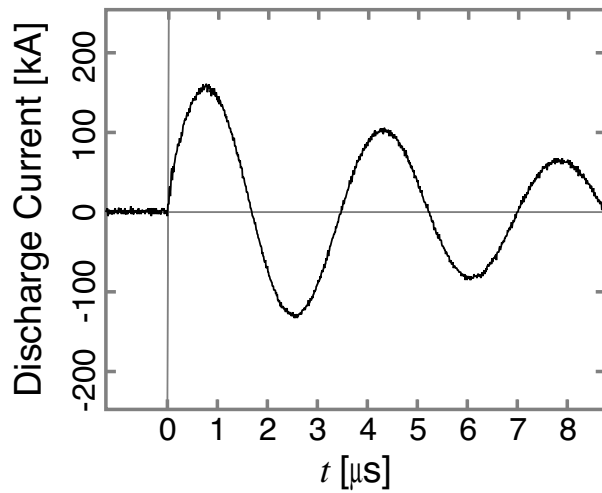


Figure 2.8: Typical discharge current waveform

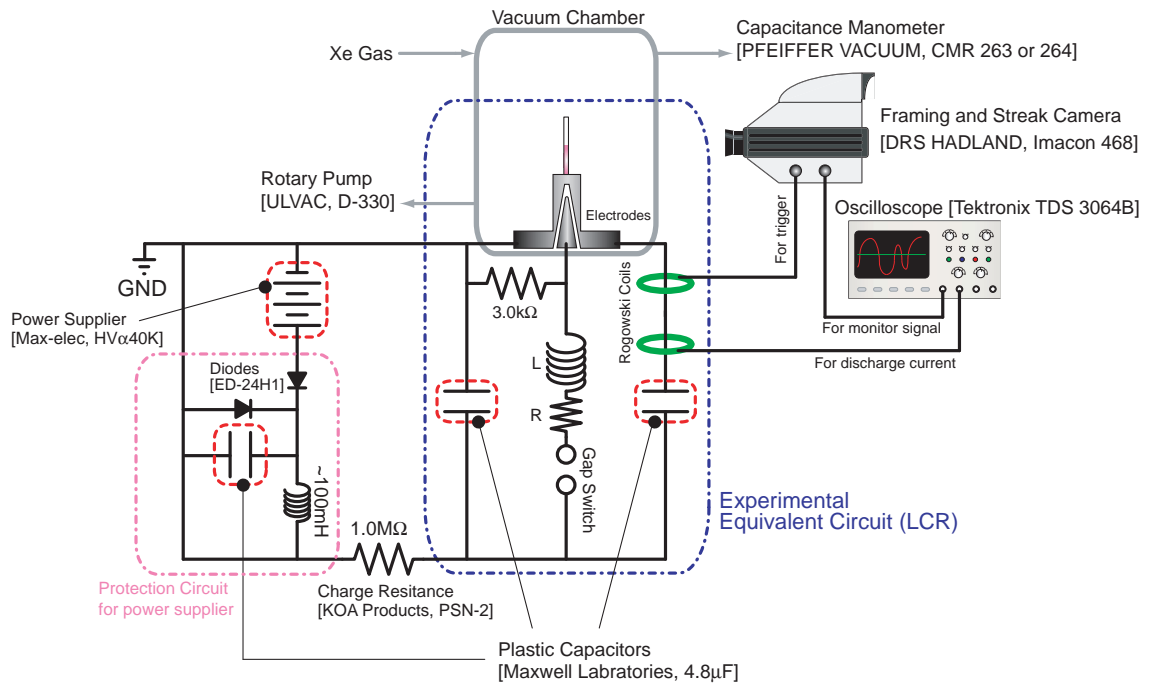


Figure 2.9: The equivalent circuit and block diagram of the device

current  $I$  in LCR circuit for an initial charge voltage  $V_0$  is analytically given by

$$I = \frac{V_0}{\omega_d L} \exp(\beta_0 t) \sin(\omega_d t) \quad (\text{A}), \quad (2.50)$$

$$\omega_d = \sqrt{\omega_0^2 - \beta_0^2} \quad (1/\text{s}), \quad (2.51)$$

$$\omega_0 = \frac{1}{\sqrt{LC}} \quad (1/\text{s}), \quad (2.52)$$

$$\beta_0 = \frac{R}{2L} \quad (1/\text{s}). \quad (2.53)$$

The discharge current shown in Fig. 2.8 can be fitted with the ideal wave form by the least squares method and this gives  $L \sim 70$  nH and  $R \leq 25$  m $\Omega$ . In spite of lower discharge voltage:  $\sim 17$  kV, due to the modification shown in Sec. 2.3.1, the shock front velocity for a same initial pressure was similar before.

## 2.4.2 Fast Framing and Streak Image Camera

The electro-magnetically driven shock wave is guided by the tapered electrodes and propagates through the guiding tube. The fast framing and streak image camera [DRS HADLAND, Ltd., Imacon 468] with lens [Nikon, Co., Ai AF Micro Nikkor 105mm F2.8D] takes the self emission profile of the shock wave during the propagation. The electric shutter established exposure time of 10 ns.

The trigger pulse is supplied by another Rogowski coil placed in the current path of the pulse power device. Another Rogowski coil is used without integration because the fast rising trigger pulse is desired. In order to make adjustments of the output voltage to appropriate value and prevent the signal from inversion, a pulse conditioner composed of a resistive voltage divider and a diode is used.

The camera in the framing mode can take four pictures at different timing. Thus, we can observe the shock image as a function of the discharge time. In this experiment, the exposure time was 10 ns.

In case of the streak mode, we can take a streak image of the vertical motion using image of the vertical streak slit. We observed evolutions of the emission pattern of the shock wave with streak sweep time 1  $\mu\text{s}$ .

## 2.5 Steady and One-dimensional Shock Waves and Self-emission Profiles

In this section, the electro-magnetically driven shock wave formation is given. As has been discussed in Sec. 1.1, steady and planar shock wave formation is of critical importance for investigation of the strong shock wave structure.

### 2.5.1 Formation of Steady and One-dimensional Shock Waves

As described in Sec. 1.1, the strong shock wave structure is affected by ion-electron energy transfer, ionization relaxation, radiation effect and their interplay. Because of complexity induced by the non-linear nature, quantitative estimation of the strong shock wave has not yet been established even in laboratories. Generation of the one-dimensional shock wave is important to make a well-defined condition. When steady and planar shock waves are generated, theoretical models [10, 22, 23] and calculations based on steady and planar condition may be appropriate to make comparative estimation of them and the above problem can be made clear. Here, we show that the electro-magnetically driven shock wave in our device satisfies steady and one-dimensional condition.

In Sec. 2.3.2, we showed basic structure of our device and indicated that the guiding tube with the constant cross section can realize steady and one-dimensional shock wave condition. Then, to confirm this advantage, we investigated the effectiveness of guiding tube by observing the images of the shock waves with and without the guiding tube. Plasma evolutions with and without the guiding tube are shown in Figs. 2.10(a) and 2.10(b). Initial pressure is 0.30 Torr and each flaming exposure time is 10 ns in both results. Here,  $t$  and  $z$  in Figs. 2.10(a) and 2.10(b) are the time after discharge start and vertical spatial scale in both framing and streak. The color pattern means that red is stronger and blue is weaker emissivity. Absolute intensity of the emission can not be discussed because sensitivities of the framing channels are different. However, relative intensity on each image can be investigated.

As in Fig. 2.10(a), the flaming pictures show that shock wave is spreading with

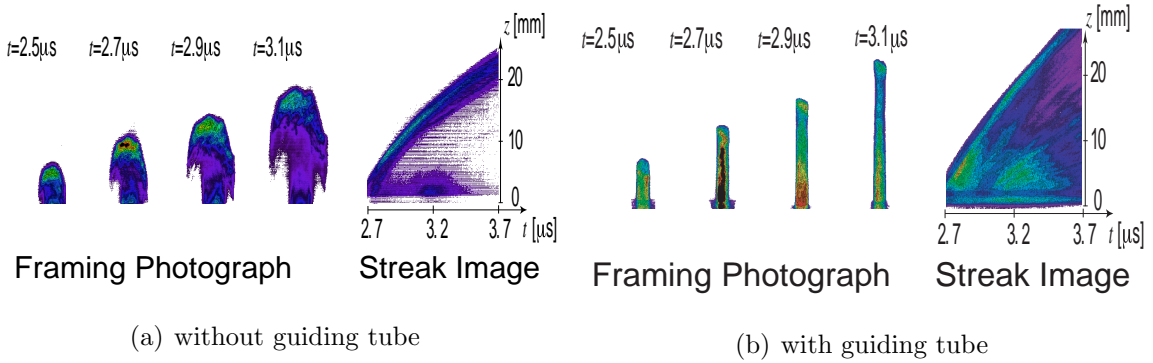


Figure 2.10: Framing and streak images of electro-magnetically driven shock waves

time. The streak image gives that the shock front velocity is  $\sim 28$  km/s in  $t \sim 2.7 \mu\text{s}$ , and  $\sim 17$  km/s in  $t \sim 3.2 \mu\text{s}$ . This result indicates that the shock wave decays with time without guiding tube.

On the other hand, the flaming pictures in Fig. 2.10(b) show that the shock is planar. Also the streak image in Fig. 2.10(b) displays that the shock velocity is constant with time, which means it is steadily propagating with mean velocity of 25 km/s. Thus, the guiding tube realizes formation of the steady and one-dimensional condition in the electro-magnetically driven shock wave [70].

## 2.5.2 Self-emission Profiles of Steady and One-dimensional Shock Waves

In Sec. 2.5.1, we confirmed that the electro-magnetically driven shock wave is steady and one-dimensional. Next, the shock images were observed as a function of the initial pressure with exposure time of 10 ns. The flaming and streak pictures taken in the condition of  $p_1 = 5.0$  Torr, 1.0 Torr, 0.50 Torr, and 0.10 Torr, which are the typical experimental condition, are shown in Figs. 2.11(a), 2.11(b), 2.11(c) and 2.11(d). The color table pattern is similar before.

The shock front mean velocity versus the change of initial pressure was obtained by the streak images. The relation between the shock front velocity and the corresponding shock Mach number, and initial pressure is shown in Fig. 2.12. The start

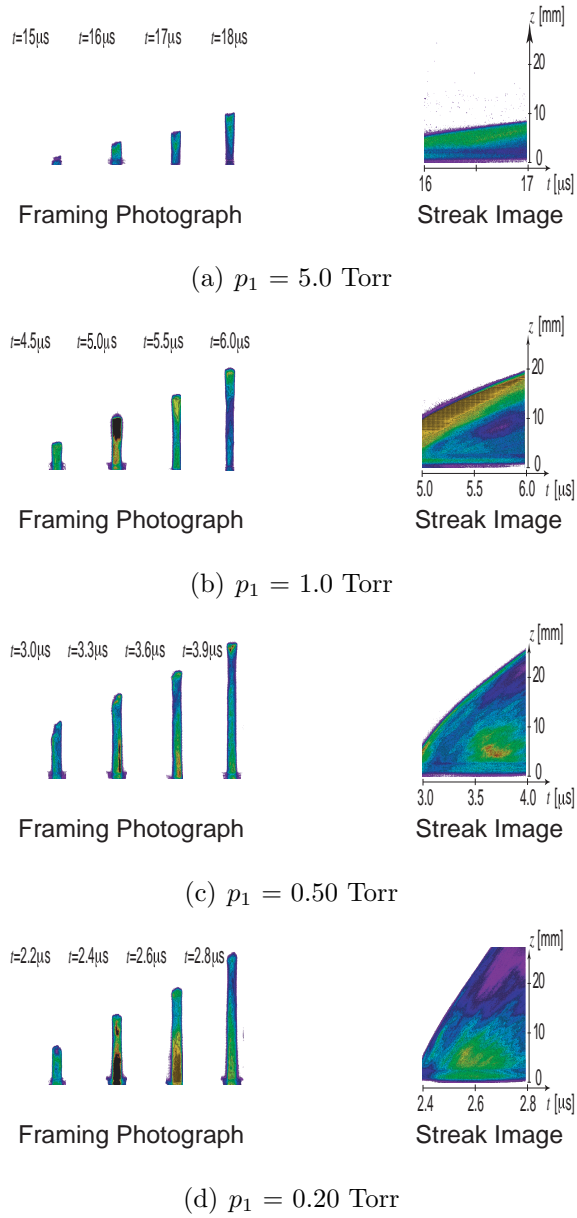


Figure 2.11: Framing and streak images of electro-magnetically driven shock wave in the guiding tube

edge of strong emission is assumed to be the shock front. The problem whether this is precursor or not is discussed in Sec. 5.1. Here, the shock Mach number  $M$  is normalized value of the front speed  $u_s$  by the speed of sound  $v_{Xe}$  of Xe at 300 K as shown in

$$M \equiv \frac{u_s}{v_{Xe}}, \quad (2.54)$$

where  $v_{Xe}$  at  $T = 300$  K is

$$v_{Xe} = \sqrt{\left. \frac{\partial p}{\partial \rho} \right|_s} = \sqrt{\gamma RT} \sim 180 \text{ (m/s)}. \quad (2.55)$$

$R$  is the gas constant as same as Eq. (2.8) and  $\gamma$  is 5/3 because Xe is monatomic gas.

Fig. 2.12 shows that the shock front velocity is hyperbolically decreasing with initial pressure, and Maximum shock Mach number exceeds 200 in low pressure condition. Of course, since high Mach number region dominated by relaxation processes, the simple scaling can not be extrapolated to this region. When we assume that the drive source, the magnetic pressure, is constant, the relation seems to correspond the scaling from the Rankine-Hugoniot relation,  $p_2/p_1 \sim M^2$  in Eq. (2.15).

The solid line in Fig. 2.12 means the shock velocity threshold  $D_{\text{rad}}$  derived by Eq. (2.37). As  $D_{\text{rad}}$  is function of only atomic number density, the line can be drawn.

Attention should be paid that the emission patterns between Figs. 2.11(a), 2.11(b) and Figs. 2.11(c), 2.11(d) are different. The radiation effect might be important, because in the low pressure region, the front speed exceeds the threshold  $D_{\text{rad}}$  [70]. This tendency is similar, when the target gas is Ar [71]. However, as  $D_{\text{rad}}$  is derived from the black body assumption, the real radiation contribution need to be investigated carefully. At least, as shown in Fig. 2.12, our experimental device generates stronger shock wave than it by conventional shock tube. In particular, this device is advantageous for formation of shock wave in lower density region than intense lasers. Since the mean free path is  $\sim$  mm in this density region, in addition to collisional relaxation process in conventional plasma shock waves: ion-electron and ionization relaxation processes, the effect of atom-atom collision process can be reflected in the emission pattern.

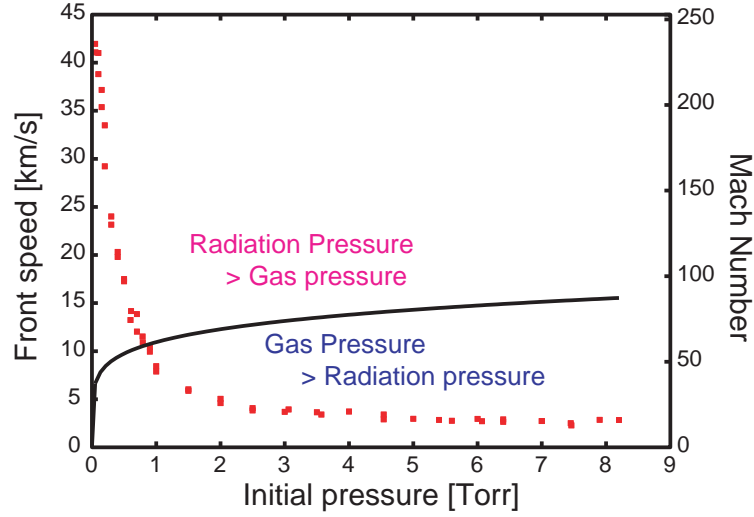


Figure 2.12: Initial pressure vs shock Mach number and shock speed

## 2.6 Concluding Remarks

In this chapter, first we briefly reviewed the physics relevant to strong shock wave and summarized the characteristic time scale of collisional process in the shock heated layer. We pointed out that the different physical parameters changes the dominant dissipative process and then the shock structure itself also changes. However, quantitative estimation of the structure is extremely difficult due to the non-linear nature of the relaxation process. Then, we proposed the electro-magnetically driven shock experiments and developed a compact pulse power device with tapered electrodes and a guiding tube. We have demonstrated that it can produce steady and one-dimensional high Mach number shock waves. The shock Mach number reached  $M \sim 200$  in low density Xe gas. In this region, it is indicated that radiative effect might contribute to the shock wave structure. Moreover, collisional relaxation processes also can be observed experimentally. We showed that the shock structure with relaxation layer can be investigated in the critical parameter region using our device because the accessible shock parameter is much different from conventional methods and generated shock wave is steady and planar.

## Chapter 3

# Calculation of Strong Shock Wave Structure Based on Steady and One-dimensional Condition

The strong shock wave structure is strongly connecting to relaxation processes. The elementary process of the relaxation are atomic processes. In this chapter, calculation of the atomic processes by rate equation is addressed. As previous chapter shows that the driven shock wave is steady and planar, the calculation can assume a steady and one-dimensional situation to make comparative study between the experiment and calculation. First, we show preparative introduction for the calculation, next for the modeling, and finally we discuss the calculation results.

### 3.1 Atomic Processes

The basic atomic processes of plasma are four: ionization, excitation, recombination, and deexcitation [72]. Atom in neutral has bound electrons which correspond to the atomic number. When a free electron provides enough energy by an interaction, the bound electron is stripped from the atom. This process is ionization. In case that the energy change of the interaction is weak, since bound electron can not receive the energy enough to ionize itself, it changes the distribution. When a free electron

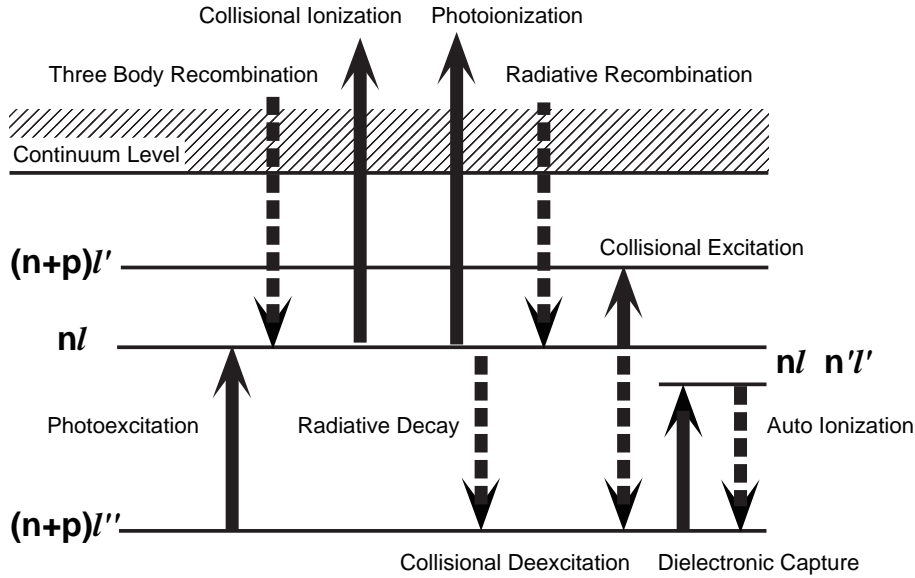


Figure 3.1: A sketch of atomic processes in plasma

loses energy, a neighbor ion captures the free electron. This process is recombination, which is the inverse action of ionization. A bound electron in high level state loses energy, the ion decays from upper to lower level. This is deexcitation, which is the inverse process of excitation. A schematic diagram of the four atomic processes is shown in Fig. 3.1. In Fig. 3.1, the solid lines mean the excitations of bound electron to upper levels or ionization to continuum, and the dashed lines mean the deexcitation process of bound electron to lower level or the recombination of free electron.

In the simulation, we assume that ions are only in ground states. Thus, considering atomic processes are only ionization and recombination: collisional ionization, three body recombination, radiative recombination, and photo ionization. Here, only electron-ion interactions are considered for the calculation. However, since atom-atom interaction may play an important role for weakly ionized plasma which is expected to be dominant in shock front vicinal region (in more detail, see Sec. 2.1.4 and 3.4.4), the semiclassical formula for ionization by neutral-neutral collisions is addressed [54]. Then, collisional excitation and collisional deexcitation is also shown because Local

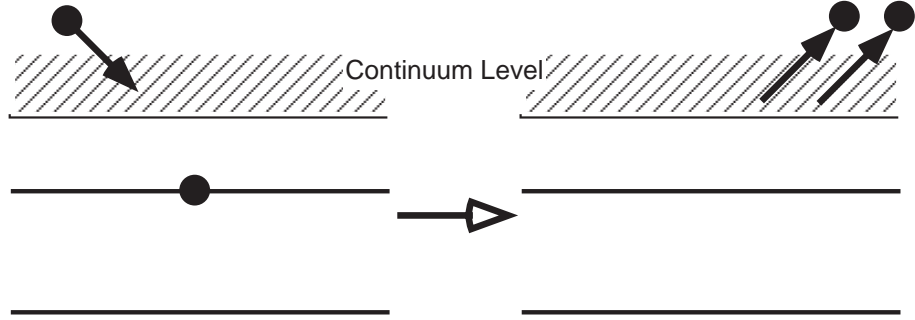
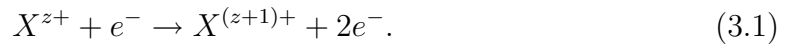


Figure 3.2: Schematic of Electron impact ionization process

Thermal Equilibrium (LTE) which means that the rate of a collisional process equals exactly the rate of its inverse is important for measurement of electron temperature in Ch. 4. At last, charge transfer collision process is briefly explained. This process might be significant in the formation of shock structure, since ion temperature is larger than electron temperature in ion-electron relaxation layer of shock wave (in more detail, see Sec. 3.4.4). In the following section, the rate coefficients formulae of each atomic process are shown.

### 3.1.1 Collisional Ionization

Collisional ionization process, here which is also called “electron impact ionization”, means that a free electron collides against an ion with knocking out a bound electron into the continuum as shown schematically in Fig. 3.2 and Eq. (3.1).



The collisional ionization rate coefficient is given by empirical formulae [73–76]. The general empirical formulae is following:

$$I^c(z, i) = C_{\xi_{z,i}} T_e^{-3/2} \times \frac{\exp(-E_{z,i}/T_e)}{(E_{z,i}/T_e)^k} F\left(\frac{E_{z,i}}{T_e}\right) \quad (\text{cm}^3/\text{s}), \quad (3.2)$$

where  $C$  and  $k$  are constant number and  $F(E_{z,i}/T_e)$  is expression function.  $E_{z,i}$  is ionization energy in eV and  $\xi_{z,i}$  is the number of equivalent bound electrons.  $z$  means the charge state and  $i$  shows the  $i$ th level of bound electron.

Table 3.1 shows empirical formulae of collisional ionization rate coefficients [73–76].

Table 3.1: Empirical formulae of collisional ionization rate coefficients

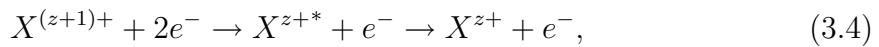
Author	$C \text{ cm}^3 \cdot \text{eV}^{3/2}/\text{s}$	$k$	$F(E_{z,i}/T_e)$
Landshoff-Perez	$1.24 \times 10^{-6}$	2	$0.915(1 + 0.064T_e/E_{z,i})^{-2} + 0.42(1 + 0.5T_e/E_{z,i})^{-2}$
Lotz	$3 \times 10^{-6}$	1	$E_1(E_{z,i}/T_e) \exp(E_{z,i}/T_e)$
Seaton	$2.15 \times 10^{-6}$	2	1
McWhirter	$0.234 \times 10^{-6}$	7/4	1

Salzmann [77] recommended the coefficient given by Landshoff and Perez [76]. In this study, the rate coefficient formulated by Landshoff and Perez [76] is used as shown in the following equation as,

$$I^c(z, i) = 1.24 \times 10^{-6} \xi_{z,i} T_e^{-3/2} \frac{\exp(-E_{z,i}/T_e)}{(E_{z,i}/T_e)^2} \times \left[ \frac{0.915}{(1 + 0.064T_e/E_{z,i})^2} + \frac{0.42}{(1 + 0.5T_e/E_{z,i})^2} \right] \quad (\text{cm}^3/\text{s}). \quad (3.3)$$

### 3.1.2 Three Body Recombination

In three body recombination, two free electrons enter at the same time into an interaction volume of an ion. In the process, one of the electrons is captured into an ionic state, while the second carries away the extra energy as shown in Fig. 3.3 and Eq. (3.4).



The rate coefficient of three body recombination is obtained by the detailed balance principle because this is the inverse process of electron collisional ionization.

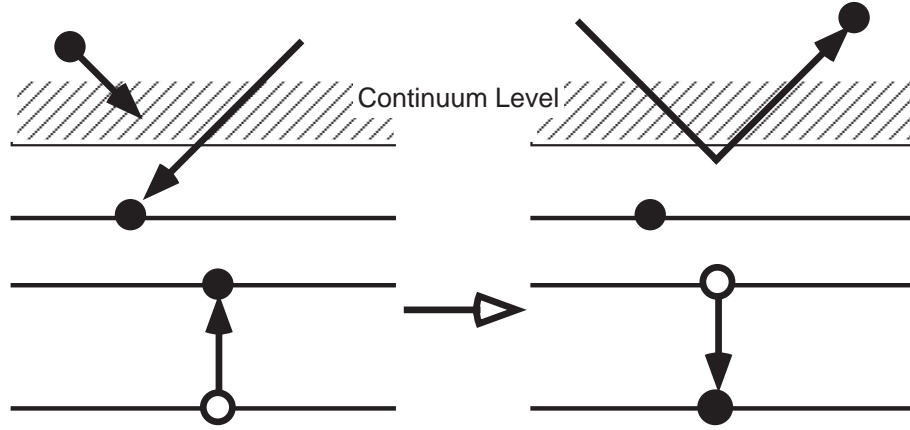


Figure 3.3: Schematic of three body recombination process

The coefficient used in this study is shown as follows,

$$R^{3b}(z, i) = 1.66 \times 10^{-22} T_e^{-3/2} N_e \frac{g_{z,i}}{g_{z+1,1}} \exp(E_{z,i}/T_e) I^c(z, i) \quad (\text{cm}^3/\text{s}), \quad (3.5)$$

where  $N_e$  is electron number density in  $\text{cm}^{-3}$ , and  $g_{z,i}$  and  $g_{z+1,1}$  are the degeneracy of a state after/before recombination.

### 3.1.3 Radiative Recombination

In radiative recombination, an electron is captured into one of the ionic states, with the emission of a photon which takes the extra energy as shown in Fig. 3.4 and Eq. (3.6). This is the inverse process of photoionization.



The rate coefficient for radiative recombination [79] used in this study, is shown in

$$R^r(z, i) = 5.20 \times 10^{-14} q_{z,i} \left( \frac{E_{z,i}}{T_e} \right)^{3/2} \times \exp(E_{z,i}/T_e) E_1(E_{z,i}/T_e) \quad (\text{cm}^3/\text{s}), \quad (3.7)$$

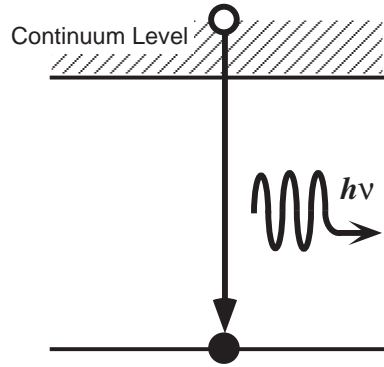


Figure 3.4: Schematic of radiative recombination process

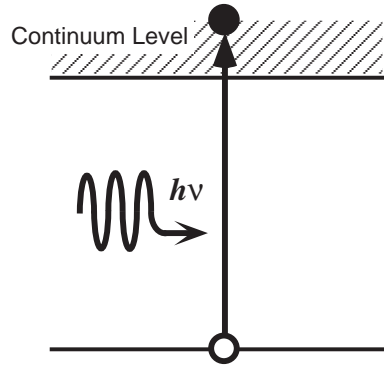


Figure 3.5: Schematic of photoionization process

where  $q_{z,i}$  is effective charge and  $E_1$  is exponential integral. The exponential integral  $E_1$  [80] is obtained by the following integration:

$$E_1(x) = \int_x^\infty \frac{\exp(-t)}{t} dt. \quad (3.8)$$

### 3.1.4 Photoionization

When the plasma density is high, that is optically thick, photon emitted by radiative process is reabsorbed by ion. In this process, the bound electron of the ion is sometimes ionized by the photon energy as shown in Fig. 3.5 and Eq. (3.9). This is called “photoionization”.



The cross section for photoionization  $\sigma_{\text{bf}}$  of hydrogen atom is estimated by the following equation [10, 81, 82]:

$$\sigma_{\text{bf}} = \frac{64\pi^4 e^{10} m_e q_{z,i}^4}{3\sqrt{3} h^6 c n^5 \nu^3} \quad (\text{cm}^2), \quad (3.10)$$

where  $e$  is elementary electric charge,  $4.8 \times 10^{-10}$  esu,  $m_e$  is the electron mass in cgs,  $h$  is the Planck constant,  $6.626 \times 10^{-27}$  erg s,  $c$  is the speed of light,  $2.998 \times 10^{10}$  cm/s,  $n$  is principal quantum number and  $\nu$  is photon frequency in Hz. The photoionization rate coefficient is estimated by,

$$I^p(z, i) = 4\pi \int_{h\nu \geq E_{z,i}} \sigma_{\text{bf}} \frac{I_\nu}{h\nu} d\nu \quad (\text{s}^{-1}), \quad (3.11)$$

where  $I_\nu$  is radiation intensity. On one occasion,  $I_\nu$  is replaced by Planck distribution  $B_\nu$  with radiation temperature  $T_r$  in K.  $B_\nu$  is shown as,

$$B_\nu = \frac{2h\nu^3}{c^2} \frac{1}{\exp(h\nu/k_B T_r) - 1} \quad (\text{erg/cm}^2/\text{str/s/Hz}), \quad (3.12)$$

where  $k_B$  is the Boltzmann constant,  $1.38 \times 10^{-16}$  erg/K.

However, photoionization is not considered as elementary process in this study. Instead, the radiation effect is estimated by using radiative heat flux  $F_{\text{rad}}$  as a free parameter of the calculation (in more detail, see Sec. 3.4.6).

### 3.1.5 Electron Collisional Excitation and Deexcitation

In the electron collisional excitation, which is also called “electron impact excitation”, a free electron that moves near an ion loses energy by inducing a transition of a bound electron from a lower into a higher level as shown in Fig. 3.6 and Eq. (3.13).



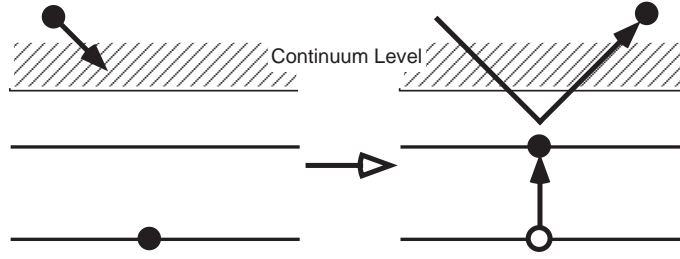


Figure 3.6: Schematic of electron impact excitation process

where \* means that ion is in an excited state. The rate coefficient for electron impact excitation  $C_e$  is following [83]:

$$C_e(i \rightarrow j) = 1.58 \times 10^{-5} f_{ij} T_e^{-\frac{1}{2}} E_{ij}^{-1} \exp(-E_{ij}/T_e) G \quad (\text{cm}^3/\text{s}), \quad (3.14)$$

where  $f_{ij}$ , which means a dimensionless quantity to express the strength of the transition, is absorption oscillator strength from  $i$  level to  $j$  level and,  $E_{ij}$  is excitation energy in eV,  $T_e$  is electron temperature in eV.  $G$ , which takes into account the quantum mechanical effect on the oscillator strength, is Gaunt factor and is shown in [83],

$$G = (0.15 + 0.28 \exp(-E_{ij}/T_e) E_1(E_{ij}/T_e)), \quad (3.15)$$

where  $E_1$  is exponential integral as shown in Eq. (3.8).

Whereas, electron collisional deexcitation, which is also called “electron impact deexcitation”, is the inverse of electron impact excitation. An electron moving near an excited ion induces a downward ionic transition from an upper to a lower ionic state in this process as shown in Fig. 3.7 and Eq. (3.16). The electron takes the extra energy.



where \* means that ion is excited. The rate coefficient for electron impact deexcitation  $D_{e(i)}$  is obtained by the detailed balance principle in,

$$D_{e(i)}(j \rightarrow i) = (g_i/g_j) \exp(E_{ij}/T_e) C_{e(i)}(i \rightarrow j) \quad (\text{cm}^3/\text{s}), \quad (3.17)$$

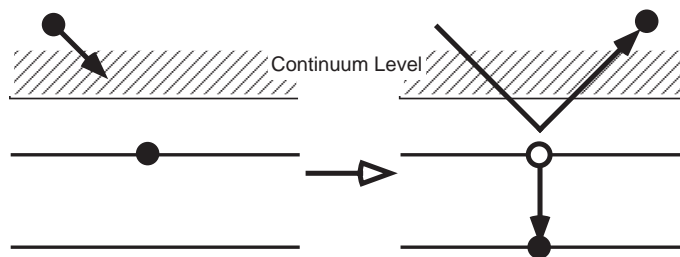


Figure 3.7: Schematic of electron impact deexcitation process

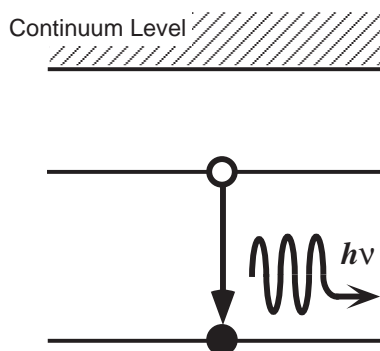


Figure 3.8: Schematic of radiative decay process

where  $g_i$  and  $g_j$  are statistical weight in  $i$  level and  $j$  level, respectively.

### 3.1.6 Radiative Decay

In radiative decay, which is also called “spontaneous emission”, a photon is emitted spontaneously, thereby inducing a transition of the ion from the higher to the lower state. This process is the inverse of Resonant photoabsorption as shown in Fig. 3.8 and Eq. (3.18).

$$X^{z+*} \rightarrow X^{z+} + h\nu, \quad (3.18)$$

where \* means that ion is excited. The rate of radiative decay  $A_r$ , which is called “Einstein A coefficient”, is shown,

$$A_r(j \rightarrow i) = 4.34 \times 10^7 \times \frac{g_i}{g_j} f_{ij} E_{ij}^2 \quad (1/s). \quad (3.19)$$

### 3.1.7 Atom-atom Collisional Ionization

Ionization process in collisions between neutral atoms is expected to be important for forming initial “priming” electrons, which is a trigger for electron avalanche in shock structure as show in Sec. 2.1.4. Atom-atom collisional ionization process is shown in,



however, here it assumes only the same atom collision. Strictly speaking, this process is considered to the two-step, atom-atom excitation and ionization. The cross sections are actually not truly ionization cross sections but rather those of rate-controlling excitation reaction [59].

Drawin estimated ionization cross section for the collisions between neutral atoms as show in [54],

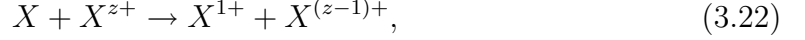
$$\sigma_{a-a} = 4\pi a_0^2 \left( \frac{E_H}{E_i} \right)^2 \frac{m_A}{m_H} \xi_i \frac{2m_e}{m_e + m_A} \frac{W_i - 1}{\left[ 1 + \frac{2m_e}{m_e + m_A} (W_i - 1) \right]^2} \quad (\text{cm}^2), \quad (3.21)$$

where,  $a_0 = 5.2 \times 10^{-9}$  cm,  $E_i$  is ionization energy of a target atom,  $E_H$  is ionization energy of hydrogen,  $\xi_i$  is number of equivalent electrons in the outer shell of an atom,  $m_e$  is electron mass,  $m_A$  is target atom mass,  $m_H$  is the hydrogen atomic mass,  $W_i = (E_a - E_i)/E_i$ , and  $E_a$  means the kinetic energy of the atoms in the center of mass system.

### 3.1.8 Charge Transfer Collision

When an ion approaches an atom, the ion attract the atomic electrons, and it may eventually capture one or more electrons from the atom after its collision with

that atom. The atomic process is called “charge transfer” as shown in,



however, here it assumes only the same atom collision and one electron capture process. The cross section  $\sigma_{\text{ex}}$  of charge transfer collision is qualitatively explained by “classical overbarrier model” [84] as shown in,

$$\sigma_{\text{ex}} \sim 6.5 \times 10^{-14} \left( \frac{2\sqrt{z} + 1}{E_i} \right)^2 \quad (\text{cm}^2), \quad (3.23)$$

where  $z$  is the charge of the projectile ion and  $E_i$  is the ionization potential of the target atom electron in eV. Charge transfer process might be important for evaluation of the charge state profiles in shock waves (See Sec. 3.4.4).

## 3.2 Rate Equation

The population  $N(z, i)$  of each ion is decided by the atomic event “rate” in Fig. 3.1. As usual,  $z$  means the charge state and  $i$  means  $i$ th level of bound electron. The atomic event “rate” is described by the following rate Equation:

$$\begin{aligned} \frac{dN(z, i)}{dt} = & \sum_{j(<i)} E(z, j \rightarrow z, i)N(z, j) + \sum_{j(>i)} DE(z, j \rightarrow z, i)N(z, j) \\ & - \sum_{j(>i)} E(z, i \rightarrow z, j)N(z, i) - \sum_{j(<i)} DE(z, i \rightarrow z, j)N(z, i) \\ & + \sum_j I(z-1, j \rightarrow z, i)N(z-1, j) + \sum_j R(z+1, j \rightarrow z, i)N(z+1, j) \\ & - \sum_j I(z, i \rightarrow z+1, j)N(z, i) \\ & - \sum_j R(z, i \rightarrow z-1, j)N(z, i), \end{aligned} \quad (3.24)$$

where  $E(z, i \rightarrow z, i')$  and  $DE(z, i' \rightarrow z, i)$  are excitation and deexcitation rate coefficients, and  $I(z', i' \rightarrow z, i)$  and  $R(z, i \rightarrow z', i')$  are ionization and recombination rate coefficients, respectively. This is time dependent rate equation called “Collisional Radiative model”, and this model can be appropriate to wide range of plasma parameter.

In this study, as we consider only ionization and recombination processes without photoionization, Eq. (3.24) is simplified as the following:

$$\begin{aligned} \frac{dN_i(z)}{dt} = & (I^c(z-1)N_e) N_i(z-1) \\ & - (I^c(z)N_e + R^{3b}(z)N_e + R^r(z)N_e) N_i(z) \\ & + (R^{3b}(z+1)N_e + R^r(z+1)N_e) N_i(z+1), \end{aligned} \quad (3.25)$$

where  $N_i(z)$  and  $N_e$  are ion density of charge state  $z$  and total electron density,  $I^c(z)$  is collisional ionization rate coefficient,  $R^{3b}(z)$  is three body recombination rate coefficient,  $R^r(z)$  is radiative recombination rate coefficient.

### 3.3 Steady and 1-D hydrodynamic Conservation Laws and Ion-electron Relaxation Equation

Our electro-magnetically driven shock waves are considered to be steady and planar condition as show in Sec. 2.5.1. Based on Eqs. (2.4), (2.5), and (2.6), Mass, momentum and energy conservation laws under the steady and planar condition [85,86] and ideal equation of state are:

$$\rho u = \text{const}, \quad (3.26)$$

$$p + \rho u^2 = \text{const}, \quad (3.27)$$

$$\begin{aligned} \rho u \left[ \frac{1}{2}u^2 + \frac{5}{2}R(T_i + \alpha T_e) + \frac{1}{N_i} \sum_{j=1}^{20} N_{Xe^{j+}} RT^{j+} \right] \\ + F_{\text{rad}} + u(p_{\text{rad}} + \epsilon_{\text{rad}}) + F_{\text{cond}} = E(z), \end{aligned} \quad (3.28)$$

$$p = \rho R(T_i + \alpha T_e) + p_{\text{rad}}, \quad (3.29)$$

where  $\rho$  is plasma mass density,  $p$  is total pressure,  $u$  is flow velocity,  $\alpha$  is the degree of ionization,  $R$  is gas constant:  $R = k_B/m_{Xe}$ ,  $m_{Xe}$  is Xenon atomic mass,  $N_{Xe^{j+}}$  is number density of charge state  $j+$ ,  $T^{j+}$  is equal to ionization energy divided by the Boltzmann constant  $k_B$ ,  $F_{\text{rad}}$  is radiation flux,  $p_{\text{rad}}$  is radiation pressure,  $\epsilon_{\text{rad}}$  is radiation energy density,  $E(z)$  is total energy flux in a position  $z$  and  $F_{\text{cond}}$  is the heat

conduction flux by ion and electron conductivity. In this paper,  $F_{\text{cond}}$  is not considered but may be estimated using the procedure proposed by Brysk et al [87]. We assume that maximum charge state is 20, since ion populations in higher charge states are not effective for the formation of shock structure in this plasma parameter. Radiative flux  $F_{\text{rad}}$  is a fitting parameter to estimate the radiative effect from comparison of experimental results with the calculation. However the radiation pressure and the radiation energy density are neglected [10, 22] because the optical thickness of the shocked region in our experimental condition is not enough thick.

In shock wave structure, the shock heated ions relax to ion-electron equilibrium by energy transfer to cooler electrons. The energy relaxation frequency  $\nu_{\text{eq}}(\text{i}, \text{e})$ , which is inverse of  $t_{\text{eq}}(\text{i}, \text{e})$  as shown in Eq. (2.28) is given by Spitzer [27, 48], as the following:

$$\begin{aligned} \nu_{\text{eq}}(\text{i}, \text{e}) &= \frac{1}{t_{\text{eq}}(\text{i}, \text{e})}, \\ &= \frac{8(2\pi)^{1/2} m_e^{1/2} N_e Z_i^2 e^4 \ln\Lambda}{3m_i (4\pi\epsilon_0)^2 (k_B T_e)^{3/2}}, \\ &\sim 3.2 \times 10^{-9} \frac{N_i Z_i^3 \ln\Lambda}{A T_e^{1.5}} \quad (1/\text{s}). \end{aligned} \quad (3.30)$$

In Eq. (3.30),  $N_i$  is ion number density in  $\text{cm}^{-3}$ ,  $T_e$  is electron temperature in eV,  $A$  is the atomic weight of the material ( $\text{Xe} = 131$ ), and  $Z_i$  is the average ionization state. Here, the debye shielding distance  $\lambda_D$  in SI assumed no shielding by ions is

$$\lambda_D = \left( \frac{\epsilon_0 k_B T_e}{N_e e^2} \right)^{1/2} \quad (\text{m}), \quad (3.31)$$

where the characters denote the same meanings as usual and unit in SI. From Eqs. (2.24) and (2.20), the Coulomb logarithm  $\ln\Lambda$  in SI is

$$\ln\Lambda \sim \ln \left( \frac{3(4\pi\epsilon_0)\epsilon_0^{1/2} (k_B T_e)^{3/2}}{N_e^{1/2} Z_i e^3} \right). \quad (3.32)$$

Therefore, the ion-electron relaxation equation is obtained [48] as follows

$$\frac{dT_i}{dt} = - \frac{T_i - T_e}{t_{\text{eq}}(\text{i}, \text{e})}. \quad (3.33)$$

## 3.4 Calculation Results

In this section, we show calculation results which show relations between the charge state profiles,  $T_i$ ,  $T_e$  and effects of three parameters: initial pressure, initial electron temperature and radiative flux. Especially, it is emphasized that we propose to make a comparative study between numerical calculation and experimental observation using two fitting parameters: those are initial electron temperature  $T_e^0$  and radiative flux  $F_{\text{rad}}$ .

### 3.4.1 Calculation Flow and Calculation Region in Shock Waves

We estimate the structure of strong shock wave with relaxation layer under steady and planar condition [88]. The numerical modeling is based on the steady and planar condition. Distributions of the ion and electron temperatures, the ion and electron number densities, the flow velocity, and the Xe charge states were calculated by the rate equations shown in Eq. (3.25) coupled with mass, momentum, and energy conservation laws and ideal equation of state. They are shown in Eqs. (3.26), (3.27), (3.28), and (3.29). The relaxation between ion and electron can be expressed as Eq. (3.33). Some Xe data of related atomic process were published [89–96]. The atomic data for this calculation were derived from Saloman [89]. Here, the calculation flowchart is shown in Fig. 3.9.

In case of steady state condition, here, time differential  $dt$  in Eq. (3.25) and (3.33) can be converted to  $dz/u$ . Then we can convert the temporal evolution of physical parameters into spatial scales based on the coordinate from the shock front. This is significantly advantageous point to investigate the shock wave structure .

Next, we show a sketch of an expected temperature distribution in the shock region, initial condition and the calculation region of shock wave in Fig. 3.10. Here, we don't calculate precursor structure of the shock wave. Instead, we calculate just the region behind shock front as indicated in Fig. 3.10.

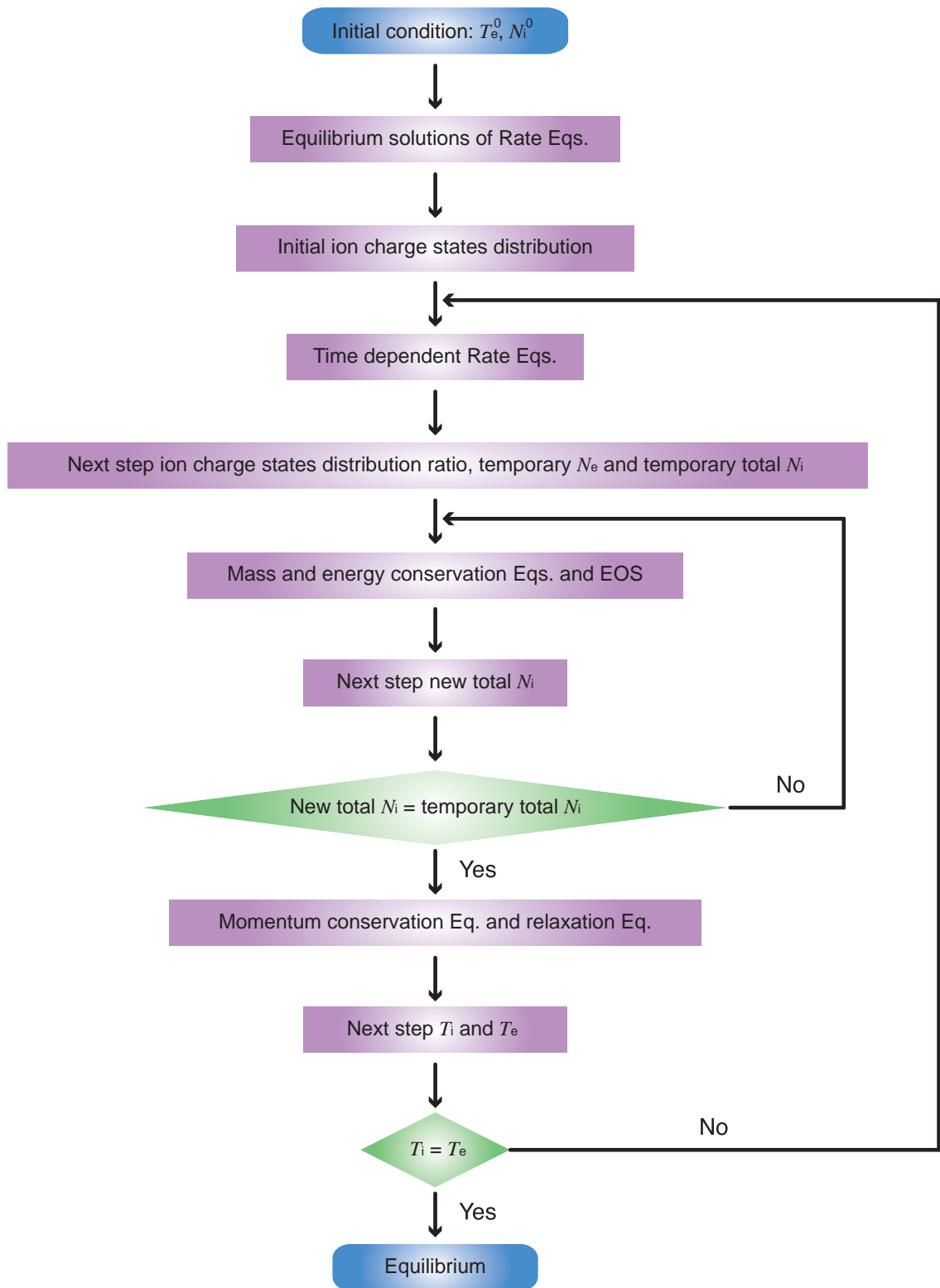


Figure 3.9: Flowchart for numerical simulation of shock heated relaxation layer

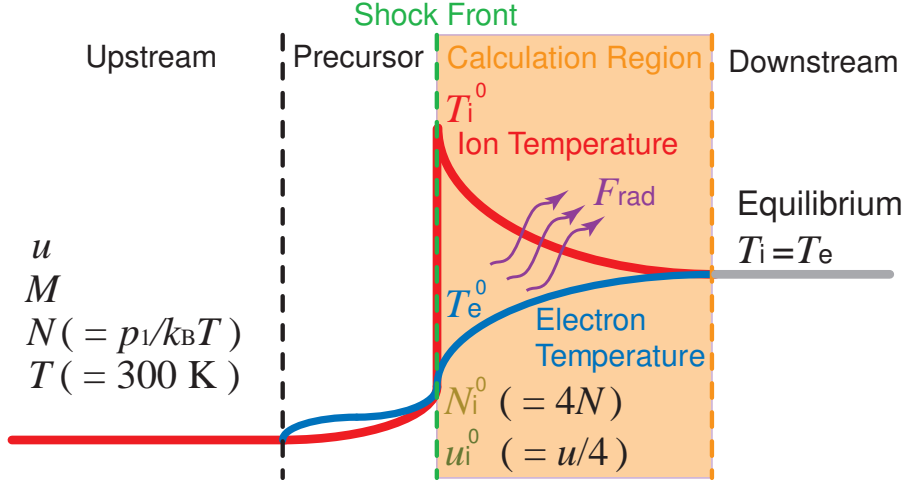


Figure 3.10: Temperature distribution sketch, initial condition and calculation region

### 3.4.2 Two Initial Free Parameters

In order to proceed the calculation, we have to specify the initial condition. Initial parameters for the calculation of relaxation layer are ion temperature  $T_i^0$ , electron temperature  $T_e^0$ , flow velocity behind the shock wave  $u_i^0$ , total ion number density  $N_i^0$  and the distribution of the initial charge state. Among the parameters, initial electron temperature  $T_e^0$  and radiative flux  $F_{\text{rad}}$  are arbitrarily specified as fitting parameters, which are important to investigate precursor and radiative cooling region.

At just behind the shock front, we may assume that the specific heat ratio  $\gamma$  to be 5/3, without considering the contribution from internal degrees of freedom. The initial ion temperature  $T_i^0$  is derived from the Rankine-Hugoniot relation, Eq. (2.17) and total ion number density  $N_i^0$  is 4 times that of upstream density from Eq. (2.16). For the same reason, initial flow velocity  $u_i^0$  is as 1/4 times as shock front velocity. The distribution of the initial charge states at shock front is given by the rate equation with equilibrium condition, which means left-hand side, time derivation term, of Eq. (3.25) equals to 0, for an initial electron temperature  $T_e^0$  and an initial total ion number density  $N_i^0$ .

At last, the two fitting free parameters, initial electron temperature and radiative flux, are explained. The former  $T_e^0$  is connected to precursor region. As shown in Sec.

2.1.5, the preheat region of shock wave is formed by electron heat conductivity and photoionization process because a part of hot electron is faster than shock velocity, and of course radiation also. Precursor structure is important for estimating a structure of strong shock wave. Whereas, the latter  $F_{\text{rad}}$  reflects radiation effect behind the shock front. As well as precursor region, radiative cooling region is also significant for shock heated region. When the numerical results based on these parameters and appropriate rate coefficients are fitted with experimental data, we can estimate the structure of strong shock wave.

### 3.4.3 Initial Gas Pressure and Relaxation Structure

As has been shown in Fig. 2.12, we obtained the relation between initial pressure and shock front velocity. Here, three pressure cases are selected as typical cases which are shown in Table 3.2. Table 3.2 shows shock parameters: initial pressure  $p_1$  in vacuum chamber, initial total ion number density  $N_i^0$ , shock Mach number  $M$ , and initial ion temperature  $T_i^0$ . They can be obtained from the experimentally observed shock front speed  $u_s$ . Here, initial electron temperature  $T_e^0$  is assumed to be 2.5 eV to see the relaxation structure as a function of  $p_1$ . Xe II is dominant charge state around  $T_e \sim 2.5$  eV, and it is easy to observe in the experiment.

Table 3.2: Shock parameters estimated from experimental results and Rankine-Hugoniot Relations

$p_1$ Torr	$N_i^0$ 1/cm <sup>3</sup>	$u_s$ km/s	$M$	$T_i^0$ eV
0.12	$1.7 \times 10^{16}$	30	170	230
0.75	$1.1 \times 10^{17}$	11	61	30
3.0	$4.2 \times 10^{17}$	4.0	22	3.9

We show calculation results of Xe ion charge state distributions, and ion and electron temperature distributions for the case with  $p_1 = 0.12$  Torr in Figs. 3.11(a) and 3.11(b). In the calculation,  $z = 0$  indicates the location of shock front. Ion-electron relaxation length was estimated to be  $\sim 8$  mm, which can be also observed in the experiment with  $p_1 = 0.12$  Torr. The result also indicated that equilibrium

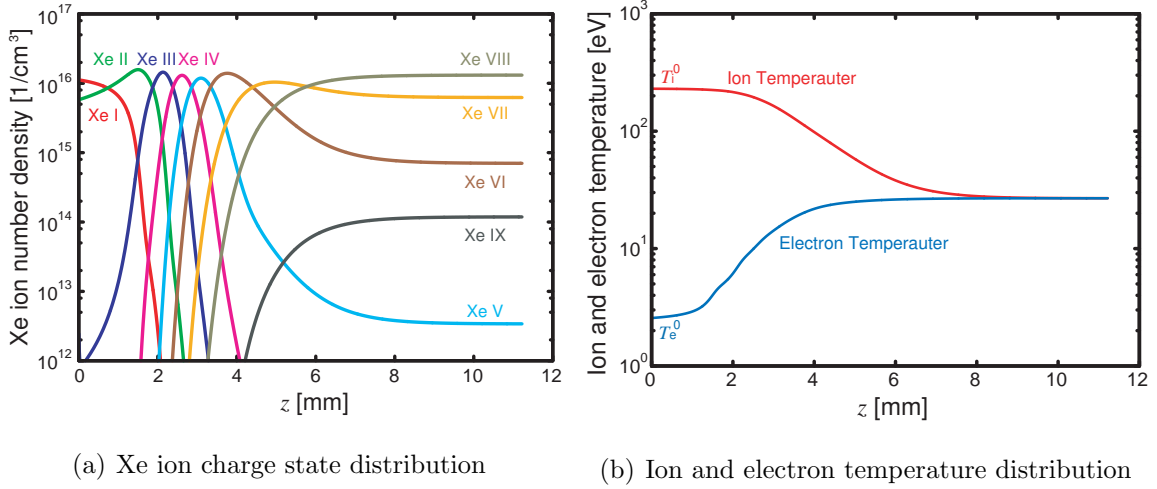


Figure 3.11: Relaxation layer of shock heated Xe for  $T_e^0 = 2.5$  eV at  $p_1 = 0.12$  Torr

temperature is  $\sim 30$  eV and the shock heated plasma is strongly ionized up to  $Z_i \sim 7$ .

With the higher  $p_1$ , for example,  $p_1 = 0.75$  Torr, scale lengths of the Xe ion charge state distributions, and ion and electron temperature distributions are decreased as shown in Figs. 3.12(a) and 3.12(b). Ion-electron relaxation length is  $\sim 1.5$  mm. In this condition, the equilibrium temperature is  $\sim 7$  eV and this plasma is ionized to  $Z_i > 3$ .

At the initial pressure of 3.0 Torr, Xe ion charge state distributions, and ion and electron temperature distributions are shown in Figs. 3.13(a) and 3.13(b). Ion-electron relaxation length is estimated to be  $\sim 2$  mm, which can be observed in the experiment in this condition. The relaxation length in this condition is rather longer than that in the case of lower initial pressure shown in Figs. 3.12(a) and 3.12(b), in spite of higher plasma density. The reason is considered that ion-electron relaxation is inversely proportional to the average ionization degree  $Z_i$  as shown in Eq. (2.28). Since the average ion charge state  $Z_i$  is  $\sim 0.5 < 1$  in the condition shown in Fig. 3.13(a), the plasma is in a weakly ionized state. The distributions of ion charge state and temperature are not changed enough because  $T_i^0$  is close to  $T_e^0$  in this condition.

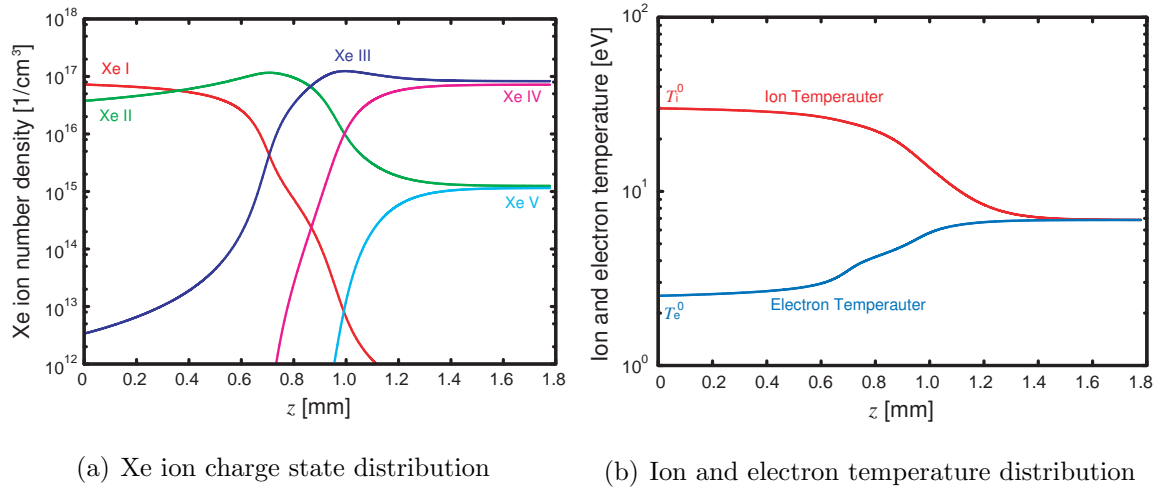


Figure 3.12: Relaxation layer of shock heated Xe for  $T_e^0 = 2.5$  eV at  $p_1 = 0.75$  Torr

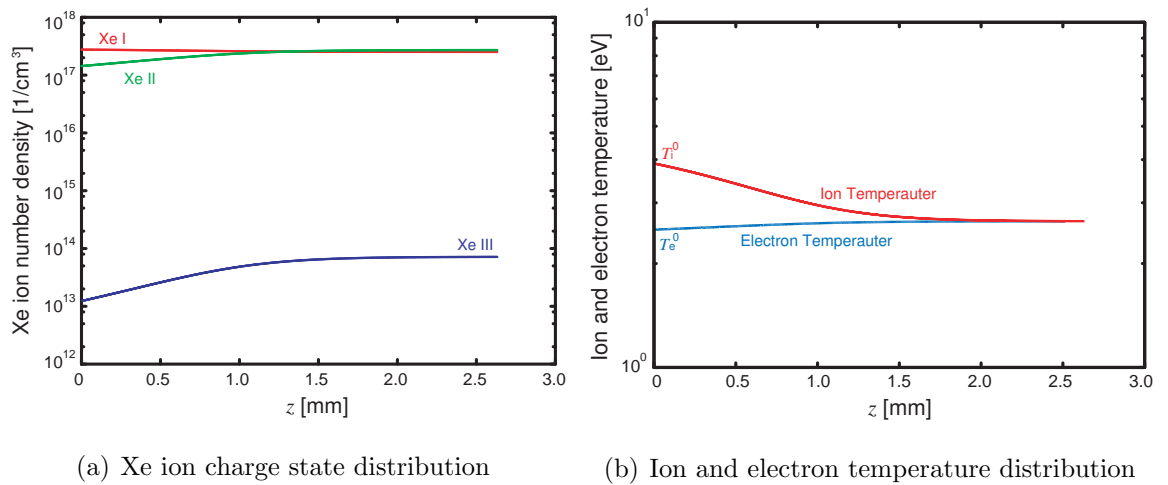


Figure 3.13: Relaxation layer of shock heated Xe for  $T_e^0 = 2.5$  eV at  $p_1 = 3.0$  Torr

We calculated the ion charge state and temperature distributions based on the initial ion temperature estimated from experimental shock front velocity and initial pressure. In the our shock velocity region, it was confirmed that the shock wave structure changes fairly depending on the initial pressure. This means that our device has potential to estimate the relaxation layer with comparative study of experimental results and numerical calculations.

### 3.4.4 Initial Electron Temperature and Relaxation Length

We discuss the effect of initial electron temperature  $T_e^0$ : one of the two fitting free parameters. We estimate the relaxation process for three initial pressure cases, 0.12, 0.75 and 3.0 Torr. Initial electron temperatures  $T_e^0$  are 2.2 and 2.8 eV for each initial pressure condition.

The charge state and temperature distributions for  $T_e^0 = 2.2$  and 2.8 eV at  $p_1 = 0.12$  Torr, are shown in Figs. 3.14(a), 3.14(b), 3.15(a), and 3.15(b). As shown in Figs. 3.14(a) and 3.14(b) for low initial electron temperature,  $T_e^0 = 2.2$  eV, the scale length of Xe II,  $\sim 13$  mm, is larger than  $\sim 3$  mm in  $T_e^0 = 2.5$  eV. As shown, the slight difference of initial electron temperature significantly changes the Xe II region, and naturally ion-electron relaxation length. On the other hand, as shown in Figs. 3.15(a) and 3.15(b) for higher initial electron temperature,  $T_e^0 = 2.8$  eV, the relaxation structure is similar to that for  $T_e^0 = 2.5$  eV. The relaxation length is smaller slightly in case of  $T_e^0 = 2.8$  eV because initial average ionization degree is higher and the ion-electron relaxation time  $t_{\text{eq}}(i, e)$  becomes smaller.

The charge state and temperature evolutions for  $p_1 = 0.75$  Torr, are shown in Figs. 3.16(a), 3.16(b), 3.17(a), and 3.17(b). The dependency of initial electron temperature is similar to that in low initial pressure, case of  $p_1 = 0.12$  Torr. For the case of  $T_e^0 = 2.2$  eV, the existence region of Xe II,  $\sim 6$  mm, is extremely longer than the case with  $T_e^0 = 2.8$  eV.

And then, the charge state and temperature distributions for  $p_1 = 3.0$  Torr, are shown in Figs. 3.18(a), 3.18(b), 3.19(a), and 3.19(b). The dependency of initial electron temperature is similar to those of lower  $p_1$  cases. However, as referred in Sec.

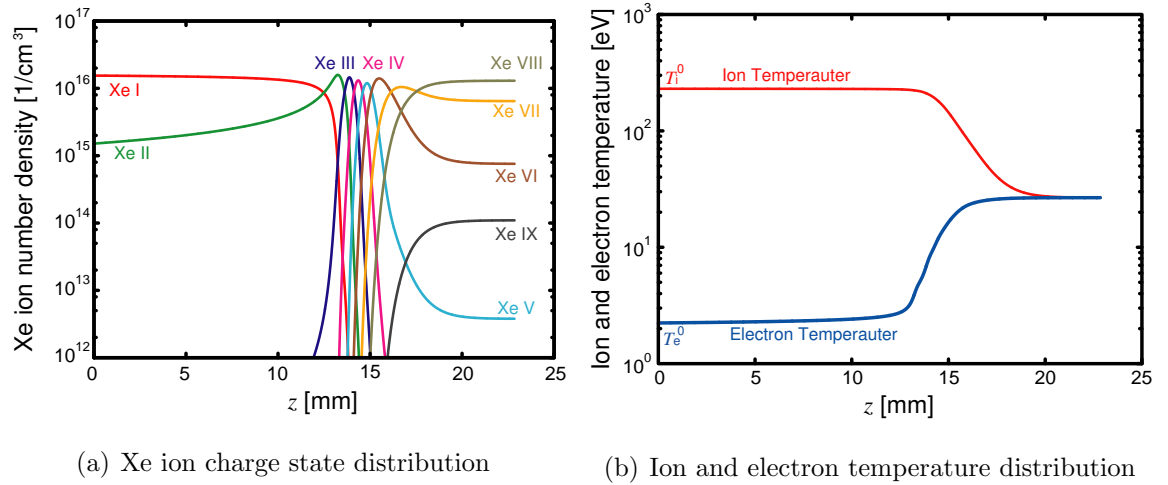


Figure 3.14: Relaxation layer of shock heated Xe for  $T_e^0 = 2.2$  eV at  $p_1 = 0.12$  Torr

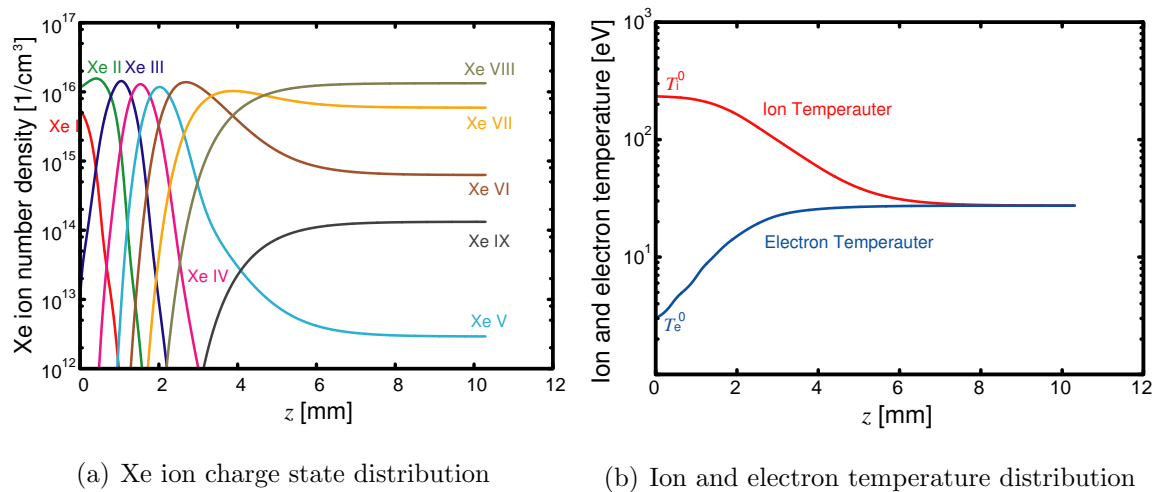
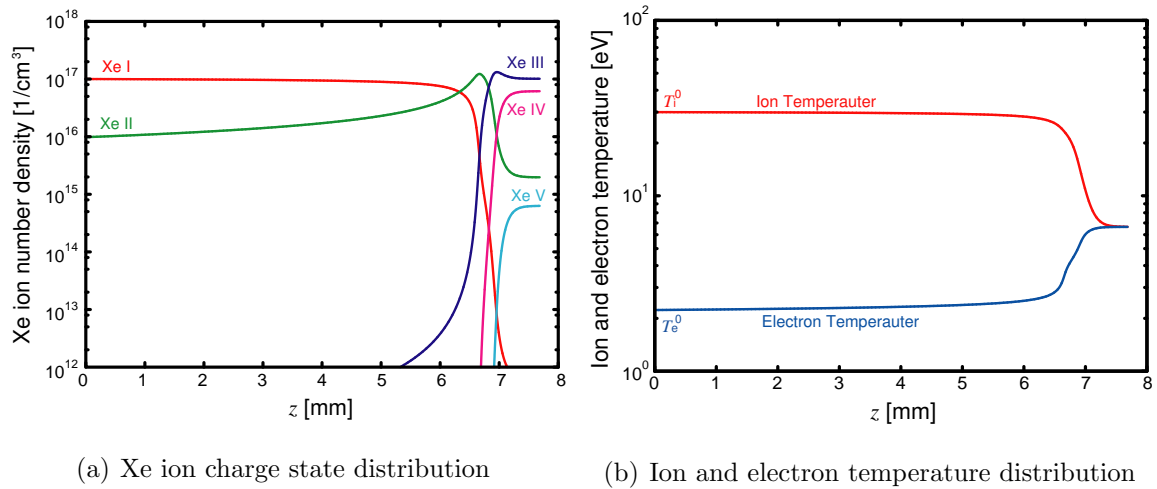
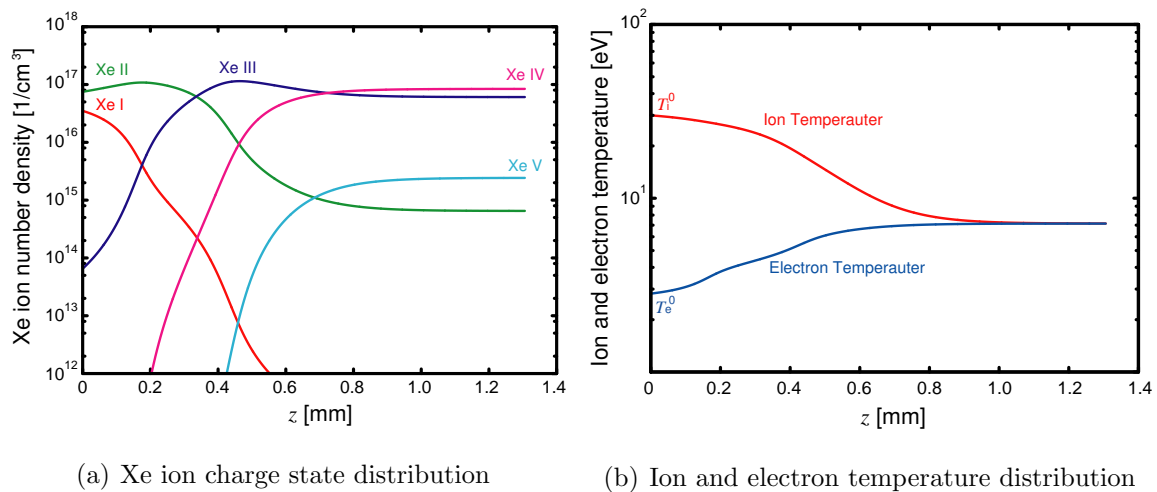


Figure 3.15: Relaxation layer of shock heated Xe for  $T_e^0 = 2.8$  eV at  $p_1 = 0.12$  Torr

Figure 3.16: Relaxation layer of shock heated Xe for  $T_e^0 = 2.2$  eV at  $p_1 = 0.75$  TorrFigure 3.17: Relaxation layer of shock heated Xe for  $T_e^0 = 2.8$  eV at  $p_1 = 0.75$  Torr

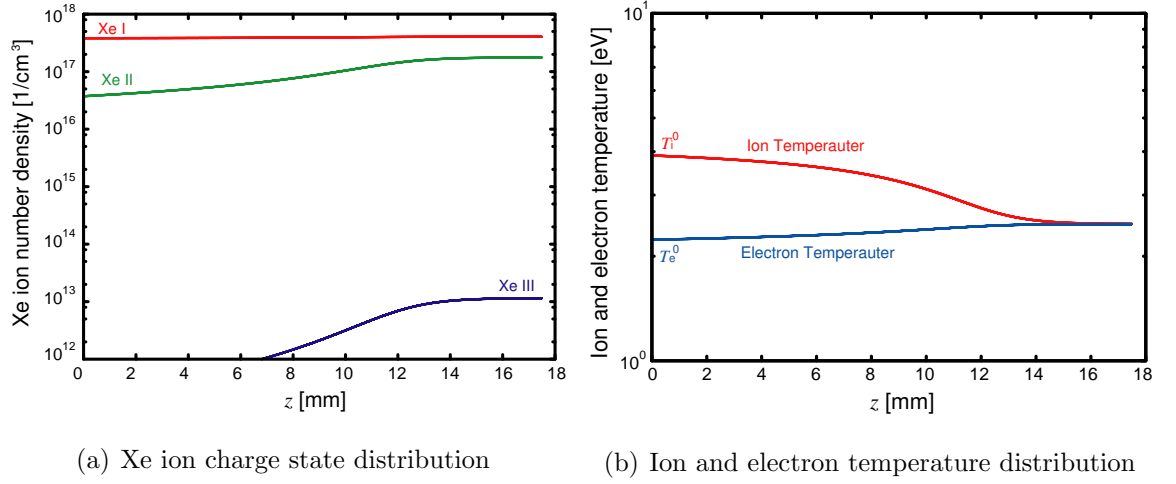


Figure 3.18: Relaxation layer of shock heated Xe for  $T_e^0 = 2.2$  eV at  $p_1 = 3.0$  Torr

3.4.3, the distributions of ion charge state and of temperature do not change so much enough because  $T_i^0$  is close to  $T_e^0$  in this condition. When a lower initial electron temperature, which is considered to be reasonable, was set, the relaxation length became extremely longer. Essentially, in the very low initial electron temperature, Xe I occupies dominant population of Xe charge states.

It is important for the scale length whether the number of “priming” electron for ionization is enough or not. As shown, the existence region of Xe II behind the shock wave is very sensitive to the initial electron temperature  $T_e^0$ . We estimate precursor temperature by fitting these calculations with experimental results because the emission lines from Xe II can be observed by visible spectroscopy.

### 3.4.5 Effects of Charge Transfer and Electron-neutral Collision

It is investigated whether the contribution of charge-transfer collisions is significant in evaluation of the charge state profiles. In the estimation, we evaluate only the processes related to Xe II because it is emphasized that the region of Xe II is sensitive to initial electron temperature in the previous section. Therefore, we focused on the

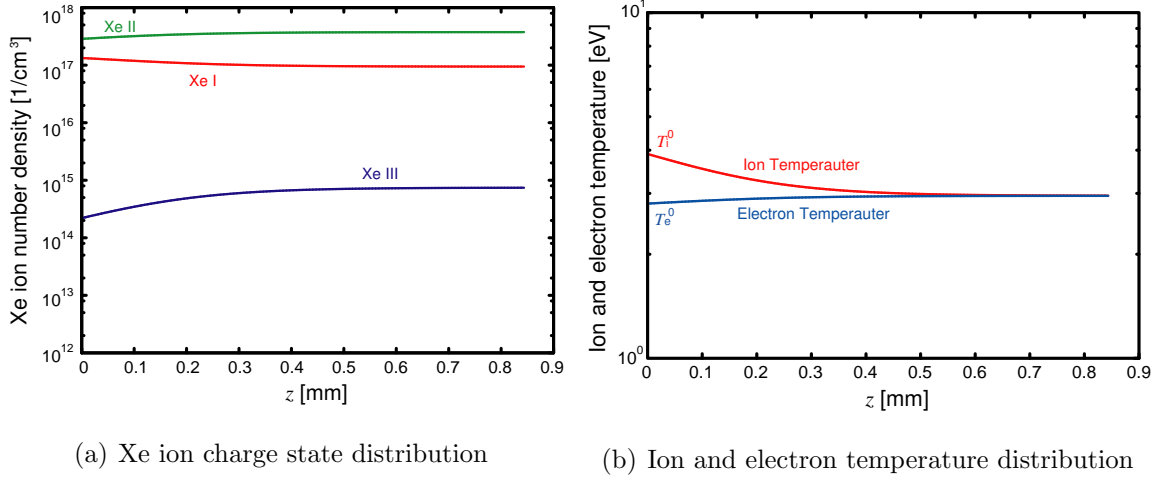
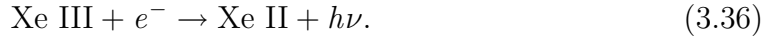
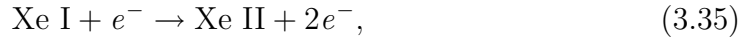


Figure 3.19: Relaxation layer of shock heated Xe for  $T_e^0 = 2.8$  eV at  $p_1 = 3.0$  Torr

charge-transfer, ionization and recombination processes. They are,



Here we can neglect the following process:  $\text{Xe I} + \text{Xe II} \rightarrow \text{Xe II} + \text{Xe I}$ , because ion charge state profile does not change, and the dominant recombination process of Xe II is radiative recombination in this condition. The condition of the estimation assumes the same one at  $z = 0$  of Fig. 3.14(a), namely we assume that the electron temperature is 2.2 eV and total ion number density is  $1.7 \times 10^{16} \text{ cm}^{-3}$ . In this condition, ion number density of  $N_{\text{Xe I}}$  and  $N_{\text{Xe III}}$ , electron number density  $N_e$  is given by the equilibrium rate equation, which means the left-hand side of Eq. (3.25) equals to 0. These parameters is shown in Table 3.3

Table 3.3: Plasma parameters for the estimation of charge-transfer collision

Total $N_i^0 \text{ cm}^{-3}$	$N_{\text{Xe I}} \text{ cm}^{-3}$	$N_{\text{Xe III}} \text{ cm}^{-3}$	$N_e \text{ cm}^{-3}$	$T_i^0 \text{ eV}$	$T_e^0 \text{ eV}$
$1.7 \times 10^{16}$	$1.5 \times 10^{16}$	$2.2 \times 10^{12}$	$1.5 \times 10^{15}$	230	2.2

First, we estimate the charge-transfer collision process of Eq. (3.34) using the

cross section by the classical overbarrier model shown in Eq. (3.23) [84]. The cross section is estimated to be:

$$\begin{aligned}\sigma_{\text{ex}} &\sim 6.5 \times 10^{-14} \left( \frac{2\sqrt{z} + 1}{E_i} \right)^2 \quad (\text{cm}^2), \\ &\sim 6.6 \times 10^{-15} \quad (\text{cm}^2),\end{aligned}\tag{3.37}$$

where  $E_i$  is the ionization potential energy of acceptor in eV, for Xe  $E_i \sim 12$  eV, and  $z$  is the charge number of donor,  $z = 2$ . Then the total rate of charge transfer reaction per unit time per unit volume,  $N_{(\text{ex})}$ , that is the products of the above cross section, number densities of Xe I and Xe III, and relative velocity which assumes thermal mean velocity at the condition,  $T_i \sim 230$  eV, is estimated be

$$N_{(\text{ex})} \sim 4.8 \times 10^{20} \quad (1/\text{cm}^3/\text{s}).\tag{3.38}$$

On the other hand, the reaction numbers,  $N_{(I^c)}$  and  $N_{(R^r)}$ , per unit time per unit volume for processes shown in Eqs. (3.35) and (3.36), are estimated using rate coefficient of collisional ionization,  $I^c(z = 0)$ , and radiative recombination,  $R^r(z = 2)$ , from the equilibrium rate equation as the following

$$N_{(R^r)} = N_{\text{Xe III}} R^r(z = 2) N_e,\tag{3.39}$$

$$\sim 3.2 \times 10^{23} \quad (1/\text{cm}^3/\text{s}) \quad \gg N_{(\text{ex})},\tag{3.40}$$

$$N_{(I^c)} = N_{\text{Xe I}} I^c(z = 0) N_e,\tag{3.41}$$

$$\sim 1.2 \times 10^{24} \quad (1/\text{cm}^3/\text{s}) \quad \gg N_{(\text{ex})}.\tag{3.42}$$

These estimations indicate that the reaction number of charge-transfer collision is much less than ones of collisional ionization and radiative recombination in the parameter region considered in the thesis. Therefore, in the parameter region discussed, we can neglect the number of charge-transfer collision process.

At last, the contribution of electron-neutral collision process is investigated. In the average low ion charge state region:  $Z_i < 1$ , the collision may be considered not only to electron-ion but also electron-neutral collision. Then, we show the electron-neutral relaxation time  $t_{\text{eq}}(\text{e}, \text{n})$  as shown in

$$t_{\text{eq}}(\text{e}, \text{n}) \sim \frac{1}{\sqrt{2} N_e \sigma_{(\text{e}, \text{n})} v_e} \frac{m_{\text{Xe}}}{m_e},\tag{3.43}$$

where  $\sigma_{(e,n)}$  is the cross section of electron-neutral scattering, which is order of a Xe atom cross section,  $\pi \times 10^{-16} \text{ cm}^2$ , and  $v_e$  is electron thermal velocity. We assume the same condition as well as to that of charge-transfer: the electron temperature is 2.2 eV and total ion number density is  $1.7 \times 10^{16} \text{ cm}^{-3}$ . The electron-neutral relaxation time  $t_{\text{eq}}(e, n)$  is estimated to be

$$t_{\text{eq}}(e, n) \sim 3 \times 10^{-4} \text{ (s)}. \quad (3.44)$$

This means  $t_{\text{eq}}(e, n)$  is extremely longer than the characteristic time. Therefore, the electron-neutral process can be neglected in this region. Zeldovich [10] reported that the electron-neutral collision process is only significant for  $Z_i < 10^{-3}$ .

### 3.4.6 Radiation Effect on Shock Wave Structure with Relaxation Layer

We discuss the effect of fitting parameter  $F_{\text{rad}}$ . When the radiation effect is significant in the shock wave structure, the radiation cools the shock heated region as discussed in Sec. 2.1.3.

Under the same condition in Fig. 3.11(a), the ion and electron temperature distributions are estimated as in Fig. 3.20 without radiation effect ( $F_{\text{rad}} = 0$ ).  $T_i$ ,  $T_e$ , and also equilibrated temperature decrease as schematically shown in Fig. 3.20 when we consider the effect of  $F_{\text{rad}}$ .

Our experimental set up has a potential to observe the profile of electron temperature by spectroscopy. The calculation can fit the experimental results with radiative flux  $F_{\text{rad}}$ , as a fitting parameter. We can evaluate radiative flux  $F_{\text{rad}}$ , with this calculation model when we estimate the electron temperature distribution from experimental results. In Sec. 5.3, we discuss the influence of radiative flux in our experiment.

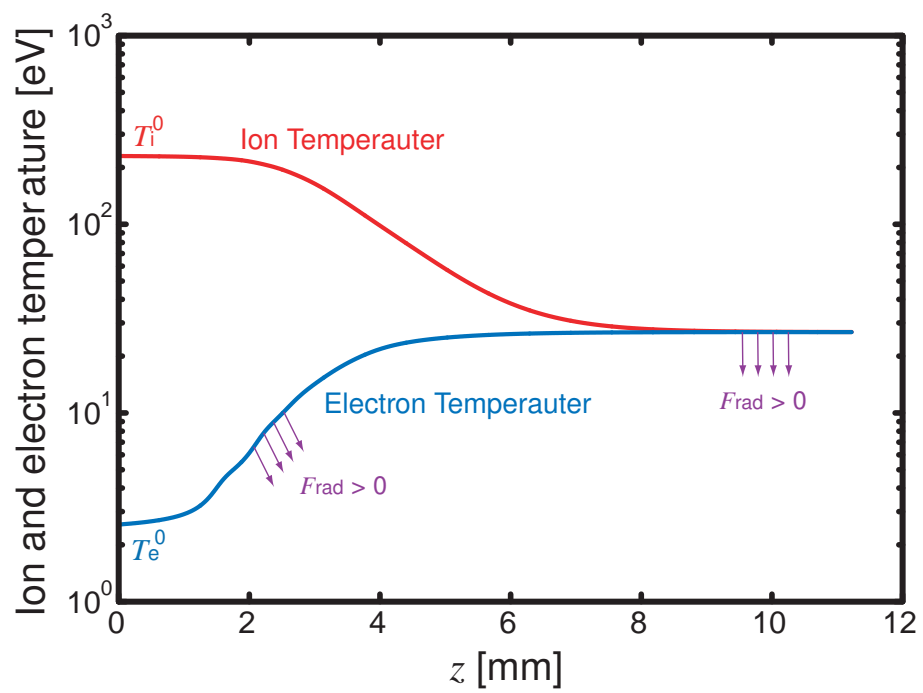


Figure 3.20: Schematic of radiation cooling effects on ion and electron temperature distributions

### **3.5 Concluding Remarks**

We calculated the physical parameters in the relaxation region of a strong shock wave under steady and planar condition. Before the discussion of the results, some atomic processes in shock wave and the calculation procedure were briefly summarized.

To estimate the strong shock waves with relaxation layer, we proposed comparative study between the calculation and the experiment using two fitting parameter: initial electron temperature and radiative flux. The calculation results showed that the structure of ionization relaxation layer strongly depends on the two fitting parameters: electron temperature at the shock front and radiative flux from the shock heated region. The results also indicated that the comparison between the calculation and our experiment is expected to allow us not only to discuss the relaxation layer of shock heated region but also to estimate precursor region and radiative transfer effect on the structure of strong shock wave.

# Chapter 4

## Measurement of Electron Temperature in Shock-heated Region by Spectroscopic Method

Our aim of this study is to make clear the physics and structure of electromagnetically driven strong shock waves. Comparative studies between experiment and calculation are important as shown in previous chapter for quantitative estimation of the strong shock with relaxation layer. In this chapter, the arrangement of electron temperature measurement by line pair method is addressed.

### 4.1 Fundamental Principle of the Measurement

The electron temperature profile was measured by a line pair method involving two spectral lines of same ionization stage [97]. In this section, the principle of the measurement is briefly shown in both optically thin and thick condition.

#### 4.1.1 Line Emission from Optically Thin Medium

We would like to start with optically thin case which means that radiation field is not planckian and line radiations is dominant.

The emission of atomic line radiation can be described by an emission coefficient  $\epsilon$  in J/s/m<sup>3</sup>/str, which has the following form:

$$\epsilon = \frac{1}{4\pi} h\nu_{ij} A(j \rightarrow i) N_{z,j}, \quad (4.1)$$

where  $i$  and  $j$  are lower and upper levels,  $\nu_{ij}$  is the resonant wavelength, and  $A(j \rightarrow i)$  is Einstein A coefficient as has been shown in Eq. (3.19). When we assume that spectrum profile  $\phi(\nu)$  does not depend on wavelength, the two line intensity ratio  $I_{i'j'}/I_{ij}$  is shown as,

$$\frac{I_{i'j'}}{I_{ij}} = \frac{h\nu_{i'j'} A(j' \rightarrow i') N_{z,j'}}{h\nu_{ij} A(j \rightarrow i) N_{z,j}}, \quad (4.2)$$

where  $I_{i'j'}$  and  $I_{ij}$  are the radiation intensity of particular levels of interest. When Boltzmann distribution can be assumed in the levels of the interested lines, the population ratio is written as shown in

$$\frac{N_{z,j'}}{N_{z,j}} = \frac{g_{j'}}{g_j} \exp\left(\frac{E_{j'j}}{T_e}\right), \quad (4.3)$$

where  $g_{j'}$  and  $g_j$  are statistical weight for  $j'$  and  $j$  levels,  $E_{j'j}$  is the energy gap from  $j'$  to  $j$  and  $T_e$  is electron temperature. We substitute Eq. (4.3) into Eq. (4.2) to obtain

$$\frac{I_{i'j'}}{I_{ij}} = \frac{g_{j'} h\nu_{i'j'} A(j' \rightarrow i')}{g_j h\nu_{ij} A(j \rightarrow i)} \exp\left(\frac{E_{j'j}}{T_e}\right). \quad (4.4)$$

Actually, as shown in Sec. 4.3.2, we measure values which are proportional to photon number  $N_p$ , therefore the ratio is show in

$$\frac{N_p(i'j')}{N_p(ij)} = \frac{g_{j'} A(j' \rightarrow i')}{g_j A(j \rightarrow i)} \exp\left(\frac{E_{j'j}}{T_e}\right). \quad (4.5)$$

In case of optically thin, we can estimate the electron temperature from Eq. (4.5).

### 4.1.2 Emission from Optically Thick Medium

When we assume optically thick condition, as show in Eq. (3.12), the spectrum radiation become the following planckian distribution:

$$B(\lambda, T) d\lambda = \frac{2hc^2}{\lambda^5} \frac{1}{e^{hc/\lambda k_B T} - 1} d\lambda, \quad (4.6)$$

where  $\lambda$  is the wavelength,  $T$  is the temperature,  $c$  is the speed of light,  $h$  is the Planck constant, and  $k_B$  is the Boltzmann constant. The photon number distribution  $f_p$  is described as the following:

$$f_p = \frac{1}{e^{hc/\lambda k_B T} - 1}. \quad (4.7)$$

Therefore, the ratio of two photon numbers:  $N_p(i'j')$  and  $N_p(ij)$  is shown in the following equation as,

$$\frac{N_p(i'j')}{N_p(ij)} = \frac{e^{hc/\lambda_{ij} k_B T} - 1}{e^{hc/\lambda_{i'j'} k_B T} - 1}. \quad (4.8)$$

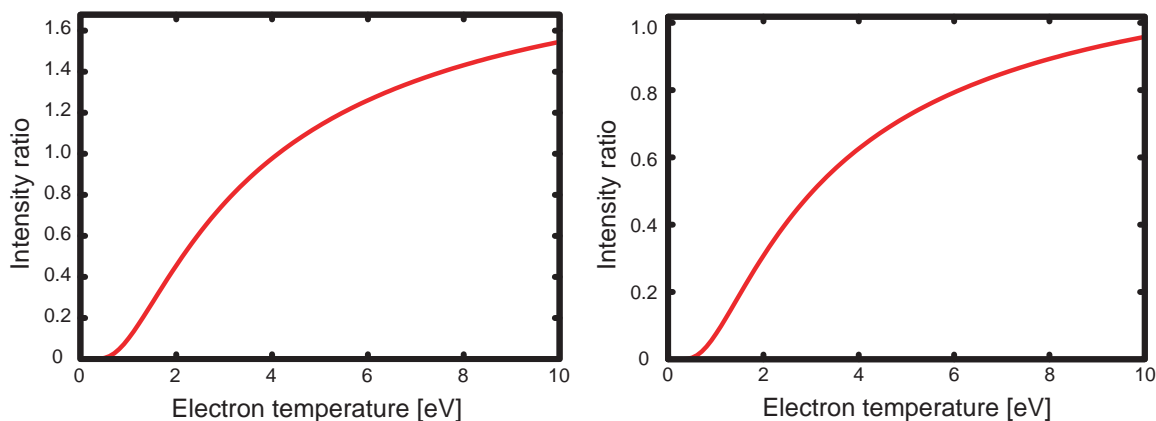
## 4.2 Selections of Wavelength

The dominant radiation spectrum observed from the experiment were those of Xe II. There are 22 available lines among many Xe spectral lines [89, 98]. Three lines: 433, 484, and 529 nm, were selected from these. The reason of the selection comes from sensitivity of temperature estimation from the ratio of the line intensities. The two ratios: 433-529 and 433-484, among three lines are selected for the temperature estimation. Golobic *et.al.*, also reported electron temperature measurement by the three lines in the different parameter [85]. The atomic data [98] of three lines are shown in Table C.1.

Table 4.1: Xe II data of three lines: 433, 484, and 529 nm

Wavelength nm	$A_r(j \rightarrow i)$ 1/s	$E_i - E_j$ eV	Configurations	$g_i - g_j$
433.052	$1.4 \times 10^8$	14.0737 - 16.9359	$5p^4(^3P_2)6p-5p^4(^3P_2)6d$	6 - 8
484.433	$1.1 \times 10^8$	11.5390 - 14.0976	$5p^4(^3P_2)6s-5p^4(^3P_2)6p$	6 - 8
529.222	$8.9 \times 10^7$	11.5390 - 13.8811	$5p^4(^3P_2)6s-5p^4(^3P_2)6p$	6 - 6

Here, we show the relation between the intensity ratio and the electron temperature in Figs. 4.1(a) and 4.1(b). They are derived from Eq. (4.5) using the atomic data above.



(a) Intensity ratio of the 433 and 529 nm

(b) Intensity ratio of the 433 and 484 nm

Figure 4.1: Relations between the intensity ratio and electron temperature

### 4.3 Setup for Electron Temperature Measurement

Temporal behaviors of the resonance lines were measured by a grating monochromator [JASCO International, Co., Ltd., CT25/N, 1200/mm] and a streak unit [Hamamatsu Photonics K.K., M2548 with C2830]. To synchronize streak time of spectrum line with the shock wave through the guiding tube, a delay pulse generator [Stanford Research System, Inc., DG 535] controlled the timing. First, the delay pulse setup and the streak unit are explained briefly. Then, basic characteristics of the spectroscopy: temporal and spatial resolutions of the setup and the sensitivity of wavelength are addressed.

#### 4.3.1 Delay Pulse Setup and Streak Image Camera

We show the top view of the experimental setup composed of the monochromator and the streak unit in Fig. 4.2. The exit slit of the monochromator were removed and the streak unit with temporal disperser [Hamamatsu Photonics K.K., M2548 with C2830] was directly attached to the exit port. The wavelength was calibrated and fixed by the dial gage, and a streak image of the fixed central wavelength was focused on the CCD surface.

The radiation emitted from shock heated region in the guiding tube is focused on

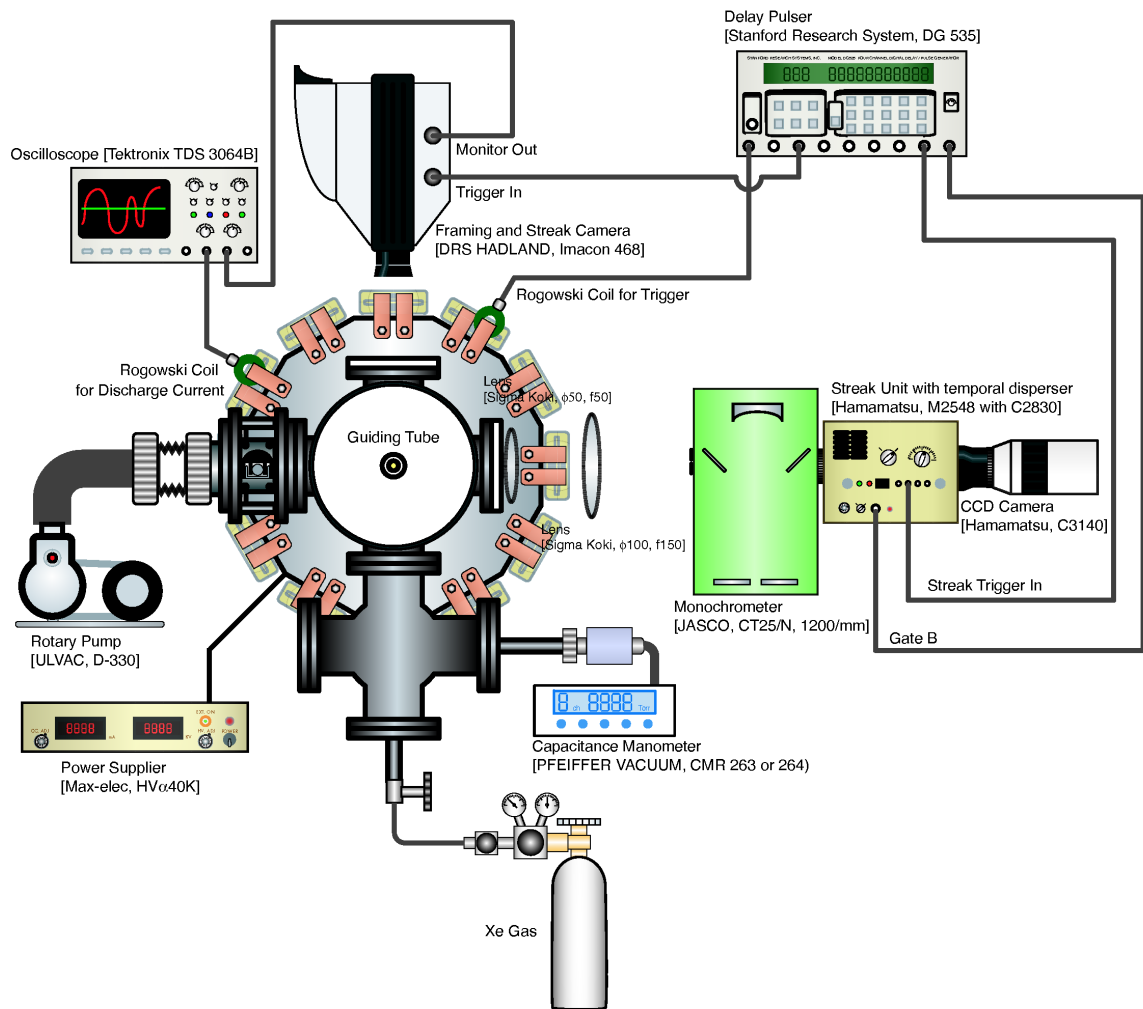


Figure 4.2: Top view of the experimental setup with basic diagnostics

the incident slit of the monochromator. The amplified spectrum is focused on the CCD surface. Digitized count numbers from the CCD are proportional to photon numbers. The output signal were corrected considering the quantum efficiency that depends on the wavelength [100].

Next, we consider the synchronization of the spectroscopic image system with the driven shock wave. The imaging system was started with the triggering Rogowski coil, as has been described in Sec. 2.4.2. The delay pulse generator controlled the framing camera [DRS HADLAND, Ltd., Imacon 468] and the streak unit. The exposure time of the framing camera was mostly 10 ns. As the streak unit has a delay time in the streak mode and the sweep time [100], we have to calibrate and synchronize the streak time with the shock wave arrival in the guiding tube. As shown in Appendix. B, we made calibration using a LED, which characterized the streak times as shown in Table 4.2.

Table 4.2: Evaluated sweep time and delay time of streak mode

Sweep time mode	Sweep time $\mu\text{s}$	Delay time $\mu\text{s}$
500ns/15mm	0.30	0.76
1 $\mu\text{s}$ /15mm	0.58	1.2
2 $\mu\text{s}$ /15mm	1.2	1.9
5 $\mu\text{s}$ /15mm	3.0	4.4
10 $\mu\text{s}$ /15mm	5.8	7.9
20 $\mu\text{s}$ /15mm	12	16

### 4.3.2 Spectroscope and Characteristics

The temporal and spatial resolutions of monochromator were estimated by the following procedure. The scattered light of Green LD laser [Photop Suwtech, Inc., DPGL-2200] ,  $\lambda = 532$  nm, from the guiding tube was focused to the vertical slit of the monochromator with two lens [Sigma Koki, Co., BK 7  $\phi$ 50 - f50 and BK 7  $\phi$ 100 - f150]. The focused image taken by the CCD camera [Hamamatsu Photonics K.K.,

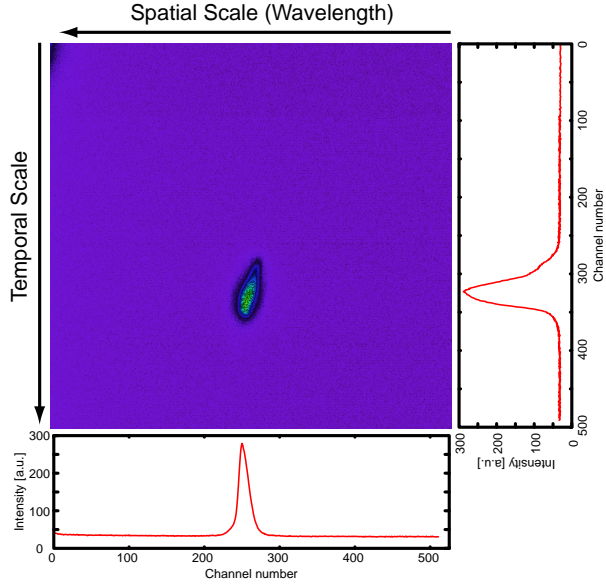


Figure 4.3: Focused image of the scattered light by LD Green Laser

Co., C3140] is shown in Fig. 4.3. Both vertical slit width of the monochromator and horizontal slit of streak unit are  $100 \mu\text{m}$  in this study. The temporal resolution of this set up, which corresponds to full width at half maximum (FWHM) for the vertical profile, is estimated to be  $\sim 33$  ch for 491 ch. Whereas, the spatial resolution of this set up, which corresponds to the horizontal profile, is  $\sim 15$  ch for 511 ch. As usual, the color pattern in the image means that red is stronger and blue is weaker.

## 4.4 Electron Temperature Distribution

In this section, we show the result of electron temperature measurement. To compare the experimental results with the calculation result as shown in Sec. 3.4, the result for two cases: 0.12 and 0.75 Torr, are shown. The estimation of the line intensity is by integrating the total count number from the central fixed line. We assume no channel sensitivity dependence in the typical line spread of about 40 ch.

#### 4.4.1 Electron Temperature Distribution for Case of $p_1 = 0.12$ Torr

The line ratios were measured for  $p_1 = 0.12$  Torr. As above, the two ratios: 433-529 nm and 433-484 nm are selected in the two-line intensity ratio technique. First, the spectrum profile of 433.0 nm from Xe II is shown in Fig. 4.4. This emission was measured at 40 mm from the bottom of the guiding tube and the streak mode was  $2\mu\text{s}/15\text{mm}$ . MCP voltage in the streak unit was set in the same value for every experiment. The color pattern shows the emission intensity. In Fig. 4.4, the right orange line profile, which was obtained by integrating the count numbers between vertical orange lines, means the photon number distribution of Xe II line of  $\lambda = 434.0$  nm. This was used for estimating the electron temperature. We corrected the effects of continuum lines and avoided vicinal region of strong emission lines. In Fig. 4.4, the bottom pink line profile, was obtained by integrating the count numbers between horizontal pink lines, which is roughly shows the relation between wavelength and intensity. However, since only the center line is focused on the CCD, the intensity distribution for wavelength from this profile is not appropriate. The Xe II line,  $\lambda = 424.5$  nm, was identified as shown in the bottom profile. This line was identified when the line was the focused center position. However, the line at ch 400 could not be identified and the unknown line may be from an impurity.

Next, the spectrum profile of 484.4 nm line from Xe II is shown in Fig. 4.5. The experimental condition is the same with 433.0 nm measurement. In Fig. 4.5, the right orange and the bottom pink line profiles are also same meaning. As shown in the bottom of the profile, two remarkable lines: 492.1 and 487.6 nm from Xe II were identified.

And then, the spectrum profile of 529.2 nm from Xe II was measured, of which result is shown in Fig. 4.6. The experimental condition is same one in 433.0 nm. In Fig. 4.6, the right orange and the bottom pink line profiles are also same meaning. In the bottom profile, the three remarkable lines: 537.2, 533.9, and 526.1 nm from Xe II were also identified.

We could estimate electron temperature from the three spectrum profiles. Since

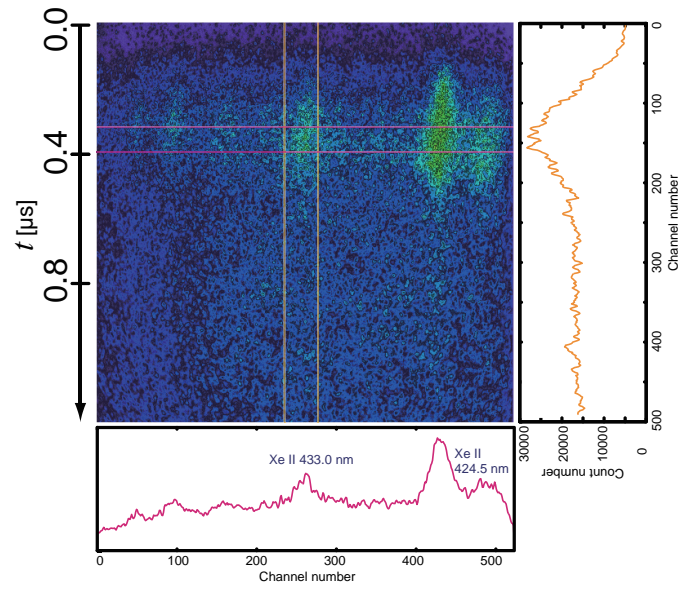


Figure 4.4: Streak spectral image of 433 nm for  $p_1 = 0.12$  Torr

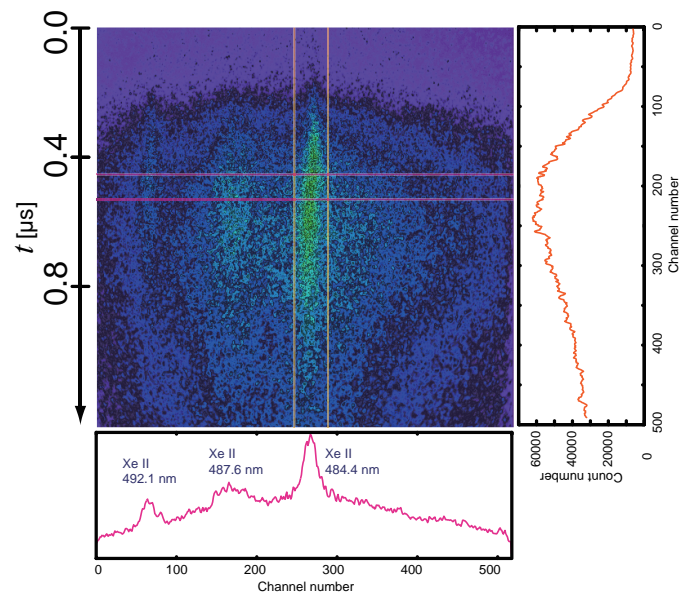


Figure 4.5: Streak spectral image of 484 nm for  $p_1 = 0.12$  Torr

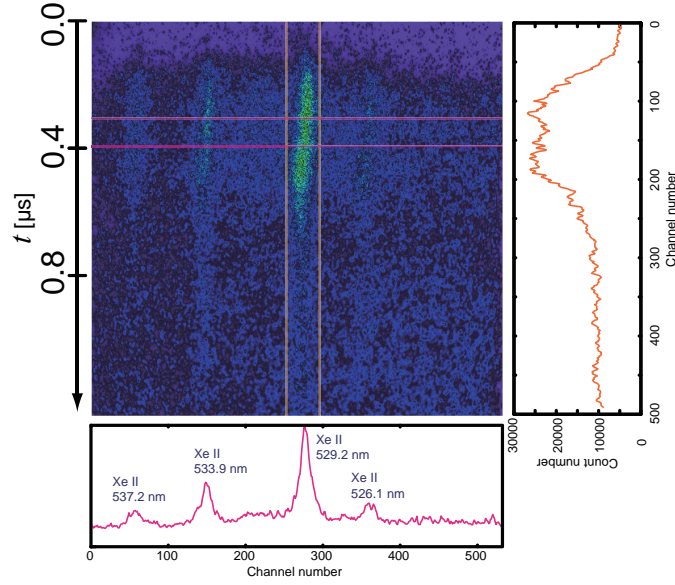


Figure 4.6: Streak spectral image of 529 nm for  $p_1 = 0.12$  Torr

the temporal resolution is  $\sim 33$  ch as shown in Sec. 4.3.2, the photon number profile for the center line was divided per this range and electron temperature was by the ratio of the average of value integrated between this region. Electron temperature profile along the spatial scale can be estimated because the shock wave driven by our device can be considered as steady and planar shock as shown in Sec. 2.5.1 and the temporal scale can be converted to the spatial scale. As shown in Table 4.2, the sweep time in this condition is  $1.2 \mu\text{s}$ . When initial pressure  $p_1$  is 0.12 Torr, shock front velocity  $u_s$  is  $\sim 30$  km/s as has been shown in Table 3.2. The flow velocity  $v_c$  behind the shock front derived from one-dimensional mass conservation law, is  $3u_s/4$ . Thus, the sweep time,  $1.2 \mu\text{s}$ , can be converted to the spatial scale, 27 mm. Here, we assume that the emission region is behind shock front and the flow velocity is constant. Here, the starting point of the emission is defined as the arrival time of peak-value/20.

As shown in Fig. 4.7, we show the electron temperature profile for  $p_1 = 0.12$  Torr, based on optically thin from Eq. (4.5) and optically thick condition from Eq. (4.8). Electron temperature profile in further downstream region,  $z > 12$  mm, is not shown in Fig. 4.7 because the emission from Xe II is too weak to estimate it.

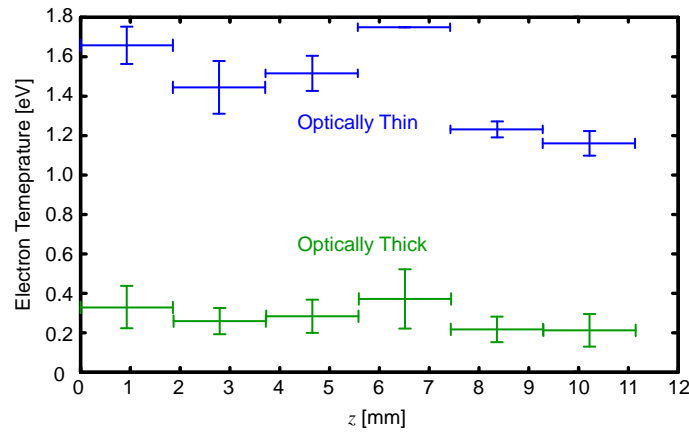
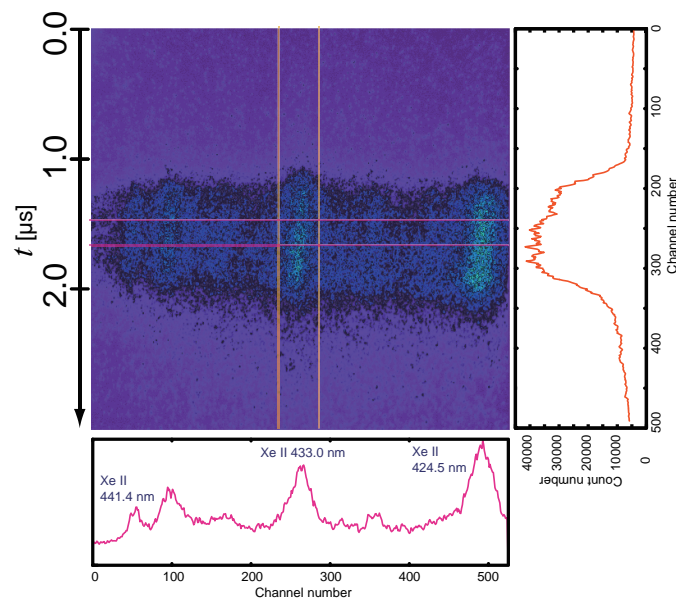
Fig. 4.7 shows that the profile is not vastly changed for both optically thick and thin cases. The constant value can not be understood by the calculation results, in which only ion-electron relaxation process was taken into consideration as shown in Sec. 3.3.

Here, we have to confirm that the populations of the levels keep the Boltzmann distribution because this estimation for optically thin is based on this assumption. It is significant that the radiative decay rate and collisional deexcitation rate are compared to judge the assumption in this situation. We assume that  $T_e \sim 2.0$  eV, total ion number density behind shock front  $N_i^0 = 1.7 \times 10^{16}$  1/cm<sup>3</sup>, which is corresponding to four times of that in 0.12 Torr by shock compression, for the estimation. By using electron number density  $N_e$  obtained by equilibrium condition and electron temperature  $T_e$ , Eq. (3.17) gives collisional deexcitation rate. When we compared the collisional deexcitation rate to radiative decay rate  $A_r(j \rightarrow i)$  of three lines: 433, 484, and 529 nm, both were comparable. Then, the each level is considered not to deviate significantly from the Boltzmann distribution. However, as the full LTE approximation may not be appropriate in this condition, the measured temperature is considered to be an excited temperature rather than the real electron temperature. Whereas, since the line radiations is dominant in this situation, the estimation based on planckian distribution is also not appropriate. Further investigation about the shock structure is addressed in the next chapter.

#### 4.4.2 Electron Temperature Distribution for Case of $p_1 = 0.75$ Torr

The line ratios were measured for  $p_1 = 0.75$  Torr as well as the case of  $p_1 = 0.12$  Torr. The experimental condition is same one in 0.12 Torr. First, the spectrum profile of 433.0 nm from Xe II is shown in Fig. 4.8. As shown in the bottom profile of Fig. 4.8, the Xe II lines: 424.5 nm and 441.4 nm, were identified.

Next, the spectrum profile of 484.4 nm from Xe II is shown in Fig. 4.9. The experimental condition is the same as that of 433.0 nm. In the bottom profile, the two remarkable lines: 492.1 and 487.6 nm from Xe II were identified.

Figure 4.7: Electron temperature distribution for  $p_1 = 0.12$  TorrFigure 4.8: Streak spectral image of 433 nm for  $p_1 = 0.75$  Torr

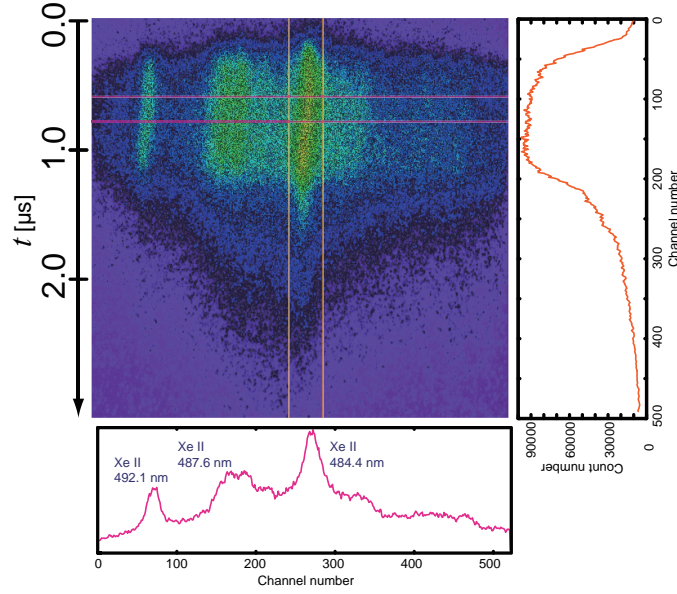


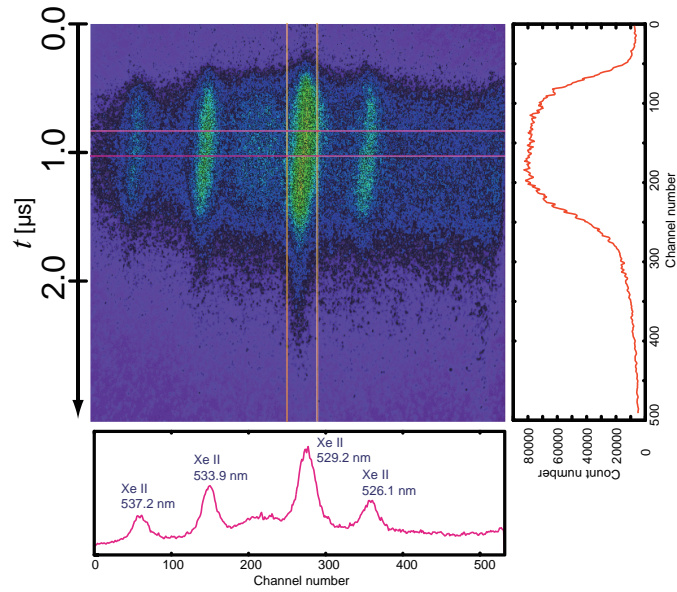
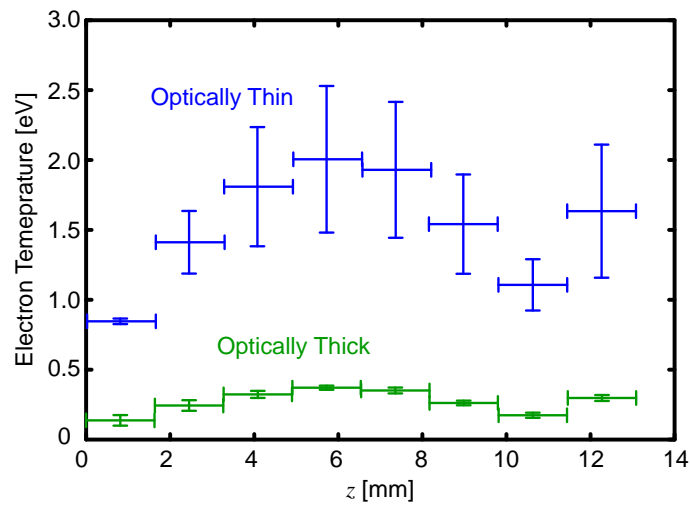
Figure 4.9: Streak spectral image of 484 nm for  $p_1 = 0.75$  Torr

And then, the spectrum profile of 529.2 nm from Xe II is shown in Fig. 4.10. The experimental condition is the same. In the bottom profile, the three remarkable lines: 537.2, 533.9, and 526.1 nm from Xe II were identified.

As shown in Fig. 4.11, we show the electron temperature profile for  $p_1 = 0.75$  Torr, based on optically thin condition from Eq. (4.5) and optically thick condition from Eq. (4.8). The electron temperature was also approximately constant value,  $T_e \sim 2$  eV as well as that in 0.12 Torr. The electron temperature profile shown in Fig. 4.11 can not be explained by the calculation results shown in the previous section.

As well as 0.12 Torr case, the populations of the levels may deviate a little bit from the Boltzmann distributions and the estimation as the excited temperature may be appropriate.

Since a line broadening (FWHM) is not different in both cases of  $p_1 = 0.12$  and 0.75 Torr, the optical thickness in these conditions is considered to be small. Then, this means the estimation based on black body assumption is not appropriate.

Figure 4.10: Streak spectral image of 529 nm for  $p_1 = 0.75$  TorrFigure 4.11: Electron temperature distribution for  $p_1 = 0.75$  Torr

## **4.5 Concluding Remarks**

We measured electron temperature profiles in the shock heated region of electro-magnetically driven strong shock waves by line pair method. Before that, we addressed briefly the measurement principle for optically thin and thick cases.

The experimental results showed that the electron temperature of shock heated region keeps an almost constant value. We would like to point out that the situation can not be explained by conventional relaxation process, in which electrons get energy by electron-ion collision and their temperature is expected to monotonously increase with distance from the front. To make clear this point, we will discuss the structure of electro-magnetically driven strong shock wave through a comparative study between the experimental observation and numerical simulation in the next chapter.

## Chapter 5

# Estimation of Electro-magnetically Driven Strong Shock Waves with Relaxation Layer

The electron temperature profiles were estimated from Xe II lines as shown in Sec. 4.4. The results indicated that an area with the constant electron temperature is extending unexpectedly over a wide region. In this chapter, we show three possible factors affecting the electron temperature: emission from discharge plasma, initial ionization in the shock waves and radiative cooling. After physical estimation of our electro-magnetically driven shock waves, finally, a relation between our experiment and radiative SNRs is discussed.

### 5.1 Emission from Shocked Region

In this section, we discuss a possible factor: discharge plasma, which may affect the electron temperature profile. After that, we also show that experimental system is steady state and streak emission pattern is consistent with the framing images of integrated emission profile.

Though electron temperature profile is affected by ion-electron and ionization relaxation, and radiation processes in the shocked region, it is also expected to change

from the shocked region to a “discharge plasma” region. Discharge plasma is the region behind shocked region and this may include the ions sputtered from electrodes and ablated from the insulator. Therefore, we need to check whether the observed line emissions include the effect of the discharge plasma region. Now, since we can assume the shock wave is planar and steady, the shocked region is expected to spread uniformly with time. If an line emission includes the discharge plasma, the emission scale length must change with time.

To investigate it, emission scale lengths of Xe II line,  $\lambda = 434$  nm from different observation points: 2.0, 4.0, and 5.5 mm from the bottom of the guiding tube are compared with the same condition. We show those spectrum profiles for  $p_1 = 0.12$  Torr in Fig. 5.1. Here, the horizontal axis in Fig. 5.1 is temporal scale and  $t = 0$  means initial rise of the spectrum profile. In the figure, the peak values are normalized because the solid angles for each observation points are different, and the starting points of the emission are aligned. As shown in Fig. 5.1, the full width at half maximum (FWHM) of the emission spectrum profiles is nearly equal. Thus, the Xe II line emission can be considered not from the discharge plasma in this condition. Moreover, the fact that the profiles are independent on observation points indicates the shocked region is in steady state.

Whereas, we estimate the scale length of shocked region roughly. In this condition, since the shock front velocity  $u_s$  is 30 km/s, the velocity of the contact surface which means the boundary between the shocked region and the discharge plasma region, is estimated to be about 23 km/s, using the relation of  $3u_s/4$  based on the classical Rankine-Hugoniot Relation. Thus the length of the shocked region is expected to be a few cm because a few  $\mu s$  passed after discharge. As well as, the emission time scale:  $\sim \mu s$  in Fig. 5.1 can also be converted to the scale length:  $\sim$  cm. Then, the emission scale length is the order of the shocked region and this estimation also shows that the strong emission region is in the shock heated region.

In addition, the possibility that the line emissions is not from shocked region but from the precursor region is also unreasonable. Precursor region is formed by mainly electron heat conductivity and/or photoionization as has been shown in Sec. 2.1.5 and this region is considered to be extremely diffusive region. As above, the

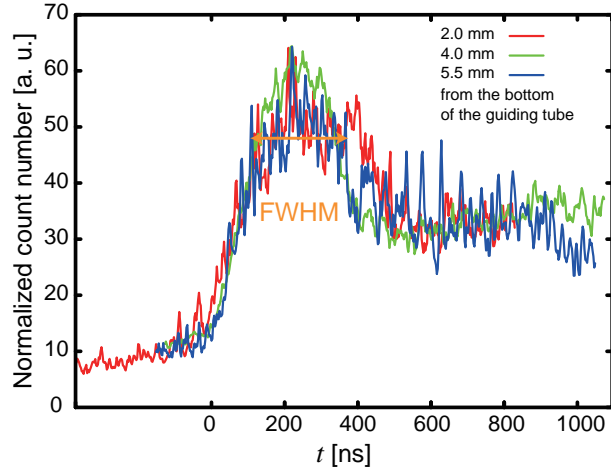


Figure 5.1: Streak profiles of  $\lambda = 434$  nm for different observation points in case of  $p_1 = 0.12$  Torr

clear start edge of the self-emission by the fast framing camera and the spectroscopic measurement indicate that the emission region is not from diffusive precursor but from the shock front.

The streak profile of Xe II line,  $\lambda = 434$  nm, for  $p_1 = 0.75$  Torr is shown in Fig. 5.2. Here, the profiles are also normalized and aligned. As shown in Fig. 5.2, the profiles are independent of observation points, and it is shown that their behavior is also steady. The FWHMs of the emission spectrum profiles for all observation points are nearly equal as well as for the case of  $p_1 = 0.12$  Torr. Thus, the Xe II line region can be also considered not to be disturbed by the discharge plasma.

Next, we investigate the region of strong Xe II line for consistency between streak profiles and framing images. At first, the case of  $p_1 = 0.12$  Torr is discussed. The presence region of strong Xe II lines is estimated to be  $\sim 3$  mm from the FWHM of Xe II line,  $\lambda = 434$  nm, as in Fig. 5.1 and the comparable temporal resolution of the spectral streak image in Sec4.3.2. This tendency of spectrum profile form is similar to the other Xe II lines observed in the experiments. We show a framing image of the shock region obtained by Imacon 468 in this condition in Fig. 5.3. The color pattern means that red is stronger and blue is weaker, as usual. In Fig. 5.3, the bright area in the front region extends for  $\sim 2$  mm, and this may be considered to

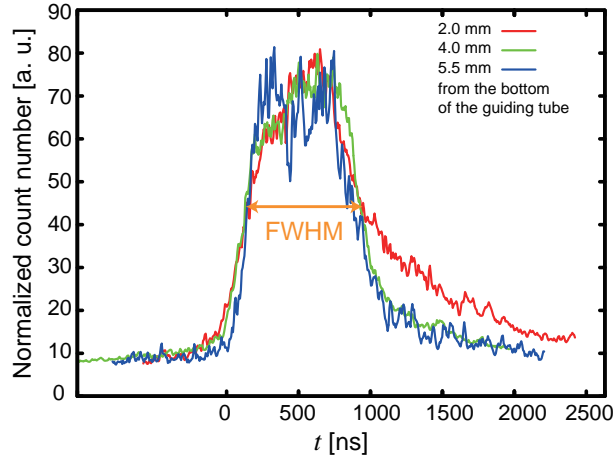


Figure 5.2: Streak profiles of  $\lambda = 434$  nm for different observation points in case of  $p_1 = 0.75$  Torr

be the presence region of strong Xe II lines. And, the dark area behind the bright region is also corresponding to be the spatial scale of the spectroscopic results. The dominant lines of dark area can be considered from Xe III and/or more ionized ion, since the dominant wavelength of the spectrum Xe III and/or more ionized ion lines is shorter than 400 nm which is the lowest wavelength of sensitivity in this experiment. Golobic *et.al.*, reported that the Xe III dominated the spectra below 400 nm [85], however, the line emissions through the acrylic guiding tube in this experiment is too weak to observe them at below 400 nm. It is reasonable to consider based on ionization relaxation as shown in the calculations that more ionized ions exist behind Xe II ions. As above, the framing emission pattern is considered to be consistent with the spectroscopic results.

The same prospect about the region of the strong Xe II line is reviewed in the case of  $p_1 = 0.75$  Torr for the consistency between streak line profiles and framing pictures. The converted spatial scale length of the strong Xe II emission region is estimated to be  $\sim 4.5$  mm from the FWHM of the line emission shown in Fig. 5.2 and the comparable temporal resolution. We show a framing image of the shock region obtained by Imacon 468 in this condition in Fig. 5.4. The color pattern means that red is stronger and blue is weaker, as usual. In Fig. 5.4, the strong bright area

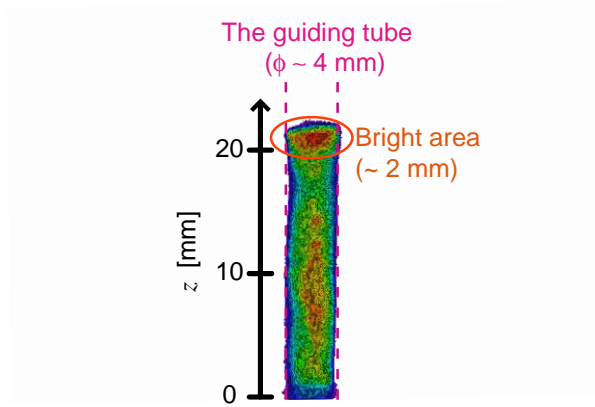


Figure 5.3: Framing image of shock wave through the guiding tube in case of  $p_1 = 0.12$  Torr

in front region is extending for  $\sim 5$  mm, and this is considered to be the presence region of strong Xe II lines. Thus, as well as  $p_1 = 0.12$  Torr case, the framing emission pattern can be considered to be consistent with the spectroscopic results.

## 5.2 Initial Ionization by Atom-atom Collisional Ionization in Shock Structure

In Sec. 5.1, we showed that the measurement results for electron temperature were not disturbed by discharge plasma. Next, we consider the second possible factor which affects the electron temperature profile. That is initial ionization process as shown in Secs. 2.1.4 and 3.4.4. Especially, in Sec. 3.4.4, it was shown that poor “priming” electrons cause no ion-electron relaxation and freezing ion and electron temperatures. We consider whether the initial ionization is the main factor of the constant electron temperature profile observed by our experiment.

The spectrum line emissions from 400 to 700 nm were investigated by the spectroscopic measurement, however, almost lines are identified to be from Xe II and we didn’t observe any strong lines from Xe I, although a few unknown lines existed. This may be come from the fact that any Xe I lines don’t have larger oscillator strength

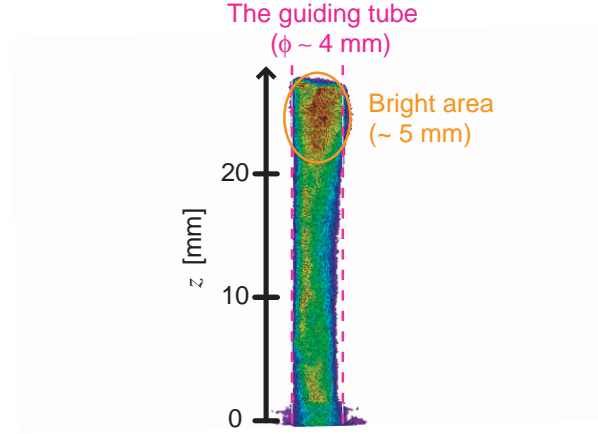


Figure 5.4: Framing image of shock wave through the guiding tube in case of  $p_1 = 0.75$  Torr

than that of Xe II in this wavelength region [98]. Thus, our experimental setup may observe only Xe II lines and it is difficult to estimate initial ionization by the transition from Xe I to Xe II.

As shown in Fig. 5.1, the time scale of initial rise of Xe II line emission profile is about 100 ns. When we assume that most of Xe I atoms are ionized to Xe II ions in this initial rise and that initial ionization is caused by only atom-atom collisional ionization, we can estimate the reaction cross section  $\sigma_{a-a}$ .

The mean free path  $\lambda_{a-a}$  for atom-atom collisional ionization process can be written as shown in

$$\lambda_{a-a} \sim v_a \Delta t \sim \frac{1}{N_a \sigma_{a-a}}, \quad (5.1)$$

where  $v_a$  is ion velocity,  $\Delta t$  is the collision time,  $N_a$  is the atomic number density and  $\sigma_{a-a}$  is the cross section for the atom-atom ionization cross section, and  $\Delta t$  is  $\sim 100$  ns which is based on the time scale of initial rise in Fig. 5.1 for the case of  $p_1 = 0.12$  Torr.

We assume that the atom-atom collisional ionization process occurs within  $\Delta t \sim 100$  ns in this condition. To satisfy this assumption, the atom-atom ionization cross

section is estimated as shown in

$$\begin{aligned}\sigma_{a-a} &\geq \frac{1}{N_a v_a \Delta t}, \\ &\geq 2.0 \times 10^{-16} \text{ (cm}^2\text{)},\end{aligned}\tag{5.2}$$

where  $N_a$  is equal to  $N_i^0 = 1.7 \times 10^{16} \text{ 1/cm}^3$ ,  $v_a$  is shock front speed, 30 km/s. This estimation indicates that the cross section must be larger than  $2.0 \times 10^{-16} \text{ cm}^2$ . Whereas, we estimate the atom-atom ionization cross section in this condition from Eq. (3.21), to be

$$\sigma_{a-a} \sim 1.3 \times 10^{-16} \text{ (cm}^2\text{)}.\tag{5.3}$$

Eqs. (5.2) and (5.3) show that the predicted value of the cross section is the same order of the semiclassical formula [54]. Thus, the predicted value is considered to be reasonable. Whereas, Kelly *et.al.*, estimated the cross sectional slope  $C$  as  $C \sim 10^{-20} \text{ cm}^2/\text{eV}$  [59]. If ion energy is near the ionization threshold energy, that is about 12 eV, the cross section near the threshold depends linearly on the ion energy [10]. Since the ion temperature  $T_i^0$  is order of  $\sim 200 \text{ eV}$  in this condition as shown in Table. 3.2, the linear scaling with the cross sectional slope  $C$  may not be appropriate. For the case of  $p_1 = 0.75 \text{ Torr}$ , there is also the same tendency.

We showed that atom-atom collisional ionization supplies enough ‘‘priming’’ electrons in the narrow region and that initial ionization problem is considered not to be the main factor for the constant electron temperature. Since our calculation in Sec. 3.4.4 did not include atom-atom collisional ionization process, enough initial ionization could not be estimated.

### 5.3 Radiative Cooling in Shock Waves

We discuss radiative cooling which restricts the rising of electron temperature by ion-electron relaxation. The proposed estimation method of radiative flux in shock waves as shown in Sec. 3.4.6 is used.

The enough transition from Xe I to II in narrow region, which is about  $\sim \text{mm}$  in  $p_1 = 0.12 \text{ Torr}$ , was shown in the previous section. Since the thickness of the

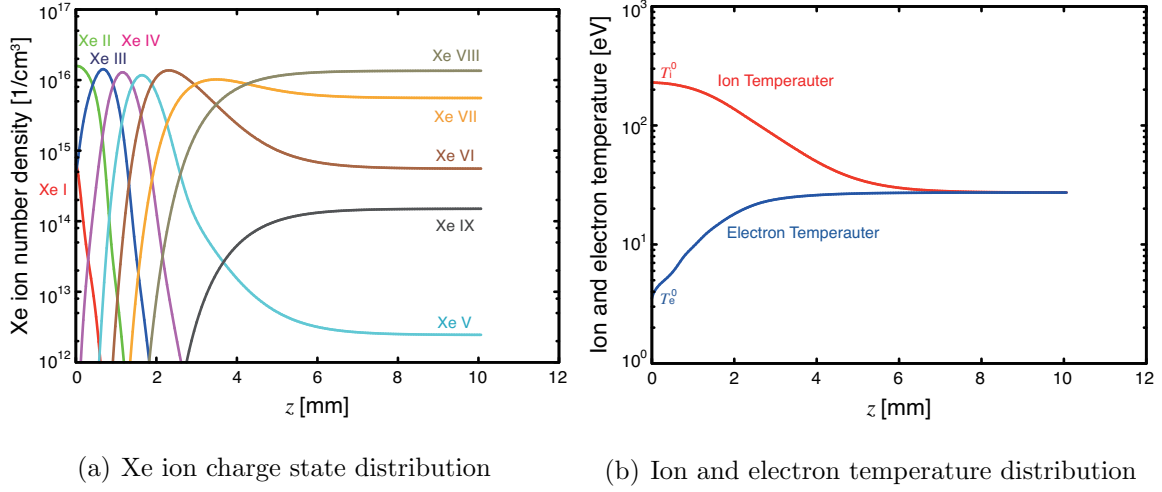


Figure 5.5: Relaxation layer of shock heated Xe for  $T_e^0 = 3.5$  eV at  $p_1 = 0.12$  Torr

compression shock is approximately two to three gaskinetic atomic mean free paths, the length is considered to be also  $\sim$  mm in  $p_1 = 0.12$  Torr. Thus, we can assume that there is the region of enough ionized Xe behind the shock front.

We fix that initial electron temperature  $T_e^0$  is 3.5 eV. This value was obtained by equilibrium rate equations corresponds to the Xe II dominant condition. In the condition, there are enough “priming” electrons to ionize and we can refrain the effect of initial ionization. Since the experimental results by the line pair method reflects not real electron temperature but an excited temperature, this slightly higher temperature, 3.5 eV, than experimental value,  $\sim$  2 eV, may be justified.

At first, as well as Sec. 3.4, we show calculation results of Xe ion charge state distributions, and ion and electron temperature distributions for  $T_e^0 = 3.5$  eV at  $p_1 = 0.12$  Torr without  $F_{\text{rad}}$  as shown in Figs. 3.11(a) and 3.11(b). As usual,  $z = 0$  indicates the location of shock front, and the shock condition is the same as Table 3.2 at  $p_1 = 0.12$  Torr.

In this condition, electron temperature increases to 10 eV in  $\sim$  mm scale and the existence region of Xe II is also estimated to be  $\sim$  mm. This behavior cannot explain the experimental observation.

Here, we consider a radiative cooling effect. We assume that optical thickness in

our system is thin and that the populations for all level are Maxwellian. Therefore, total radiative flux  $F_{\text{rad}}$  in a local region  $dz$  is shown as the following:

$$F_{\text{rad}} = \sum_z \sum_j h\nu_{ij} A_r(j \rightarrow i) N(z, j) dz, \quad (5.4)$$

where  $z$  is the charge state,  $i$  and  $j$  are the  $i$  and  $j$ th levels of bound electron,  $h$  is the Planck constant,  $A_r(j \rightarrow i)$  is radiative decay rate, and  $N(z, j)$  is the population. As there are only 22 available lifetimes of states of Xe II for Xe ion [98] (in more detail, see Appendix. C), we cannot estimate accurate radiative flux. Here, we define the radiative flux integrating the 22 known lines of Xe II as  $F_{\text{rad}}^*$  as the following:

$$F_{\text{rad}}^* = \sum_u h\nu_{lu} A_r(u \rightarrow l) N_u dz \quad (5.5)$$

$$= \sum_u h\nu_{lu} A_r(u \rightarrow l) \frac{g_u}{g_g} N_g \exp(-E_u/k_B T_e) dz, \quad (5.6)$$

where  $N$  is population,  $E$  is energy of level,  $k_B$  is the Boltzmann constant,  $T_e$  is electron temperature, and subscript “u” means upper level, “l” means lower level, and “g” means ground level. We evaluate total radiative flux  $F_{\text{rad}}$  using  $F_{\text{rad}}^*$  as shown in

$$F_{\text{rad}} = \beta F_{\text{rad}}^* \quad (5.7)$$

where  $\beta$  is a constant. Since the calculation can estimate the populations of ground state as shown in Sec. 3.4,  $F_{\text{rad}}^*$  can be evaluated.

When the radiation flux is considered, energy equation Eq. 3.28 can be written

$$\rho u \left[ \frac{1}{2} u^2 + \frac{5}{2} R(T_i + \alpha T_e) + \frac{1}{N_i} \sum_{j=1}^{20} N_{\text{Xe}^{j+}} R T^{j+} \right] + \beta F_{\text{rad}}^* = E(z). \quad (5.8)$$

Here, it is assumed that radiative energy density, radiative pressure and thermal heat conductivity are neglected for estimating the contribute of radiative flux. Using Eq. (5.8) with radiation flux, we calculate ion and electron temperature distributions for  $T_e^0 = 3.5$  eV at  $p_1 = 0.12$  Torr with  $\beta$  as a parameter. The result is shown in Fig. 5.6 and the shock condition is the same of Figs 3.11(a) and 3.11(b).

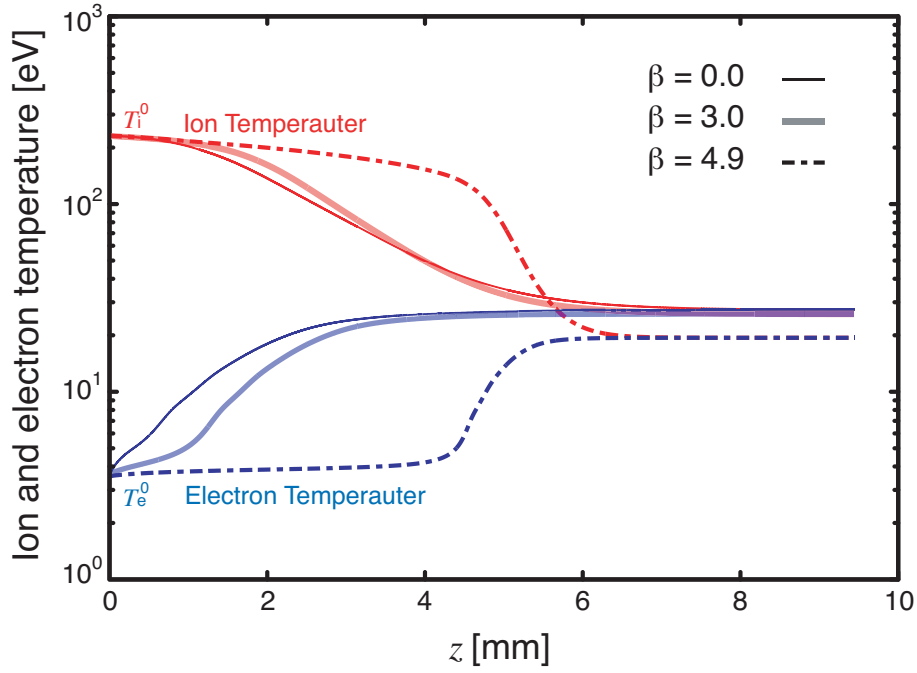


Figure 5.6: Ion and electron temperature distributions with radiative flux factor  $\beta$

As shown in Fig. 5.6, the rise of electron temperature is restricted with increase of  $\beta$ . Especially, for  $\beta = 4.9$ , electron temperature keeps constant in wide region, several mm scale.

On the contrary, the decay of ion temperature is restricted with increase of  $\beta$ , due to inefficient ion-electron relaxation as shown Eq. (3.33). The relaxation process depends on the ion charge  $Z_i$  and the constant ion charge  $Z_i$  (See Fig. 5.7(a)) until  $z = 4$  mm relatively limits the decay of ion temperature.

In the condition,  $\beta = 4.9$ , we show calculation results of Xe ion charge state distributions, and ion and electron temperature distributions in Figs. 5.7(a) and 5.7(b).

As shown in Fig. 5.7(a), the radiative flux lengthens the existence region of Xe II. The behavior of radiative flux can reasonably explain the experimental results.

At  $z \sim 5$  mm, ion-electron relaxation rapidly occurs and the population of Xe III increases. Since in this estimation we consider the radiative flux from only Xe II,

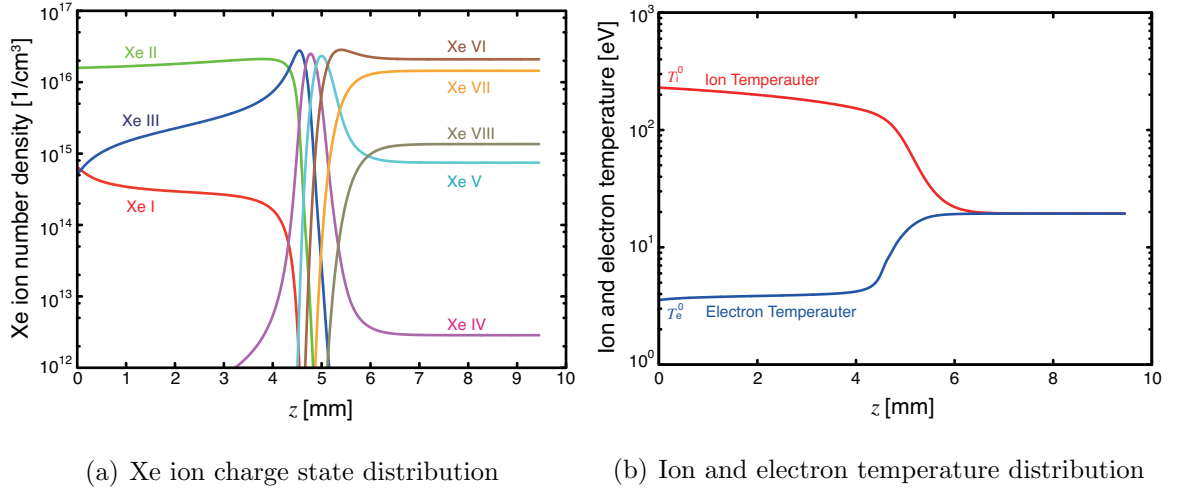


Figure 5.7: Relaxation layer of shock heated Xe with radiative flux ( $\beta = 4.9$ ) for  $T_e^0 = 3.5$  eV at  $p_1 = 0.12$  Torr

the radiative effect must be underestimated in the Xe III dominant region. Thus, the evolutions from  $z \sim 5$  mm is not appropriate. Although the estimation is considerably simplified we emphasize that we can show the importance of radiative flux for the formation of structure of the electro-magnetically driven shock waves.

## 5.4 Relation between Electro-magnetically Driven Strong Shock Waves to Radiative SNRs

Establishing similarity and/or scaling of radiation hydrodynamics between the astrophysical phenomena and the laboratory experiments is a difficult and a challenging task. The radiative contribution to shock waves complicates their behavior even without considering interaction between the radiation transport and the hydrodynamics. For simplification of scaling to astrophysical phenomena, we assume that the radiation transport is local. This means that the system of interest should be strictly either optically thin or optically thick. Here, radiative-flux regime is considered, which means optically thin. When we may be able to express  $\nabla \cdot F_{\text{rad}}$  as a power law function of density and pressure in both of astrophysical and laboratory plasma, the Euler equation for energy with the radiative flux can be converted to an invariant

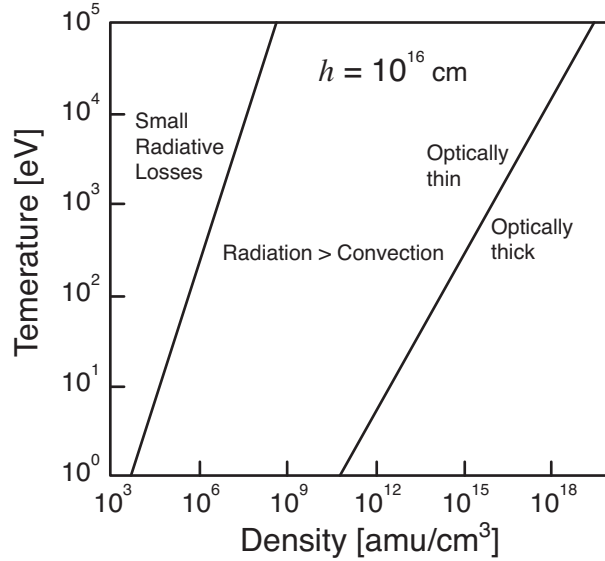


Figure 5.8: Relation between temperature and density for radiative effect and optical depth on the spatial scales  $h = 10^{16}$  cm of young SNRs [7]

between two systems [8, 14].

In some supernovae (SNe), the radiative losses are considered to be significant [15–19]. Fig. 5.8 shows the physical property on the spatial scales appropriate to young SNRs [7]. As shown in Fig. 5.8, there is a large range of densities for which radiative losses dominate over convection while the system remains optically thin.

In the previous section, we estimated the contributions of radiative flux using  $F_{\text{rad}}^*$  and consequently we concluded that the radiative cooling in our experimental system may be important for the shock structure.  $F_{\text{rad}}^*$  is based on atomic property, however, if it is modeled as a power law function of hydrodynamic parameters such as density and pressure, and an invariant is instituted. Then, a scaling to above radiative SNRs can be established. Our experiment may be appropriate to model a local region of an evolving spherical SNR, for a limited time, which means that the effects of spherical divergence are not important. Although there are many problems and we need more sophisticated design effort, we conclude that this experiment can be an useful test bed to scale up a laboratory level observation to astrophysical phenomena.

## 5.5 Concluding Remarks

In this chapter, we discussed main factors which keep the electron temperature at a rather low value in the unexpected wide range of strongly shock heated region. It was confirmed that the observed line emissions were from shock heated region and that the measurement results for electron temperature were not disturbed by the discharge plasma. We estimated the cross section of atom-atom collisional ionization to be  $\geq 10^{16} \text{ cm}^2$  from the initial rise of spectrum profile Xe II, and it was shown that the atom-atom collision plays significant roles for the formation of the shock jump layer. Since the region behind shock front is considered to be ionized plasma by atom-atom collision, initial ionization problem, which means that poor “priming” electrons cause no ion-electron relaxation, is inappropriate for the interpretation of the observation. We showed that radiative effect is important for the formation of shock structure. The radiative cooling restricts the rise of electron temperature in ion-electron relaxation layer and delays the ionization relaxation. This behavior can correspond to the experimental results. Finally, a relation between our experiment and radiative SNRs was discussed. Our electro-magnetically driven shock waves with radiative cooling is considered to be an useful test bed for scaling of laboratory experiments to radiative SNRs.

# Chapter 6

## Conclusions

In this thesis, we have discussed the relaxation layer of electro-magnetically driven strong shock waves.

Chapter 1 started with an introduction to strong shock waves and their related astrophysical phenomena. Strong shock waves, those are remarkable non-equilibrium phenomena, change the structure with relaxation layer when the physical parameters are shifting. Our electro-magnetic method has a character of generating extremely strong shock wave in rather low density gas. Relaxation and dissipative processes in the low density shock heated high  $Z$  gas have not been researched enough due to the complexity of phenomena. We discussed the strong shock wave with multi-scale relaxation layer and indicated that the critical point of this study is the estimation of electro-magnetically driven strong shock waves with relaxation region through a comparative study of steady and 1-D shock experiments and calculations based on the steady and 1-D shock wave.

In chapter 2, we showed an electro-magnetic device, in which the electro-magnetically driven shock waves have been demonstrated. It can produce steady and one-dimensional high Mach number shock waves. The shock Mach number reached  $M \sim 200$  in low density Xe gas. In this region, it is indicated that radiative effect might contribute to the shock wave structure. Moreover, we showed that characteristic length of collisional relaxation processes is over  $\sim$  mm and also that they can be observed experimentally. We showed that the shock structure with relaxation region can be investigated in

the critical parameter region using our device because the accessible shock is much stronger than that from conventional methods and generated shock wave is steady and planar.

In chapter 3, we numerically calculated the physical parameters: ion and electron temperature distributions, and ion population distribution, in the relaxation region behind the jump front of strong shock wave, under steady and planar condition. We proposed comparative study between the calculation and the experiment using two fitting parameter: initial electron temperature and radiative flux to estimate the structure of the strong shock waves with relaxation layer. The calculation results indicated that the structure of ionization relaxation layer strongly depends on the two fitting parameters, electron temperature at the shock front and radiative flux in the shock region. We showed that comparisons between the calculation and our experiment are expected to allow us to estimate ionization evolution, precursor region, and radiative transfer effect on the structure of strong shock wave.

In chapter 4, we showed electron temperature measurements in the electro-magnetically driven strong shock waves by line pair method. The experiment showed anomalous results that electron temperature is almost constant over a long spatial scale along the shocked layer. The situation can not be explained by a conventional physical image that electrons get energy by electron-ion collisions in the shocked region.

In chapter 5, we discussed factors to keep electron temperature on the unexpectedly long scale. It was shown that the observed emission lines were from shock heated region and that the measurement results for electron temperature were not disturbed by the discharge plasma. We estimated that the cross section of atom-atom collisional ionization is  $\geq 10^{16}$  cm<sup>2</sup> from the initial rise of spectrum profile Xe II, and indicated that the atom-atom collision plays significant roles for the formation of the shock jump layer. Since the region behind shock front is considered to be ionized plasma by atom-atom collision, initial ionization problem, which means that poor “priming” electrons cause no ion-electron relaxation, is insignificant in this condition. We showed that radiative effect is important for the shock structure. The radiative cooling restricts the rise of electron temperature by ion-electron relaxation and delays the ionization relaxation. This behavior can correspond to the experimental results.

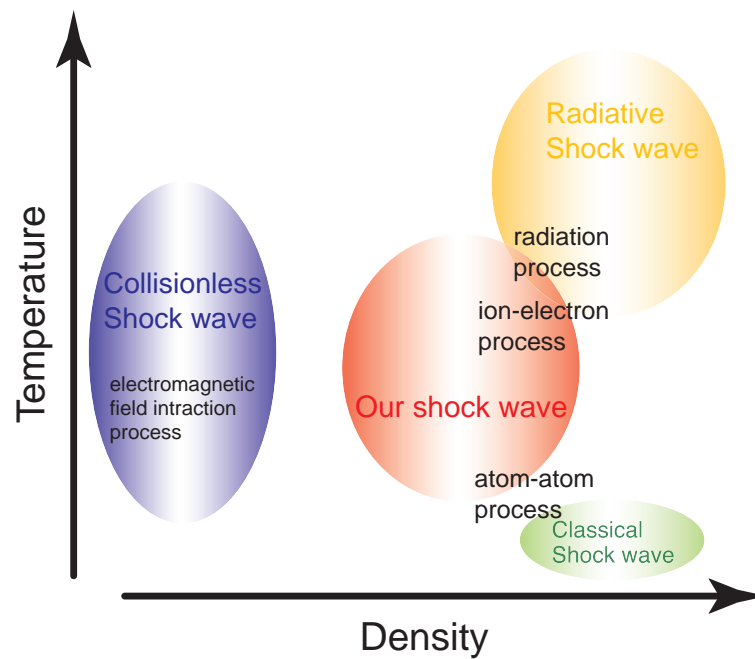


Figure 6.1: Various shock waves and their dominant dissipative processes

Finally, a relation between our experiment and radiative SNRs was discussed. Our electro-magnetically driven shock waves with radiative cooling is considered to be an useful test bed for scaling of laboratory experiments to radiative SNRs.

In summary, the structure of the strong shock wave using a compact pulse power device with a tapered electrodes and a guiding tube was discussed in this thesis. The electro-magnetic method enables us to make a well-defined condition: steady and planer, by which we can measure the shock velocity and electron temperature profile. The experimental results were compared to the calculations, which indicate that a dissipative process that is induced by atom-atom collisional ionization, is significant for the formation and the radiative process play a significant role for the structure of the electro-magnetically driven strong shock wave. The shock waves with radiative cooling may provide a key material for further discussion of scaling to radiative SNRs.

Fig. 6.1 shows the correlation between the kinds of shock wave and the dominant dissipative processes in a temperature and density plane. The shock waves in the universe are extending over an extremely wide range of parameter region. Our

shock wave device discussed in this thesis has a specific characteristics: strong shock formation in low density. In the parameter region, the interplay of various dissipative processes: atom-atom collision process, ion-electron process, radiation process, establishes the structure of the shock wave. Whereas the physics of the collisional shock wave is significant for SNRs dynamics as shown in Sec. 1.1, the collisionless shock wave in extremely low density is considered to play an important role for shock acceleration of high energy particles [99]. The dominant dissipative process of the collisionless shock is considered to be electromagnetic field interaction. As just described in this thesis, dominant dissipative processes are vastly shifting depending on the physical parameters. We can extend the parameter region of electro-magnetically driven plasma, by scaling the specification of pulse power device.

Finally, if we carefully generate a well-defined phenomenon in an interested physical parameter, the structure of the focused phenomenon can be estimated. Although phenomena in the universe, including the Big Bang, are intrinsically non-linear, non-equilibrium state and are relaxing to equilibrium with extremely long time scale, this approach is expected to have potential to estimate them. That may reproduce a part of our universe in a laboratory and could give an important insight for the beginning of the universe and naturally the origin of ourselves.

# Appendix A

## Rogowski Coil and Calibration

As shown in Sec.2.4.1, we selected an external integration type Rogowski coil as the current probe in this experiment. Here we explain the designed Rogowski coil and its calibration procedure. The Rogowski Coil shown in Fig. A.1 consists of a helical wire coil with the lead from one end returning through the center of the coil to the other end, thus both terminals are at the same end of the coil.

The whole assembly is then wrapped around the straight conductor whose current is to be measured. Since the voltage that is induced in the coil is proportional to the rate of change of current in the straight conductor, the output of the Rogowski coil is connected to an electrical integrator circuit to provide an output signal that is proportional to current.

The circuit equation in Fig. A.2 is expressed as the following,

$$N \frac{d\phi}{dt} = L \frac{di}{dt} + (r + R)i + \frac{1}{C} \int_0^t i dt, \quad (\text{A.1})$$

where  $N$  is roll number turn/m,  $\phi$  is magnetic flux,  $L$  and  $r$  are self inductance and resistance,  $C$  and  $R$  are external capacitance and resistance. Since low frequency is considered,

$$\frac{1}{RC} \ll \omega \ll \frac{R}{L}. \quad (\text{A.2})$$

When the condition,  $r \ll R$  is assumed, Eq.(A.1) can be reduced to the following

$$N \frac{d\phi}{dt} \approx Ri. \quad (\text{A.3})$$

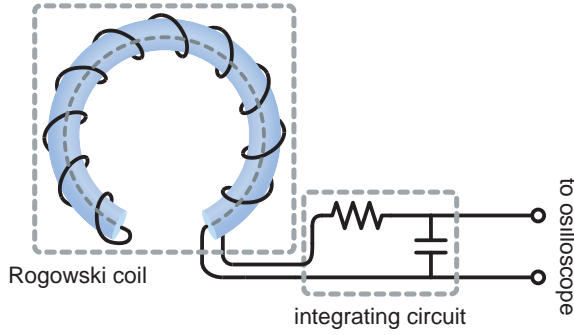


Figure A.1: A sketch of Rogowski Coil

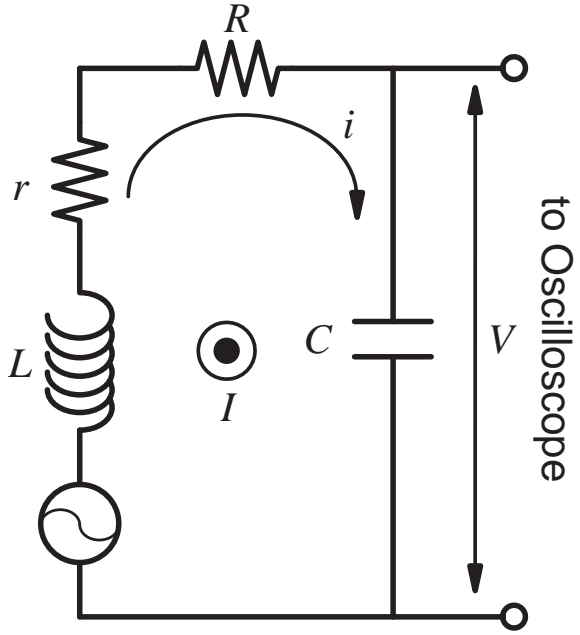


Figure A.2: Equivalent circuit of Rogowski coil

The equation of the change of the magnetic flux is

$$\frac{d\phi}{dt} = \frac{d(BS)}{dt} = \frac{d}{dt} \left( \mu_0 \frac{I}{2\pi r_1} S \right) = \mu_0 \frac{r_2^2}{2r_1} \frac{dI}{dt}, \quad (\text{A.4})$$

where  $r_1$  is the toroidal radius,  $r_2$  is the poloidal radius of Rogowski Coil, and  $S$  is the cross section of the coil.

When Eq.(A.3) is substituted, Eq.(A.4) is

$$\mu_0 \frac{Nr_2^2}{2r_1} \frac{dI}{dt} \approx Ri. \quad (\text{A.5})$$

Time integration of Eq.(A.5) is

$$\mu_0 \frac{Nr_2^2}{2r_1} \int_0^t \frac{dI}{dt} dt \approx R \int_0^t i dt. \quad (\text{A.6})$$

Since the measured voltage  $V$  is  $V = \frac{1}{C} \int_0^t i dt$ , the discharge current  $I$  is estimated by

$$I \approx \frac{2r_1 RC}{\mu_0 Nr_2^2} V = \alpha V. \quad (\text{A.7})$$

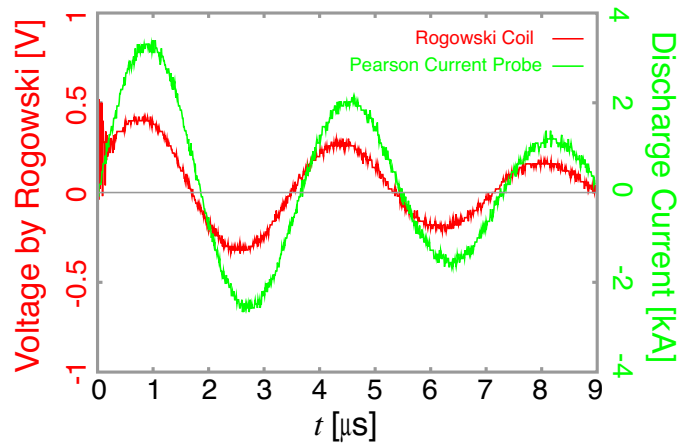


Figure A.3: Discharge current for calibration

Here, to measure the coefficient  $\alpha$ , calibration experiment is performed using a current probe [PEARSON ELECTRONICS, Inc., 110A] for calibration.

The waveforms of discharge current for the calibration experiment are shown in Fig. A.3. When the fitting by the least squares method gives  $\alpha \sim 7300$  A/V. We used this coefficient for the evaluation of discharge current.

# Appendix B

## Sweep and Delay Time of Streak Unit

We have to identify the sweep and delay time [100] of streak unit to synchronize the shock wave as referred in Sec. 4.3. Then, a calibration test was performed using a LED. Before that, we need to know the runtime measurement of LED for this setup. Then, the setup for runtime of LED is shown in Fig. B.1. The runtime of LED was obtained from the received signal timing of the photodiode and the output signal timing of the LED, and this time was  $\sim 510$  ns.

Next, the setup for the calibration of the streak unit is shown in Fig. B.2. The single shot trigger drove the delay pulse generator [Stanford Research System, Inc., DG 535] and the delay pulse generator controlled the streak unit and the function generator [Tektronix, Inc., AFG 3022] connected with LED.

The timing chart of the calibration test is shown in Fig. B.3. In Fig. B.3, the blue arrows are known and the orange ones are unknown time duration. From LED signal timing and the received streak image, the streak sweep time and the delay time for streak mode were characterized.

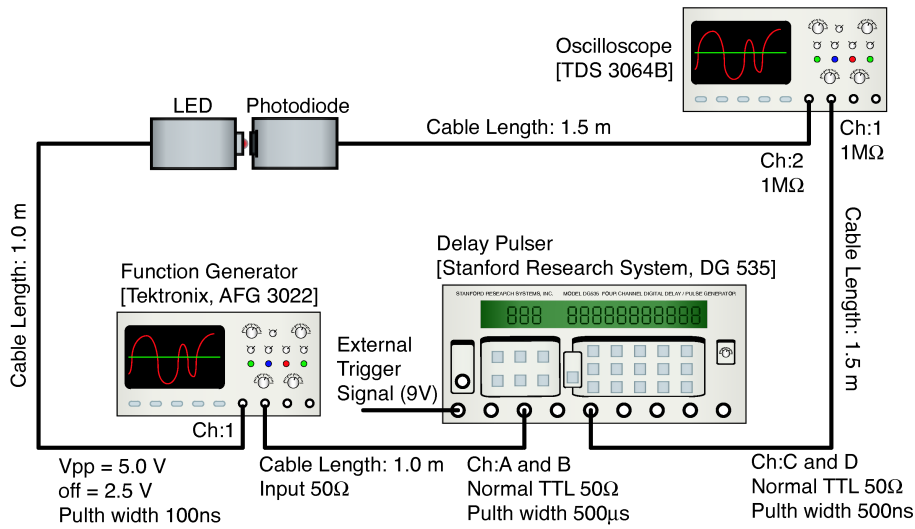


Figure B.1: Setup for runtime measurement of LED

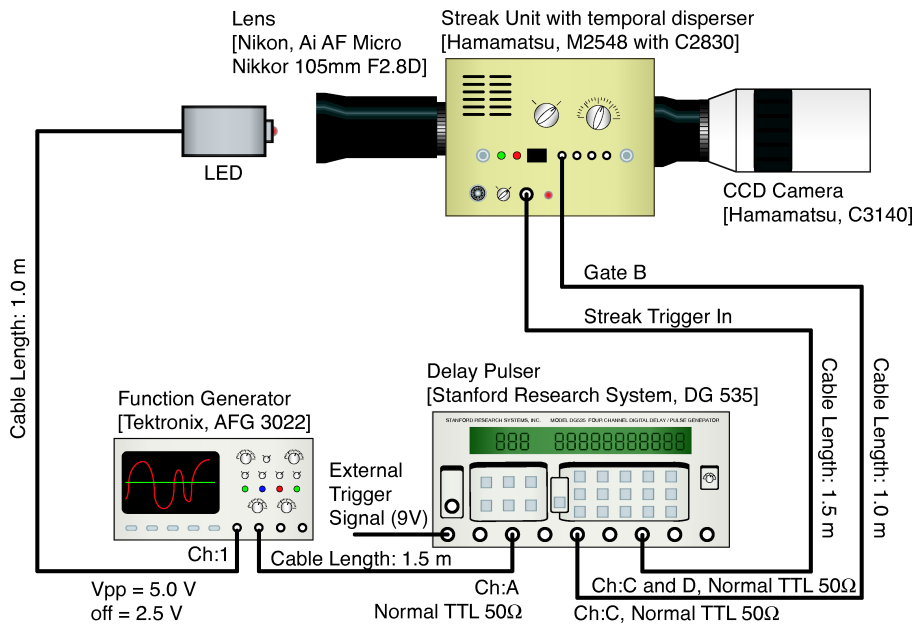


Figure B.2: Setup for calibrating of streak unit

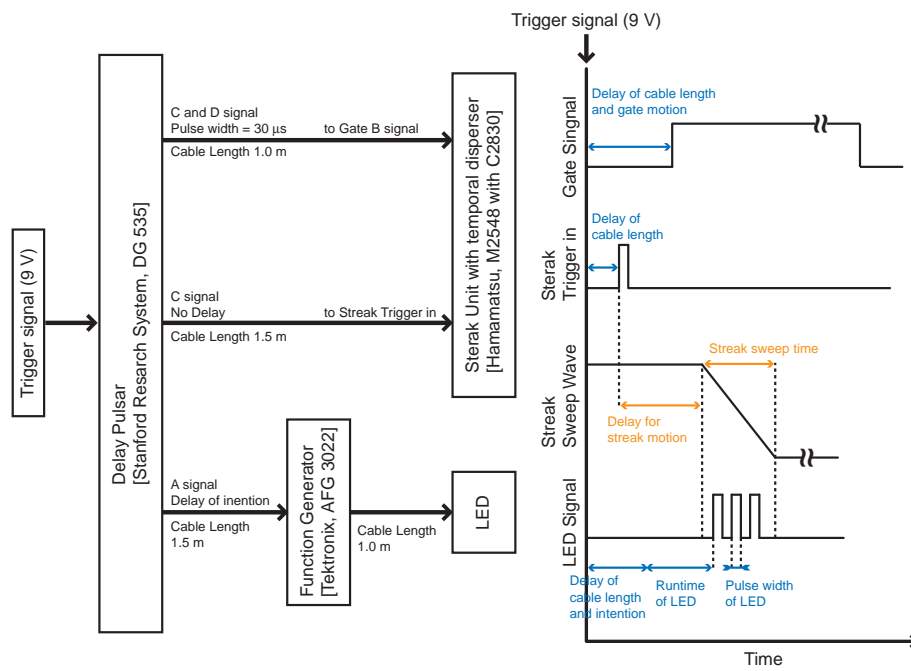


Figure B.3: Timing chart for the calibration

# Appendix C

## Xe II Atomic Data

22 Available Xe II atomic data are shown in Table C.1 [98]. In the table, the first column provides the wavelength in units of nm, the second means radiative decay rate in units of 1/s, the third stands for energy level, the fourth represents configurations, and the final provides degeneracy of a state.

Table C.1: Xe II atomic data

Wavelength nm	$A_r(j \rightarrow i)$ 1/s	$E_i - E_j$ eV	Configurations	$g_i - g_j$
433.052	$1.4 \times 10^8$	14.0737 - 16.9359	$5p^4(^3P_2)6p-5p^4(^3P_2)6d$	6 - 8
441.484	$1.0 \times 10^8$	13.5840 - 16.3916	$5p^4(^1D_2)6s - 5p^4(^1D_2)6p$	6 - 6
460.303	$8.2 \times 10^7$	11.7864 - 14.4792	$5p^4(^3P_2)6s - 5p^4(^3P_2)6p$	4 - 4
484.433	$1.1 \times 10^8$	11.5390 - 14.0976	$5p^4(^3P_2)6s - 5p^4(^3P_2)6p$	6 - 8
487.650	$6.3 \times 10^7$	13.5840 - 16.1258	$5p^4(^1D_2)6s - 5p^4(^1D_2)6p$	6 - 8
526.044	$2.2 \times 10^7$	12.9253 - 15.2816	$5p^4(^3P_1)5d - 5p^4(^3P_1)6p$	2 - 4
526.195	$8.5 \times 10^7$	14.0008 - 16.3564	$5p^4(^1D_2)6s - 5p^4(^1D_2)6p$	4 - 4
529.222	$8.9 \times 10^7$	11.5390 - 13.8811	$5p^4(^3P_2)6s - 5p^4(^3P_2)6p$	6 - 6
537.239	$7.1 \times 10^7$	11.7864 - 14.0936	$5p^4(^3P_2)6s - 5p^4(^3P_2)6p$	4 - 2
541.915	$6.2 \times 10^7$	11.7864 - 14.0737	$5p^4(^3P_2)6s - 5p^4(^3P_2)6p$	4 - 6
543.896	$7.4 \times 10^7$	12.7454 - 15.0243	$5p^4(^3P_1)6s - 5p^4(^3P_1)6p$	4 - 2

Wavelength nm	$A_r(j \rightarrow i)$ 1/s	$E_i - E_j$ eV	Configurations	$g_i - g_j$
547.261	$9.9 \times 10^6$	11.8327 - 14.0976	$5p^4(^3P_2)5d - 5p^4(^3P_2)6p$	8 - 8
553.107	$8.8 \times 10^6$	11.8327 - 14.0737	$5p^4(^3P_2)5d - 5p^4(^3P_2)6p$	8 - 6
571.961	$6.1 \times 10^6$	11.9066 - 14.0737	$5p^4(^3P_2)5d - 5p^4(^3P_2)6p$	4 - 6
597.646	$2.8 \times 10^7$	11.7864 - 13.8604	$5p^4(^3P_2)6s - 5p^4(^3P_2)6p$	4 - 4
603.620	$7.5 \times 10^6$	11.8276 - 13.8811	$5p^4(^3P_2)5d - 5p^4(^3P_2)6p$	6 - 6
605.115	$1.7 \times 10^7$	11.8327 - 13.8811	$5p^4(^3P_2)5d - 5p^4(^3P_2)6p$	8 - 6
609.759	$2.6 \times 10^7$	11.8276 - 13.8604	$5p^4(^3P_2)5d - 5p^4(^3P_2)6p$	6 - 4
627.082	$1.8 \times 10^7$	14.0008 - 15.9774	$5p^4(^1D_2)6s - 5p^4(^1D_2)6p$	4 - 6
627.754	$3.6 \times 10^6$	11.9066 - 13.8811	$5p^4(^3P_2)5d - 5p^4(^3P_2)6p$	4 - 6
680.574	$6.1 \times 10^6$	13.4427 - 15.2640	$5p^4(^3P_1)5d - 5p^4(^3P_1)6p$	8 - 6
699.088	$2.7 \times 10^7$	12.3246 - 14.0976	$5p^4(^3P_2)5d - 5p^4(^3P_2)6p$	10 - 8

# Bibliography

- [1] E. Hubble, "*A Relation between Distance and Radial Velocity among Extra-Galactic Nebulae*", The Proceedings of the National Academy of Sciences of the United States of America, **15**, 168 (1929).
- [2] G.Lemaître, "*The Expanding Universe*", Monthly Notices of the Royal Astronomical Society, **91**, 490 (1931).
- [3] E. Kolb, T. Michael, "*The Early Universe*" (Addison-Wesley, New York, 1988).
- [4] J. A. Peacock, "*Cosmological Physics*" (Cambridge University Press, Cambridge, 1999).
- [5] Plasma Science Comm Committee on High Energy Density Plasma Physics, "*Frontiers in High Energy Density Physics: The X-Games of Contemporary Science*" (National Academies Press, Washington, D. C., 2003).
- [6] B. A. Remington, R. P. Drake, D. D. Ryutov, "*Experimental astrophysics with high power lasers and Z pinches*", Review of Modern Physics, **78**, 755 (2006).
- [7] D. Ryutov, R. P. Drake, J. Kane, E. Liang, B. A. Remington, W. M. Wood-Vasey, "*Similarity Criteria for The Laboratory Simulation of Supernova Hydrodynamics*", The Astrophysical Journal, **518**, 821 (1999).
- [8] D. Ryutov, B. A. Remington, H. F. Robey, R. P. Drake, "*Magnetohydrodynamic scaling: From astrophysics to the laboratory*", Physics of Plasmas, **8**, 1804 (2001).

- 
- [9] H. W. Liepmann, A. Roshko, "*Elements of Gasdynamics*" (Dover Publications, Inc., New York, 2001).
- [10] Y. B. Zel'dovich, Y. P. Raizer, "*Physics of Shock Waves and High-Temperature Hydrodynamic Phenomena*" (Academic Press, New York, 1967).
- [11] C. Kittel, "*Thermal Physics*" (John Wiley and Sons, New York, 1969).
- [12] L. Woltjer, "*Supernova Remnants*", Annual Review of Astronomy and Astrophysics, **10**, 129 (1972).
- [13] M. Kawasaki, "*X-Rays Study of Ionization States in Supernova Remnants*", Ph.D. thesis, University of Tokyo (2003).  
[http://www.astro.isas.jaxa.jp/asca/bibliography/phd\\_thesis.html](http://www.astro.isas.jaxa.jp/asca/bibliography/phd_thesis.html).
- [14] R. P. Drake, "*High-Energy-Density Physics*" (Springer, New York, 2006).
- [15] R. A. Chevalier, "*The Radio and X-ray Emission from Type II Supernovae*", The Astrophysical Journal, **259**, 302 (1982).
- [16] C. Fransson, "*Comptonization and UV Emission Lines from Type II Supernovae*", Astronomy and Astrophysics, **133**, 264 (1984).
- [17] J. M. Blondin, B. A. Fryxell, A. Königl, "*The Structure and Evolution of Radiatively Cooling Jets*", The Astrophysical Journal, **360**, 370 (1990).
- [18] R. A. Chevalier, C. Fransson, "*Emission from Circumstellar Interaction in Normal Type II Supernovae*", The Astrophysical Journal, **420**, 268 (1994).
- [19] R. A. Chevalier, "*Type II Supernovae SN 1987A and SN 1993J*", Science, **276**, 1374 (1997).
- [20] F. H. Shu, F. C. Adams, S. Lizano, "*Star Formation in Molecular Clouds: Observation and Theory*", Annual Review of Astronomy and Astrophysics, **25**, 23 (1987).

- [21] M. Kawasaki, M. Ozaki, F. Nagase, H. Inoue, R. Peter, "*Ionization States and Plasma Structures of Mixed - Morphology Supernova Remnants Observed with ASCA*", The Astrophysical Journal, **631**, 935 (2005).
- [22] D. Mihalas, B. W. Mihalas, "*Foundations of Radiation Hydrodynamics*" (Oxford University Press, New York, 1984).
- [23] S. Bouquet, R. Teyssier, and J. P. Chieze, "*Analytical Study and Structure of a Stationary Radiative Shock*," The Astrophysical Journal Supplement Series, **127**, 245 (2000).
- [24] R. P. Drake, "*Theory of Radiative Shocks in Optically Thick Media*", Physics of Plasmas, **14**, 043301 (2007).
- [25] A. C. Kolb, "*Production of High-Energy Plasmas by Magnetically Driven Shock Waves*", Physical Review Letters, **107**, 345 (1957).
- [26] A. C. Kolb, "*Propagation of Strong Shock Waves in Pulsed Longitudinal Magnetic Fields*", Physical Review Letters, **107**, 1197 (1957).
- [27] A. B. Reighard, R. P. Drake, "*The Formation of a Cooling in a Partially Optically Thick Shock*", Astrophysics Space Sciences, **307**, 121 (2007).
- [28] A. B. Reighard, R. P. Drake, J. E. Mucino, J. P. Knauer, M. Busquet, "*Planar Radiative Shock Experiments and Their Comparison to Simulations*", Physics of Plasmas, **14**, 056504 (2007).
- [29] A. B. Reighard, R. P. Drake, K. K. Dannenberg, D. J. Kremer, M. Grosskopf, E. C. Harding, D. R. Leibbrandt, "*Observation of Collapsing Radiative Shocks in Laboratory Experiments*", Physics of Plasmas, **13**, 082901 (2006).
- [30] M. Koenig, T. Vinci, A. Benuzzi-Mounaix, N. Ozaki, A. Ravasio, M. Rabec le Glohaec, L. Boireau, C. Michaut, S. Bouquet, S. Atzeni, A. Schiavi, O. Peyrusse, D. Batani, "*Radiative Shocks: An Opportunity to Study Laboratory Astrophysics*", Physics of Plasmas, **13**, 056504 (2006).

- [31] T. Vinci, M. Koenig, A. Benuzzi-Mounaix, C. Michaut, L. Boireau, S. Leygnac, S. Bouquet, O. Peyrusse, D. Batani, "*Temperature and Electron Density Measurements on Laser Driven Radiative shocks*", *Physics of Plasmas*, **13**, 010702 (2006).
- [32] S. Leygnac, L. Boireau, C. Michaut, T. Lanz, C. Stehle, C. Clique, S. Bouquet, "*Modeling Multidimensional Effects in the Propagation of Radiative Shocks*", *Physics of Plasmas*, **13**, 113301 (2006).
- [33] S. Bouquet, C. Stehle, M. Koenig, J. P. Chieze, A. Benuzzi-Mounaix, D. Batani, S. Leygnac, X. Fleury, H. Merdji, C. Michaut, F. Thais, N. Grandjouan, T. Hall, E. Henry, V. Malka, J. P. J. Lafon, "*Observation of Laser Driven Supercritical Radiative Shock Precursors*", *Physical Review Letters*, **92**, 225001 (2004).
- [34] J. M. Laming, "*Relationship Between Oscillatory Thermal Instability and Dynamical Thin-shell Overstability of Radiative Shocks*", *Physical Review E*, **70**, 057402 (2004).
- [35] X. Fleury, S. Bouquet, C. Stehle, M. Koenig, D. Batani, A. Benuzzi-Mounaix, J. P. Chieze, N. Grandjouan, J. Grenier, T. Hall, E. Henry, J. P. Lafon, S. Leygnac, V. Malka, B. Marchet, H. Merdji, C. Michaut, F. Thais, "*A Laser Experiment for Studying Radiative Shocks in Astrophysics*", *Laser and Particle Beams*, **20**, 263 (2002).
- [36] K. Shigemori, T. Ditmire, B. A. Remington, V. Yanovsky, D. Ryutov, K. G. Estabrook, M. J. Edwards, A. J. MacKinnon, A. M. Rubenchik, K. A. Keilty, E. Liang, "*Developing a Radiative Shock Experiment Relevant to Astrophysics*", *The Astrophysical Journal Letters*, **533**, 159 (2000).
- [37] L. I. Sedov, "*Mechanics of Continuous Media*" (World Scientific, Singapore, 1997).
- [38] J. Kane, D. Arnett, B. A. Remington, S. G. Glendinning, J. Castor, R. Wallace, A. Rubenchik, B. A. Fryxell, "*Supernova-relevant Hydrodynamic Instability Ex-*

- periments on the Nova Laser*", The Astrophysical Journal Letters, **478**, L75 (1997).
- [39] W. Hillebrandt, P. Höeflich, J. W. Truran, A. Weiss, "*Explosion of a blue supergiant: a model for supernova SN1987A*", Nature, **327**, 597 (1987).
- [40] T. Shigeyama, K. Nomoto, M. Hashimoto, "*Hydrodynamical models and the light curve of Supernova 1987A in the Large Magellanic Cloud*", Astronomy and Astrophysics, **196**, 141 (1988).
- [41] S. E. Woosley, P. A. Pinto, L. Ensmann, "*Supernova 1987A: Six Weeks Later*", The Astrophysical Journal, **324**, 466 (1988).
- [42] W. D. Arnett, J. N. Bahcall, R. P. Kirshner, S. E. Woosley, "*Supernova 1987A*", Annual Review of Astronomy and Astrophysics, **27**, 629 (1989).
- [43] E. Muller, W. Hillebrandt, M. Orio, P. Höflich, R. Mönchmeyer, B. A. Fryxell, "*Mixing and Fragmentation in Supernova Envelopes*", Astronomy and Astrophysics, **220**, 167 (1989).
- [44] T. Suzuki, T. Shigeyama, K. Nomoto, "*X-Ray Emission from the Collision of the Ejecta with the Ring Nebula around Supernova 1987A*", Astronomy and Astrophysics, **274**, 883 (1993).
- [45] K. J. Borkowski, J. M. Blondin, R. McCray, "*X-Rays from the Impact of SN 1987A with Its Circumstellar Ring*", The Astrophysical Journal, **477**, 281 (1997).
- [46] L. D. Landau, E. M. Lifshitz, "*Fluid Mechanics*" (Buterworth-Heinemann, Oxford, 1997).
- [47] F. F. Chen, "*Introduction to Plasma Physics and Controlled Fusion*" (Plenum Press, New York, 1984).
- [48] L. Spitzer, "*The Physics of Fully Ionized Gases*" (Interscience Publishers, New York, 1962).

- [49] T. J. M. Boyd, J. J. Sanderson, "*The Physics of Plasmas*" (Cambridge University Press, Cambridge, 2003).
- [50] D. H. McNeill, "*Electron Heating in Collisional Shocks*", *The Physics of Fluids*, **18**, 44 (1974).
- [51] R. E. Marshak, "*Effect of Radiation on Shock Wave Behavior*", *The Physics of Fluids*, **1**, 24 (1958).
- [52] R. S. Sutherland, M. A. Dopita, "*Cooling Functions for Low-Density Astrophysical Plasmas*", *The Astrophysical Journal Supplement Series*, **88**, 253 (1993).
- [53] H. W. Drawin, "*Influence of Atom-Atom Collisions on the Collisional-Radiative Ionization and Recombination Coefficients of Hydrogen Plasmas*", *Zeitschrift für Physik*, **225**, 483 (1969).
- [54] H. H. Fleischmann, R. C. Dehmelt, "*On Drawin's Formula for Ionization in Atom-Atom Collisions*", *Zeitschrift für Physik*, **252**, 435 (1972).
- [55] R. C. Amme, P. O. Haugsjaa, "*Ionization in Low-Energy Atomic Collisions of Neon with Neon and Krypton with Krypton*", *Physical Review*, **177**, 230 (1969).
- [56] W. M. Kornegay, H. S. Johnston, "*Kinetics of Thermal Ionization. II. Xenon and Krypton*", *The Journal of Chemical Physics*, **38**, 214 (2242).
- [57] K. E. Harwell, R. G. Jahn, "*Initial Ionization Rates in Shock-Heated Argon, Krypton, and Xenon*", *The Physics of Fluids*, **7**, 214 (1964).
- [58] E. J. Morgan, R. D. Morrison, "*Ionization Rates behind Shock Waves in Argon*", *The Physics of Fluids*, **8**, 1608 (1965).
- [59] A. J. Kelly, "*Atom-Atom Ionization Cross Sections of the Noble Gases-Argon, Krypton, and Xenon*", *The Journal of Chemical Physics*, **45**, 1723 (1966).
- [60] J. A. Smith, "*Experimentally Determined Structure of the Shock Reflection Process in Ionizing Xenon*", *The Physics of Fluids*, **11**, 2150 (1968).

- 
- [61] M. Merilo, E. J. Morgan, "*Total Ionization Times in Shock-Heated Noble Gases*", The Journal of Chemical Physics, **52**, 2192 (1970).
- [62] Y. Enomoto, M. Kawamura, "*Ionization Relaxation of Shock-Heated Xenon under the Influence of Wall Boundary Layer*", Journal of the Physical Society of Japan, **45**, 1723 (1966).
- [63] M. A. Liberman, J. S. De Groot, A. Toor, R. B. Spielman, "*Physics of High-Density Z-Pinch Plasmas*", (Springer - Verlag, New York, 1999).
- [64] M. J. Bernstein, F. Hai, "*Neutron Production in a Plasma Focus Discharge with and without Axial Magnetic Field*", The Physics of Fluids, **14**, 1010 (1970).
- [65] R. Lebert, W. Neff, R. Holz, F. Richter, "*Plasma Focus as Intense Light Source for Soft X-ray Microscopy*", AIP Conference Proceedings, **195**, 507 (1989).
- [66] R. M. Patrick, "*High-Speed Shock Waves in a Magnetic Annular Shock Tube*", The Physics of Fluids, **2**, 589 (1959).
- [67] R. M. Patrick, "*Production of High-velocity Shocks*", Journal of Applied Physics, **29**, 30 (1958).
- [68] Yu. P. Raizer, "*Gas Discharge Physics*", (Springer - Verlag, New York, 1997).
- [69] Yu. D. Korolev, G. A. Mesyats, "*Physics of Pulsed Breakdown in Gases*", (URO-PRESS, Yekaterinburg, 1998).
- [70] K. Kondo, M. Nakajima, T. Kawamura, K. Horioka, "*Compact Pulse Power Device for Generation of One-dimensional Strong Shock Waves*", Review of Scientific Instruments, **77**, 036104 (2006).
- [71] K. Kondo, M. Nakajima, T. Kawamura, K. Horioka, "*Electromagnetically Driven Radiative Shocks and Their Measurements*", Journal de Physique IV, **133**, 1051 (2006).
- [72] D. Salzmann, "*Atomic Physics in Hot Plasmas*", (Oxford University Press, New York, 1998).

- [73] R. W. P. McWhirter, "*Plasma Diagnostic Techniques*", (Academic Press, New York, 1965).
- [74] M. J. Seaton, "*Atomic and Molecular Processes*", (Academic Press, New York, 1962).
- [75] W. Lotz, "*Electron-Impact Ionization Cross-sections and Ionization Rate Coefficients for Atoms and Ions from Hydrogen to Calcium*", *Zeitschrift für Physik*, **216**, 241 (1968).
- [76] R. K. Landshoff, J. D. Perez, "*Determination of Plasma Parameters of Laser-produced Aluminium Plasma from X-ray Line Radiation*", *Physical Review A*, **13**, 1619 (1976).
- [77] D. Salzmann, A. Krumbein, "*Calculation of X-ray Production Rate and Ionization-state Density in Hot Aluminum Plasma*", *Journal of Applied Physics*, **49**, 3229 (1978).
- [78] T. Kawamura, Ph.D. thesis, Osaka University (1999), (*Japanese*).
- [79] M. Seaton, "*Radiative Recombination of Hydrogenic Ions*", *Monthly Notices of the Royal Astronomical Society*, **119**, 81 (1959).
- [80] M. Abramowitz, I. A. Stegun, "*Handbook of Mathematical Functions*", (Dover Publications, Inc., New York, 1972).
- [81] D. H. Menzel, C. L. Pekeris, "*Absorption Coefficients and Hydrogen Line Intensities*", *Monthly Notices of the Royal Astronomical Society*, **96**, 77 (1935).
- [82] J. Cooper, "*Plasma Spectroscopy*", *Reports on Progress in Physics*, **29**, 35 (1966).
- [83] R. Mewe, "*Interpolation Formulae for the Electron Impact Excitation of Ions in the H-, He-, Li-, and Ne- Sequences*", *Astronomy and Astrophysics*, **20**, 215 (1972).

- 
- [84] T. Fujimoto, "*Plasma Spectroscopy*" (Oxford University Press, New York, 2004).
- [85] R. A. Golobic, R. M. Nerem, Phys. Fluids, "*Structure of Strong Shock Waves in Xenon. I: Electron temperature measurements*", Physics of Fluids, **16**, 1622 (1973).
- [86] W. H. Foley, J. B. Barder, and R. M. Nerem, "*Structure of Strong Shock Waves in Xenon. II: Further Experiments and Theoretical Interpretation*", The Physics of Fluids, **16**, 1630 (1973).
- [87] H. Brysk, P. M. Campbell, P. Hammerling, "*Thermal Conduction in Laser Fusion*", Plasma Physics, **17** 473 (1975).
- [88] K. Kondo, M. Nakajima, T. Kawamura, K. Horioka, "*Relaxation Layer in Electro-magnetically Driven Strong Shocks*", Journal of Physics: Conference Series, **112** 042028 (2008).
- [89] E. B. Saloman, "*Energy Levels and Observed Spectral Lines of Xenon, Xe I through Xe LIV*", Journal of Physical and Chemical Reference Data, **33** 765 (2004).
- [90] T. M. E. Sherbini, "*Transition Probabilities and Radiative Lifetimes for Singly Ionized Xenon*", Journal of Physics B: Atomic, Molecular and Optical Physics, **9** 1665 (1976).
- [91] L. Allen, D. G. C. Jones, D. G. Schofield, "*Radiative Lifetimes and Collisional Cross Sections for Xe I and II*", Journal of The Optical Society of America, **59** 842 (1969).
- [92] J. E. Hansen, W. Persson, "*The Influence of Relativistic Effects on the Lifetime of the  $5s5p^6\ ^2S_{1/2}$  State of Xe II*", Journal of Physics B: Atomic, Molecular and Optical Physics, **12** L331 (1979).

- [93] H. O. Di Rocco, D. I. Iriarte, J. A. Pomarico, "Lifetimes and Transition Probabilities of Xe II: Experimental Measurements and Theoretical Calculations", The European Physical Journal D, **10** 19 (2000).
- [94] K. E. Donnelly, P. J. Kindlmann, W. R. Bennett, Jr., "Radiative-lifetime Measurements of Levels in the  $5p^4 6p$  Configuration of Singly Ionized Xenon", Journal of The Optical Society of America, **63** 1438 (1973).
- [95] J. E. Hansen, W. Persson, "Revised Analysis of Singly Ionized Xenon, Xe II", Physica Scripta, **36** 602 (1987).
- [96] S. Zielińska, Ł. Bratasz, K. Dzierżega, "Absolute Transition Rates for Transitions from  $5p^4(^3P)6p^4P_{5/2}^o, ^4P_{3/2}^o, ^4D_{7/2}^o$  and  $^2D_{5/2}^o$  Levels of Xe II", Physica Scripta, **66** 454 (2002).
- [97] H. R. Griem, "Plasma Spectroscopy" (McGraw Hill Book, New York, 1964).
- [98] National Institute of Standards and Technology: Atomic Spectra Database, <http://physics.nist.gov/PhysRefData/ASD/index.html>
- [99] F. C. Jones, D. C. Ellison, "The Plasma Physics of Shock Acceleration", Space Science Reviews, **58** 259 (1991).
- [100] Hamamatsu Photonics M2548 Instruction Manual, (*Japanese*).